UNIVERSITY OF CALIFORNIASAN DIEGO

Ultrafast magnetization dynamics in quantum materials

A dissertation submitted in partial satisfaction of the
requirements for the degree
Doctor of Philosophy

in

Physics

by

Peter Kyu Min Kim

Committee in charge:

Professor Richard D. Averitt, Chair
Professor Alex Frañó
Professor Eric Fullerton
Professor Tarun Grover
Professor Tenio Popmintchev

2024

The dissertation of Peter Kyu Min Kim is approved, and it is acceptable in quality and form for publication on microfilm and electronically.

University of California San Diego

2024

DEDICATION

To my family, my friends, and the rest of this crazy universe.

TABLE OF CONTENTS

LIST OF FIGURES

LIST OF TABLES

ACKNOWLEDGEMENTS

I would not be the scientist and person I am today without the countless interactions with those I've met during my time at UCSD. There are so many I'd like to thank for helping me throughout my PhD. Though incomplete, here is an attempt to thank those that made this dissertation possible:

Thank you, Rick, for being an incredible advisor. You created an environment where I could learn and thrive, and you have been nothing but supportive and insightful throughout all these years. I've learned so much physics, and perhaps more importantly, I've learned so much about being a scientist while working with you. I appreciate your dedication to the data, your skepticism and enthusiasm towards the ever-growing body of knowledge that is physics, and your patience as a mentor. You've left an indelible mark on my life and career, for which I am deeply grateful.

I also want to express my appreciation to everyone in the Averitt lab. When I first joined, I was welcomed by Peter, Dylan, Kevin, Gufeng, and Jacob. Though our time together was short, I gained a lot from each of you. I especially want to thank Peter and Dylan showing me the ropes of ultrafast when I first arrived. I'd also like to thank those I worked alongside: Max, Kelson, Mustafa, Varun, Yuan, Ian, Ananya, Nat, Junxiao, and the many others who have come through our lab. The years of conversations and camaraderie helped me grow and get through the suffering that seems intrinsic to getting this degree. I am especially thankful for Max, with whom I've worked closely on nearly all of the projects I've been a part of here. I couldn't have asked for a better partner in crime, and I look forward to our futures.

To my collaborators: Hari, Vlad, and Venkat, thank you for the countless discussions and Zoom meetings as we analyzed and interpreted the data. It was a pleasure working with you all. I also appreciate Alejandro and Alex for our work on β-Li_2IrO_3. Thank you for the beautiful samples and your patience throughout the process.

To my friends Erik, Isabella, Ping, Ahmed, and Aidee: thank you for being my

family here in San Diego. Your friendship and support have meant the world to me.

Finally, thank you to my family. Mom and Dad, you worked so hard and sacrificed so much for me and Paul. You all taught me how to be curious, responsible, and to love science and math. Your love and support have been my foundation. I could not have done this without you all. Thank you.

Chapter 4, in part, is currently being prepared for submission for publication of the material. Kim, Peter K.; Ruiz, Alejandro; Kissin, Peter; Poore, Maxwell; Vranas, Mayia; Analytis, James; Frañó, Alex; and Averitt, Richard D. The dissertation author was the primary investigator and author of this material.

Chapter 5, in full, is a reprint of the material as it appears in Nature Communications. Kim, Peter K.; Padmanabhan, Hari; Poore, Maxwell; Koocher, Nathan Z.; Stoica, Vladimir A.; Puggioni Danilo; Wang, Huaiyu (Hugo); Shen, Xiaozhe; Reid, Alexander H.; Gu, Mingqiang; Wetherington, Maxwell; Lee, Seng Huat; Schaller, Richard D.; Mao, Zhiqiang; Lindenberg, Aaron M.; Wang, Xijie; Rondinelli, James M.; Averitt, Richard D.; and Gopalan, Venkatraman, Nature Communications, 2022. The dissertation author shared the role of the primary investigator and author of this paper with Hari Padmanabhan and Maxwell Poore.

VITA

2017	B.A. in Physics, Vassar College
2018-2024	Graduate Teaching Assistant, University of California San Diego
2024	Ph.D. in Physics, University of California San Diego

PUBLICATIONS

Peter K. Kim, Alejandro Ruiz, Peter Kissin, Maxwell Poore, Mayia Vranas, Ananya Rai, James Analytis, Alex Frañó, and Richard D. Averitt. *Quasiparticle dynamics and tracking magnetism in β-Li_2IrO_3*, (in preparation).

Hari Padmanabhan, Vladimir A. Stoica, **Peter K. Kim**, Maxwell Poore, Tiannan Yang, Xiaozhe Shen, Alexander H. Reid, Ming-Fu Lin, Suji Park, Jie Yang, Huaiyu Wang, Nathan Z. Koocher, Danilo Puggioni, Alexandru B. Georgescu, Lujin Min, Seng Huat Lee, Zhiqiang Mao, James M. Rondinelli, Aaron M. Lindenberg, Long-Qing Chen, Xijie Wang, Richard D. Averitt, John W. Freeland, Venkatraman Gopalan. *Large Exchange Coupling Between Localized Spins and Topological Bands in MnBi2Te4,* Advanced Materials **34**, 2202841 (2022).

Peter K. Kim, Hari Padmanabhan, Maxwell Poore, Nathan Z. Koocher, Vladimir A. Stoica, Danilo Puggioni, Xiaozhe Shen, Alexander H. Reid, Mingqiang Gu, Maxwell Wetherington, Seng Huat Lee, Richard D. Schaller, Zhiqiang Mao, Aaron M. Lindenberg, Xijie Wang, James M. Rondinelli, Richard D. Averitt, Venkatraman Gopalan. *Interlayer magnetophononic coupling in MnBi2Te4.* Nature Communications **13**, 1929 (2022)

Dylan Lovinger, Eli Zoghlin, Peter Kissin, Gihyeon Ahn, Kaveh Ahadi, **Peter Kim**, Maxwell Poore, Susanne Stemmer, Soonjae Moon, Stephen D. Wilson, and Richard D. Averitt. *Magneto-elastic coupling to coherent acoustic phonon modes in ferrimagnetic insulator $GdTiO_3$*, Physical Review B **102**, 085138 (2020).

Sylvie Rangan, **Peter Kim**, Charles Ruggieri, Stephen Whitelam, and Robert A. Bartynski. *Growth of a highly ordered inhomogeneous kinetically trapped molecular monolayer*, Physical Review B **100**, 245411 (2019).

ABSTRACT OF THE DISSERTATION

Ultrafast magnetization dynamics in quantum materials

by

Peter Kyu Min Kim
Doctor of Philosophy in Physics

University of California San Diego, 2024

Professor Richard D. Averitt, Chair

The diversity of phases and functional properties in quantum materials emerges from competing energy scales, strong couplings between internal degrees of freedom, geometric frustration, topology, and reduced dimensionality. The complexity of these materials consistently challenges our understanding of the underlying physics governing their properties. To this end, ultrafast experimental techniques are invaluable tools for disentangling these aspects by selectively driving degrees of freedom or excitations and observing the cascade of dynamics in the time domain. In this dissertation, we investigate the ultrafast dynamics in various quantum materials, focusing

on how the near-equilibrium responses correspond to their magnetic properties. We study β-Li_2IrO_3, a Mott insulator with strong spin-orbit coupling, and $MnBi_2Te_4$, a topological insulator with intrinsic antiferromagnetic ordering. In the former, we study how photoexcitation leads to the formation of quasiparticles whose dynamics are directly linked to equilibrium order parameters. We demonstrate how these dynamics evolve across the phase diagram and can be associated with short-ranged spin correlations above the conventional magnetic ordering temperatures. In the latter, we observe strong spin-phonon coupling likely originating from the modulation of the interlayer spin exchange due to lattice motion of the phonons. Our findings demonstrate that ultrafast techniques provide critical insights into the complex interplay of spin, charge, and lattice degrees of freedom, offering a deeper understanding of the fundamental properties and potential applications of quantum materials.

Chapter 1

Introduction

1.1 Historical Prelude

Historically, the understanding and utilization of the materials around us have quickly transformed the living conditions and world for humans over the last 10,000 years. From fire to tools to steam engines to computers, each innovation has irreversibly changed the structure of human civilization.

Alongside the advancements and technologies borne from the study of materials is a growing understanding of the fundamental nature of matter. For instance, through the study of thermodynamics and statistical mechanics, we gained insights into the concepts of work, temperature, pressure, and entropy, which paved the way for advancements in material synthesis (e.g. steel) and the development of technologies such as the steam engine. This progress continued into the realm of solid state physics, where we gained new insights into the collective behavior of many-body systems in solids, notably incorporating quantum mechanical effects. These breakthroughs ultimately led to the invention of the transistor and laid the foundation for modern computation.

This brings me to the modern study of condensed matter physics, a major goal

of which is to understand the collective behavior of many-body systems. This field has led to a deeper understanding collective states of matter vis-à-vis the Landau paradigm of phase transitions, and continues to expand as we develop our understanding of topological phases of matter. There have been notable milestones in this field, such as an understanding of (type I) superconductivity and the fractional quantum Hall effect. This has already had impacts beyond condensed matter physics, for example, laying the groundwork for understanding the Higgs mechanism in the Standard Model and the use of superconductors in technologies such as MagLev trains and magnetic resonance imaging (MRI). Though we are still in the midst of unraveling these ideas, it is clear that these ideas will have far reaching impacts.

One major avenue in the study of condensed matter physics is the study of emergent phenomena in strongly correlated systems. The notion of emergent phenomena are properties of a composite system where "the whole is greater than the sum of its parts", a quote often attributed to Aristotle. In other words, in a composite or multi-scale system, properties of the collective system arise that are distinct from the properties of the constituent parts. For example, snow flakes have new symmetries that are not apparent in the constituent water molecules that compose them. Strongly correlated systems are ones where the constituents of the system, such as the electrons and holes in solids, interact strongly. Of particular interest are systems that demonstrate emergent properties such as superconductivity and the fractionalized quantum Hall effect.

The question arises of how to discover, understand, and engineer these emergent properties and states of matter. There is a significant focus on electronic and magnetic properties in materials research and condensed matter physics. A reasonable approach to experimentally probing these properties is through the interactions of these materials with electromagnetic waves, or light.

There are many advantages of using light to probe materials. One aspect is the wide range of energies that are accessible to probe phenomena on an enormous

range of scales. We can generate light with energies ranging from radio frequencies ($\sim 1 \times 10^{-8}$ eV) to X-rays ($\sim 1 \times 10^{5}$ eV). This allows us to probe electronic and magnetic properties across a huge range of energy, which gives us insight into the fundamental excitations that often act as unique fingerprints to the underlying state of matter.

Moreover, we can utilize a wide range of techniques, For example, we can use spectroscopy, microscopy, and diffraction, each exploiting different properties of light that we can control and measure. Much of this diversity of applications is due to the long history of study which continues on to this day. In fact, the primary method for using light to measure material properties has only been possible approximately 30 years ago: sub-picosecond time-resolved spectroscopy.

Sub-picosecond time-resolved spectroscopy utilizes lasers that are able to generate pulses of light with temporal widths down to 10s of femtoseconds, high intensities, and wavelength control from the THz range to the soft X-ray range. This builds on the techniques mentioned above with the advantage of measuring time-resolved dynamics on the fastest time-scales governing the physics of materials.

This thesis focuses on the application of sub-picosecond time-resolved techniques to explore the fundamental understanding of novel phases of matter arising from strong interactions, magnetism, non-equilibrium drives, and topology.

1.2 Scope of thesis

Chapter 2 goes through the experimental techniques used throughout the rest of the thesis. Chapter 2.1 describes the pulsed laser source, the Nd:YAG laser. This is followed by a description of time-resolved experimental techniques used to probe the materials of interest in Chapter 2.2. In particular, I describe the pump-probe techniques of time-resolved reflectivity (Ch. 2.2.1) and time-resolved magneto-optical effects (Ch. 2.2.2). I describe the basic experimental setup used in the

experiments that follow as well as useful theoretical and practical background for understanding the measurements. Chapter **??** describes the cryostat and magnet used in the experiments that follow. Chapter **??** gives a theoretical background on nonlinear optics. Chapter 2.3 gives a theoretical background on optical parametric amplification which was used to generate various wavelengths in the optical and near-infrared regime for the experiments in the subsequent chapters. Chapter B describes the design and alignment of an optical parametric amplifier built in the Averitt lab.

Chapter 3 gives a theoretical background on the $j_{eff} = 1/2$ spin-orbit coupled Mott insulators and their relation to β-Li_2IrO_3, a proximate quantum spin liquid candidate.

Chapter 4 describes experimental work on β-Li_2IrO_3. Specifically, we use optical pump-probe spectroscopy to observe spin-exciton coupling, measure exciton-induced magnetic dynamics, and reveal signatures magnetic correlations above the magnetically ordered phases.

Chapter 5 covers work on $MnBi_2Te_4$. We show empirical evidence of interlayer spin-phonon coupling and provide a theoretical model of the spin-phonon coupling via a phonon-induced modulation of the interlayer exchange coupling.

Chapter 2

Experimental techniques

This chapter reviews the experimental techniques used in the projects described in this thesis and provide relevant background.

2.1 Light sources

Underlying all of the experiments in this thesis is the generation of ultrafast pulses of light and the manipulation of these pulses to obtain desired characteristics. These characteristics include, but are not limited to, the center wavelength, the spectral width, the pulse duration, and the spatial profile. This section reviews the light sources used in the experiments described in the subsequent chapters and background on the theory of operation for these elements. This includes the fundamental pulsed light source (Nd:YAG femtosecond laser), optical parametric amplifiers, and white-light generation or supercontinuum generation.

2.1.1 Nd:YAG laser and pulsed lasers

The fundamental pulsed laser used in the projects described in Chapters 4 and 5 was a Nd:YAG femtosecond laser (Spectra-Physics Spirit 1040-8). This laser outputs

an average power of up to $8W$, has a central wavelength of 1040 nm, with a pulse duration of $\sim$ 300 fs, and a repetition rate of 208 kHz.

What are pulsed lasers and why are they interesting. Note that it allows us to access nonlinearities in material properties with high E-fields

2.2 Time-resolved Optics

Ultrafast spectroscopy is an umbrella term for a large number of techniques involving sub-picosecond pulsed lasers. Here, we focus on the applications used in condensed matter, and the specific techniques used in this thesis.

A common sub-category of ultrafast spectroscopy is pump-probe spectroscopy. This technique uses a sequence of one or more ultrafast pump pulses that perturbs the sample, either resonantly or non-resonantly, followed by a probe pulse that measures the change in optical properties of the material. The case of a two-beam pump-probe experiment is depicted in Fig. 2.1.

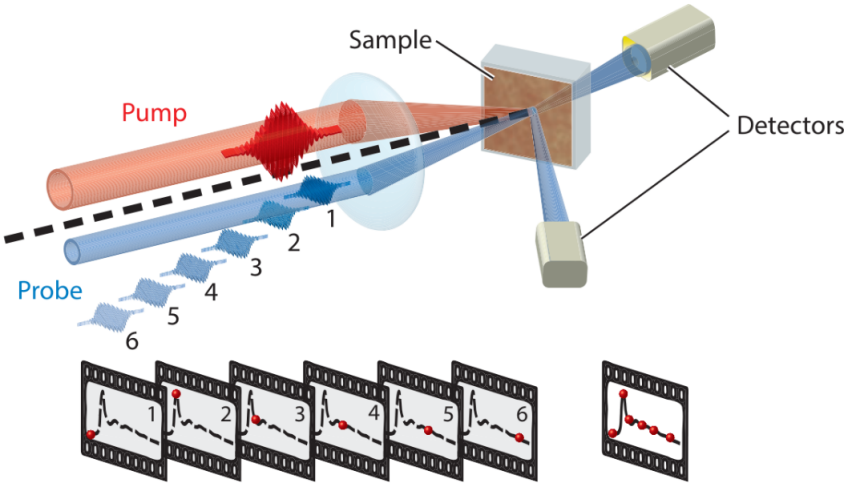

Figure 2.1: Schematic of two-beam pump-probe scheme. Adapted from [1]. Red pump pulse excites the sample. The blue probe pulse then interacts with the sample with some time delay with respect to the pump pulse. After interacting with the sample, the probe pulse goes into a detector to measure the optical response of the sample. By varying the pump-probe time delay, a time-resolved trace of the dynamics can be mapped out as shown at the bottom of the figure.

2.2.1 Time-resolved reflectivity

Time-resolved reflectivity ($\Delta R/R$) is an ultrafast pump-probe technique that measures the change in reflectivity as a function of time due to the interaction of the material with a pump pulse. Reflectivity indirectly reports on the dielectric properties of the material, and thus enables experimentalists to correspond photoinduced changes to modulation of the dielectric properties of the material. In theory, the simultaneous measurement of the time-resolved reflectivity and time-resolved transmissivity ($\Delta T/T$) of a material allows one to track photoinduced changes to the full complex dielectric function. However, this is not always practically viable.

Fig. 2.2 shows the basic experimental setup of a time-resolved reflectivity ($\Delta R/R$)

measurement. In this setup, the pulses originate from the Spirit system (Spectra-Physics, Spirit-1040-8), and will be referred to as the "fundamental beam". These pulses have a repetition rate of $f = 209kHz$, a wavelength of $\lambda = 1040 \pm 5$ nm, and a pulse duration of about $\tau \approx 350$ fs. In the setup depicted in Fig. 2.2, the pulses from the Spirit are directed into a noncollinear optical parametric amplifier (Spectra-Physics, Spirit-NOPA), where the fundamental beam can be converted to a tunable range of wavelengths $650 < \lambda < 850$ nm. These pulses can be compressed down to ~ 20 fs. After the Spirit-NOPA, the pulses go to a 90:10 beam splitter, where the 90% of the beam is transmitted to be used as a pump beam and 10% of the beam is reflected to be used as a probe beam.

The pump beam is then focused by a lens (not depicted) through an acousto-optic modulator (AOM, Brimrose, TEM-85-2) which is used to chop the pump at a high repetition rate. In this case, the AOM is modulated by a square wave at a frequency of 52.25 kHz, (1/4 the repetition rate of the laser). The beam is recollimated by a lens (not depicted) and then goes through a prism compressor comprised of a pair of double-pass prisms. This prism compressor is used to compensate for the positive group velocity dispersion in the rest of the setup, and thus minimize the pulse duration at the sample position. The pump pulses then go through a $\lambda/2$ wave-plate followed by a polarizer to purify the polarization. This allows for control of the polarization of the pump beam incident on the sample. The pump pulses are then directed onto a delay stage, which varies the arrival time of the pump pulse at the sample with respect to the probe pulse. The pump pulses often also go through a telescope (not depicted) to control the beam diameter and thus the spot size of the pump at the sample location. The pump pulses are then directed through a periscope that adjusts the beam height so that the pump can access the cryostat from above. The pump is then directed onto a three-axis translation stage that controls where the beam hits the sample and the focal distance. It is important that the beams are relatively parallel and collimated as they enter the periscope so that the beams

focus to the same point at the sample. Fine adjustment is usually necessary using a camera at the sample position.

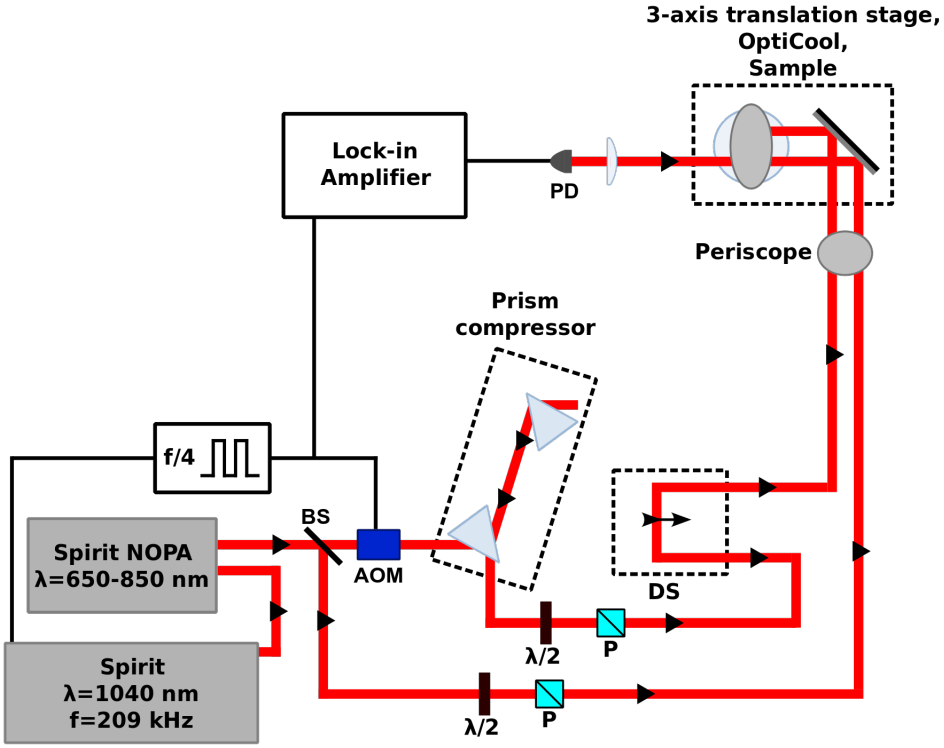

Figure 2.2: Schematic of optical pump-optical pump (OPOP) experiment in a magnetic field.

2.2.2 Magneto-optical effects

Static magneto-optical effects

Magneto-optical effects are a well-documented optical phenomena that dates back to the 19th century. Magneto-optical effects are generally defined by interactions between light and matter in the presence of an external magnetic field or magnetic ordering in the material under investigation. These phenomena have found many uses

in the experimental study of condensed matter systems as one can track the magnetic behavior of a system via its interaction with light. For example, the magnetization as a function of thermodynamic variables, the magnetic specific heat can be measured [2], and time-resolved ultrafast dynamics of a sample's magnetic ordering have all been observed through the use of magneto-optical techniques.

There are many different magneto-optical effects with various names throughout literature. For example, there is the Faraday effect (magnetic circular birefringence, MCB, in transmission), the polar Kerr effect (magnetic circular birefringence, MCB, in reflection), magnetic circular dichroism (MCD or magneto-optical ellicipticity), the Cotton-Mouton or Voigt effect (magnetic linear birefringence, MLB), and magnetic linear dichroism (MLD).

It is important to consider the relative orientation of the propagation vector of light $\vec{k}$ and the magnetic field $\vec{H}$ (or magnetization $\vec{M}$) when categorizing these effects. The two basic geometries are the:

1. Faraday geometry: light propagates parallel to magnetic field ($\vec{k} \parallel \vec{H}$)
2. Voigt geometry: light propagates perpendicular to magnetic field ($\vec{k} \perp \vec{H}$)

Typically, the Faraday geometry is associated with circular birefringence and dichroism, while the Voigt geometry is associated with linear birefringence and dichroism.

The connection between magneto-optical effects and the sample magnetization is established via the dielectric permittivity tensor ϵ_{ij}. Note that it is generally well-accepted that at optical frequencies, the magnetic susceptibility is negligible $\chi_M = 0$, and the optical response can be understood fully from the dielectric permittivity.

Consider the linear response dielectric response where $\vec{D} = \epsilon\vec{E}$ and

$$\epsilon = \begin{pmatrix} \epsilon_{xx} & \epsilon_{xy} & \epsilon_{xz} \\ \epsilon_{yx} & \epsilon_{yy} & \epsilon_{yz} \\ \epsilon_{zx} & \epsilon_{zy} & \epsilon_{zz} \end{pmatrix}, \tag{2.1}$$

where each element of the tensor is complex: $\epsilon_{ij} = \epsilon'_{ij} + i\epsilon''_{ij}$. Recall that the real component of the dielectric function corresponds to the lossless response of the material, and the imaginary component corresponds to the losses in the material. The magnetization can lead to small changes in the dielectric permittivity, allowing us to Taylor expand the elements of the permittivity in terms of magnetization components M_k:

$$\epsilon_{ij} = \epsilon^0_{ij} + K_{ijk}M_k + G_{ijkl}M_kM_l + \ldots, \tag{2.2}$$

where $i, j, k, l \in \{x, y, z\}$, ϵ^0_{ij} is the non-magnetic permittivity, and K_{ijk} and G_{ijkl} are the first- and second- order magneto-optical coefficients. Magneto-optical techniques allow us to measure the different components of the permittivity tensor as a function of magnetization or magnetic field. According to Onsager's reciprocity relations, the diagonal elements must be even under time-reversal while the off-diagonal elements must be odd under time-reversal. That is, since $\vec{M}$ is odd under time-reversal, we have $\epsilon_{ii}(-\vec{M}) = \epsilon_{ii}(\vec{M})$ and $\epsilon_{ij}(-\vec{M}) = -\epsilon_{ij}(\vec{M})$ for $i \neq j$ [3, 4, 5]. Thus, magneto-optic effects that are linear in magnetization, such as Faraday and Kerr rotation, are due to the off-diagonal terms in the permittivity tensor. With these phenomenological relations in mind, we can then relate the components of the permittivity tensor to the measured magneto-optical quantities.

Dielectric tensor to MOKE angle

For concreteness, consider an isotropic medium such as a gas or liquid. In the absence of a magnetic field to break time-reversal symmetry, the dielectric tensor reduces to:

$$\epsilon = \begin{pmatrix} \epsilon_{xx} & 0 & 0 \\ 0 & \epsilon_{xx} & 0 \\ 0 & 0 & \epsilon_{xx} \end{pmatrix}. \tag{2.3}$$

In the simplest case, we can introduce uniaxial magnetization $\vec{M}$ along the z-axis. This causes uniaxial anisotropy along the z-direction, modifying our dielectric func-

tion to:

$$\epsilon = \begin{pmatrix} \epsilon_{xx}(\vec{M}) & \epsilon_{xy}(\vec{M}) & 0 \\ -\epsilon_{xy}(\vec{M}) & \epsilon_{xx}(\vec{M}) & 0 \\ 0 & 0 & \epsilon_{zz}(\vec{M}) \end{pmatrix} \tag{2.4}$$

In order to understand how this dependence on magnetization affects the propagation of light, consider the response of circularly polarized light. In the circularly polarized basis, the dielectric tensor elements become:

$$\epsilon_{\pm} = \epsilon_{xx} \pm i\epsilon_{xy} = (n_{\pm} + ik_{\pm})^2 \tag{2.5}$$

Thus, the phase velocities and absorption of the two circularly polarizations directly depends on ϵ_{xy}. Since linearly polarized light is a linear combination of right-hand circularly polarized and left-hand circularly polarized light, a difference in phase velocities and absorptions of the two circular polarizations lead to a polarization rotation and a change in ellipticity of the light, respectively. This allows us to discern changes to the magnetic properties of the material by observing changes to the polarization rotation and ellipticity of our probe beam.

The primary magneto-optical technique used in this text is the polar magneto-optical Kerr effect (MOKE). Phenomenologically, it is commonly observed that the Kerr rotation and ellipticity is proportional to the static magnetization in the sample. That is,

$$\Theta^K \propto M. \tag{2.6}$$

We can quantify a complex MOKE angle:

$$\tilde{\Theta}^K = \theta^K + i\eta^K, \tag{2.7}$$

where θ^K and η^K are real and correspond to the Kerr rotation and Kerr ellipticity, respectively. Experimentally, the polarization rotation and ellipticity can be observed by measuring the polarization-resolved reflectance. That is, for a reflectance defined

by

$$\begin{pmatrix} E_s^r \\ E_p^r \end{pmatrix} = \begin{pmatrix} r_{ss} & r_{sp} \\ r_{ps} & r_{pp} \end{pmatrix} \begin{pmatrix} E_s^i \\ E_p^i \end{pmatrix}, \tag{2.8}$$

the complex MOKE angles are given by:

$$\begin{aligned} \tilde{\Theta}_s^K &= \frac{r_{ps}}{r_{ss}} \\ \tilde{\Theta}_p^K &= \frac{r_{sp}}{r_{pp}}. \end{aligned} \tag{2.9}$$

To show that the Kerr rotation (ellipticity) are proportional to the magnetization, consider the polar Kerr geometry of an isotropic medium with magnetization along the z-direction. That is, the incident light will be propagating along the z-direction and reflect off of the material near normal incidence. For simplicity and without loss of generality, suppose the incident electric field has s-polarization:

$$\begin{aligned} \vec{E}_s^i &= E_s^i \hat{e}_s, \\ \vec{E}_r &= E_s^i r_{ss} \hat{e}_s + E_s^i r_{ps} \hat{e}_p, \end{aligned} \tag{2.10}$$

where $\hat{e}_{s(p)}$ are the unit basis vectors along the s- (p-) directions. It is convenient to express this in the circularly polarized basis:

$$\begin{aligned} \hat{e}_\pm &= \frac{1}{\sqrt{2}}(\hat{e}_s \mp i\hat{e}_p), \\ \vec{E}_s^i &= \frac{E^i}{\sqrt{2}}(\hat{e}_+ + \hat{e}_-), \\ \vec{E}^r &= \frac{1}{\sqrt{2}}(E_{r_+}\hat{e}_+ + E_{r_-}\hat{e}_-). \end{aligned} \tag{2.11}$$

We can then relate the reflectance coefficients to the dielectric function via the Fresnel equations near normal incidence [6]. In the circularly polarized basis, the reflectance is given by:

$$r_\pm = r_{ss} \pm i r_{ps} = \frac{\tilde{n}_\pm - 1}{\tilde{n}_\pm + 1}, \tag{2.12}$$

where $\tilde{n}_\pm = n_\pm + ik_\pm$ is the complex refractive index. Plugging Eqn. 2.12 into Eqn. 2.11, we have:

$$
\begin{aligned}
E_{r_+} &= \frac{E_s^i}{2}\left(\frac{n_+ - 1}{n_+ + 1} + \frac{n_- - 1}{n_- + 1}\right) \\
E_{r_-} &= -i\frac{E_s^i}{2}\left(\frac{n_+ - 1}{n_+ + 1} + \frac{n_- - 1}{n_- + 1}\right)
\end{aligned}
\tag{2.13}
$$

Going back to the linear basis, we have

$$
\begin{aligned}
r_{ss} &= \frac{r_+ + r_-}{2} \\
r_{ps} &= \frac{-i(r_+ - r_-)}{2}
\end{aligned}
\tag{2.14}
$$

Combining the above equations, the complex MOKE angle is

$$
\tilde{\Theta}_s^K = \frac{i\epsilon_{xy}}{\sqrt{\epsilon_{xx}(\epsilon_{xx} - 1)}}. \tag{2.15}
$$

Thus, we can relate the complex Kerr angle to the magnetization: $\tilde{\Theta}^K \propto |\vec{M}|$.

Time-resolved MOKE

The above section describes magneto-optical effects with respect to static magnetization. This can then be extended to photo-induced changes to magneto-optic properties. We can phenomenologically relate the time-dependent complex polarization rotation to the time-dependent magnetization [5]:

$$
\tilde{\Theta}(t) = N(t) + \sum_{i=x,y,z} \tilde{F}_i(t)\, M_i(t), \tag{2.16}
$$

where $N(t)$ is time-dependent rotation/ellipticity due to sources that do not break time-reversal symmetry, $\tilde{F}_i(t)$ is the time-dependent effective Fresnel coefficient relating the complex Kerr angle to the magnetization, and $M_i(t)$ is the time-dependent magnetization of the material. We can isolate the magnetic term of the complex Kerr angle measuring the complex Kerr angle at under opposite magnetization directions:

$$
\tilde{\Theta}^K(t) = \frac{1}{2}\left(\tilde{\Theta}\left(+\vec{M}(t)\right) - \tilde{\Theta}\left(-\vec{M}(t)\right)\right). \tag{2.17}
$$

In the case of the polar MOKE geometry, only the out-of-plane M_z component is measured, simplifying the above equation to:

$$\tilde{\Theta}^K(t) = \tilde{F}(t) \cdot M_z(t). \tag{2.18}$$

We can describe pump-induced changes to the complex Kerr angle $\Delta\tilde{\Theta}(t)$ by:

$$\Delta\tilde{\Theta}^K(t) = \tilde{F}_0\, \Delta M_z(t) + \Delta\tilde{F}_0\, M_{z,0}, \tag{2.19}$$

where $\tilde{F}_0$ and $M_{z,0}$ are the equilibrium effective Fresnel coefficient and magnetization, respectively. Defining the equilibrium complex Kerr angle as $\tilde{\Theta}_0^K \equiv \tilde{F}_0\, M_{z,0}$, we can re-write the expression above as

$$\frac{\Delta\tilde{\Theta}^K}{\tilde{\Theta}_0^K}(t) = \frac{\Delta M_z(t)}{M_{z,0}} + \frac{\Delta\tilde{F}_0}{\tilde{F}_0}. \tag{2.20}$$

Experimental implementation

Here, we describe how to measure the polar magneto-optical Kerr effect (MOKE). The basic components needed to measure MOKE polarization rotation (ellipticity) are a linearly polarized coherent light source (laser), a sample of interest, a $\lambda/2$ waveplate ($\lambda/4$ waveplate), a Wollaston prism (or equivalent polarization analyzer), and a photodetector. To formalize how the light interacts with each component, we use the Jones matrix formalism, or Jones calculus [7]. Here, the polarization state of light is represented by a 2×1 Jones vector, and optical elements are represented by Jones matrices. The resulting polarization of light propagating through various optical elements can then be represented by a series of matrix multiplications.

In this case, consider linearly polarized light in the linearly polarized basis spanned by s-polarized light and p-polarized light:

$$\vec{E} = \begin{pmatrix} E_s \\ E_p \end{pmatrix}. \tag{2.21}$$

The sample and the $\lambda/2$ waveplate Jones matrices are, respectively, given by:

$$\overline{R} = \begin{pmatrix} r_{ss} & r_{sp} \\ r_{ps} & r_{pp} \end{pmatrix} = r_{ss} \begin{pmatrix} 1 & \tilde{\Theta}_p^K \\ \tilde{\Theta}_s^K & r_{pp}/r_{ss} \end{pmatrix}, \tag{2.22}$$

$$\overline{J}_{\lambda/2} = \begin{pmatrix} \cos 2\phi & \sin 2\phi \\ \sin 2\phi & -\cos 2\phi \end{pmatrix}, \tag{2.23}$$

where we used Eqn. 2.9 was used in Eqn. 2.22.

In general, if there is a periscope in the experimental setup or any elements that rotate the polarization after the sample, note that this can be compensated for by the $\lambda/2$ waveplate.

The Wollaston prism acts to separate orthogonal polarizations of light into two separate beams, so to the end of determining the final polarization state of light, the Wollaston prism acts to measure this final polarization state and can thus be ignored in our Jones calculus. Thus, we have:

$$\begin{aligned} \vec{E}^r &= \overline{J}_{\lambda/2} \overline{R} \vec{E}^i, \\ \begin{pmatrix} E_s^r \\ E_p^r \end{pmatrix} &= \begin{pmatrix} \cos 2\phi & \sin 2\phi \\ \sin 2\phi & -\cos 2\phi \end{pmatrix} \begin{pmatrix} r_{ss} & r_{sp} \\ r_{ps} & r_{pp} \end{pmatrix} \begin{pmatrix} E_s^i \\ E_p^i \end{pmatrix} \end{aligned} \tag{2.24}$$

To isolate $r_{ps(sp)}$, one can set the effective $\lambda/2$ waveplate angle ϕ to $\phi = \pi/8$. This simplifies the dependence of $\vec{E}^r$ on r_{ss}, r_{sp}. In practice, this can be done ensuring that the intensities out of the two arms of the Wollaston prism are equal in the absence of sample-dependent polarization rotation. This can be done by setting the $\lambda/2$ waveplate angle while the sample is not magnetized. Alternatively, one can use a reference sample where the lack of polarization rotation is known (e.g. a gold mirror). Taking this into account, for incident light with s-polarization, the reflected

light has a polarization state given by:

$$\begin{aligned}\begin{pmatrix} E_s^r \\ E_p^r \end{pmatrix} =& \frac{1}{2}\begin{pmatrix} 1 & 1 \\ 1 & -1 \end{pmatrix}\begin{pmatrix} r_{ss} & r_{sp} \\ r_{ps} & r_{pp} \end{pmatrix}\begin{pmatrix} E_s^i \\ 0 \end{pmatrix} \\ =& \frac{E_s^i}{2}\begin{pmatrix} r_{ss}+r_{ps} \\ r_{ss}-r_{ps} \end{pmatrix}.\end{aligned} \tag{2.25}$$

We are ultimately measuring the intensity of light via photodetectors. This means that we are measuring the square of the electric field: $I = |E|^2$. The Kerr angle can then be obtained by measuring the difference in intensities of the two orthogonal polarizations of the reflected light:

$$\begin{aligned} I_\theta &= I_s^r - I_p^r \\ &= |E_s^r|^2 - |E_p^r|^2 \\ &= |E_s^i|^2 |r_{ss}|^2 \left(\frac{r_{ps}}{r_{ss}} + \frac{r_{ps}^*}{r_{ss}^*}\right) \\ &= |E_s^i|^2 |r_{ss}|^2 \left(\tilde{\Theta}_s^K + \tilde{\Theta}_s^{K*}\right) \\ &= 2|E_s^i|^2 \, R \, \theta_s^K, \end{aligned} \tag{2.26}$$

where the $(\ldots)^*$ represents the complex conjugate, $R = |r_{ss}|^2$ is the reflectivity, and θ_s^K is the real part of the complex MOKE angle from Eqn. 2.7. This method allows for a background-free detection of the MOKE angle.

Similarly, we can measure the MOKE ellipticity η^K by replacing the $\lambda/2$ waveplate with a $\lambda/4$ waveplate. Similarly, we must set the effective $\lambda/4$ waveplate angle such that the two arms of the Wollaston prism are equal in the absence of sample-dependent polarization rotation. For incident light with s-polarization, the reflected light has a polarization state:

$$\begin{aligned}\begin{pmatrix} E_s^r \\ E_p^r \end{pmatrix} =& \frac{1}{4i}\begin{pmatrix} 1+i & 1-i \\ 1-i & 1+i \end{pmatrix}\begin{pmatrix} r_{ss} & r_{sp} \\ r_{ps} & r_{pp} \end{pmatrix}\begin{pmatrix} E_s^i \\ 0 \end{pmatrix} \\ =& \frac{E_s^i}{4i}\begin{pmatrix} r_{ss}(1+i)+r_{ps}(1-i) \\ r_{ss}(1-i)-r_{ps}(1+i) \end{pmatrix}.\end{aligned} \tag{2.27}$$

Again, the ellipticity can be obtained by taking the difference in intensities of the two orthogonal polarizations of the reflected light:

$$\begin{aligned} I_\eta &= I_p^r - I_s^r \\ &= |E_p^r|^2 - |E_s^r|^2 \\ &= |E_s^i|^2 |r_{ss}|^2 \left(\frac{r_{ps}}{r_{ss}} - \frac{r_{ps}^*}{r_{ss}^*} \right) \\ &= |E_s^i|^2 |r_{ss}|^2 \left(\tilde{\Theta}_s^K - \tilde{\Theta}_s^{K*} \right) \\ &= 2|E_s^i|^2 \, R \, \eta_s^K. \end{aligned} \tag{2.28}$$

We can also use this result to relate the time-dependent MOKE rotation and ellipticity $\Delta I_\theta(t)$ and $\Delta I_\eta(t)$:

$$\Delta I_\theta(t) = 2I_0^i R_0 \Delta\theta(t) + 2I_0^i \Delta R(t) \theta_0, \tag{2.29}$$

$$\Delta I_\eta(t) = 2I_0^i R_0 \Delta\eta(t) + 2I_0^i \Delta R(t) \eta_0, \tag{2.30}$$

where I_0^i is the intensity of the incident probe light, R_0 is the equilibrium reflectivity of the probe before photoexcitation, and θ_0 and η_0 are the equilibrium MOKE rotation and ellipticity before photoexcitation, respectively.

2.3 Optical parametric amplifiers

For a more complete description of the theory of optical parametric amplification, refer to [8, 9, 10]. Optical parametric amplification (OPA) is an optical process where pump photons at frequency ω_p are converted to pairs of lower energy signal ω_s and idler ω_i photons via a second-order ($\chi^{(2)}$) process in β-BaB_2O_2 (BBO). Due to the non-linear nature of this process, an intense pump field is required. A low intensity seed pulse is generally required in order to seed the amplification, whereas without the presence of a seed field, the process is referred to as spontaneous parametric

down conversion. Conservation of energy dictates that

$$\omega_p = \omega_s + \omega_i, \tag{2.31}$$

where by convention, $\omega_s < \omega_i$.

These photons must also conserve crystal momentum:

$$\vec{k}_p = \vec{k}_s + \vec{k}_i, \tag{2.32}$$

where $\vec{k}_p, \vec{k}_s, \vec{k}_i$ are the wave vectors of the pump, signal, and idler photons, respectively. This condition of conservation of momentum is also referred to as the phase matching condition. In general, phase matching cannot be achieved in isotropic materials with normal dispersion (eg. materials with a refractive index $n(\omega)$ increasing monotonically with frequency). Typically, this is solved by using birefringent materials where the dispersion depends on crystalline axes along which the light is polarized. The linear optical classifications of various common crystal families is shown in Table 2.1.

I shall describe uniaxial crystals as these are used in this thesis for optical parametric amplication. The most commonly used medium for optical parametric amplification is β-BaB_2O_2 (BBO). Uniaxial crystals refers to crystals where there is a single optic axis (not to be confused with an optical axis). An **optic axis** is defined as the axis along which light propagates without experiencing birefringence. Light propagating parallel to this axis behaves as if the material is isotropic, and the refractive index $n_o(\omega)$ ('o' for ordinary) will be independent of the polarization of the light. In other words, light which has polarization perpendicular to the optic axis will have the same index of refraction, $n_o(\omega)$, even if the light is not propagating along the optic axis. Thus, we refer to light polarized perpendicular to the optic axis as having "ordinary polarization". In contrast, if the polarization of light is parallel to the optic axis, the refractive index will be $n_e(\omega)$ and be referred to as "extraordinary polarization". These two refractive indices constitute the extreme values that the

refractive index may take at a given frequency ω. Uniaxial crystals can be further subdivided into two classifications: if $n_e(\omega) - n_o(\omega) > 0$, it is considered a positive uniaxial crystal; if $n_e(\omega) - n_o(\omega) < 0$, it is considered a negative uniaxial crystal. BBO is a negative uniaxial crystal.

Table 2.1: Optical classifications of various crystal families [9]

Crystal families	Linear optical classification
Cubic	Isotropic
Trigonal, tetragonal, hexagonal	Uniaxial
Triclinic, monoclinic, orthorhombic	Biaxial

Returning to the topic of phase matching for optical parametric amplification, we can now describe the types of phase matching. In order to achieve phase matching, the highest frequency light must have the lowest possible refractive index. In the case of optical parametric ampliciation in BBO, as it is a negative uniaxial crystal, this implies that the pump photons must be polarized along the extraordinary axis. With this fixed, we are left with the two types of phase matching: Type I phase matching where the signal and idler have parallel polarizations along the ordinary axis, and Type II phase matching where signal and idler have perpendicular polarizations. These are summarized in Table 2.2.

Table 2.2: Types of phase matching ($\omega_p > \omega_s > \omega_i$)

Phase matching type	Pump polarization	Signal polarization	Idler polarization
Type I	e	o	o
Type IIA	e	o	e
Type IIB	e	e	o

In order to optimize the phase matching condition (ie. $\Delta k = k_s + k_i - k_p = 0$), one must carefully tune the polarization and propagation angles with respect to the optic axes of the nonlinear medium to maximize the OPA efficiency. Fig. 2.3 shows phase matching curves for BBO with a pump wavelength of $\lambda_p = 0.4\mu m$.

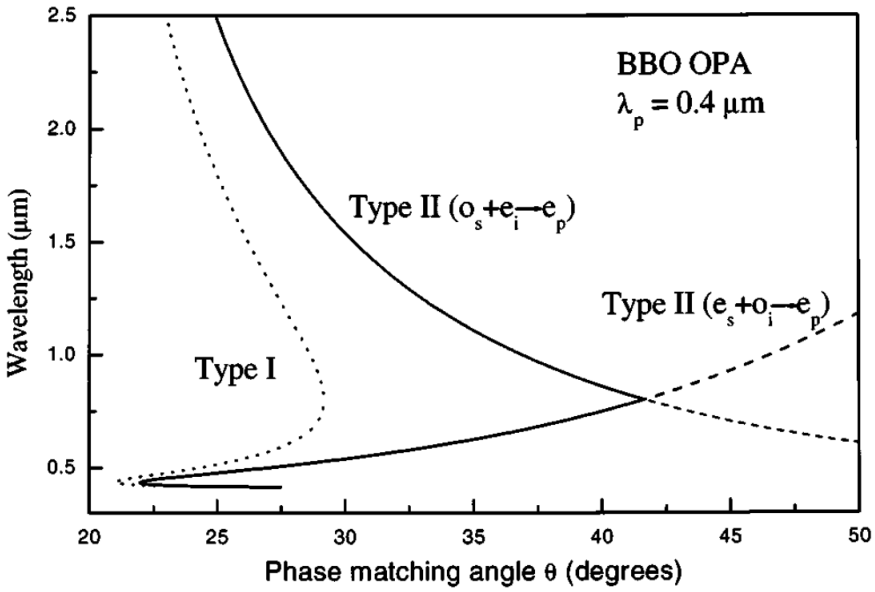

Figure 2.3: Phase matching curve for BBO adapted from [10]. The curves show the (optimal) signal wavelength given by the phase matching angle. These curves are dependent on the material (BBO), pump wavelength ($\lambda_p = 0.4\mu m$, and phase matching type (see labels).

Phase matching is principally achieved by cutting the nonlinear crystal such that the surface normal is close to the optimal phase matching angle with respect to the optic axis for your pump wavelength of choice. Most commercially available BBO crystals are sold with the proper cuts. Generally, one needs to finely tune the angle of incidence of the beams, and this is done by rotating the crystal about an axis parallel to the ordinary direction of polarization.

Chapter 3

Quantum spin liquids and Mott insulators

3.1 Introduction

3.2 $j_{eff} = 1/2$ ground state in spin-orbit coupled Mott insulators

The necessary ingredients needed for constructing the j_{eff} picture are (1) strong spin-orbit coupling of participating electrons and (2) a strong cubic crystal field environment. We are primarily interested in transition metal compounds with partially filled d orbitals and an octahedral crystal field environment for the realization of these $j_{eff} = 1/2$ states.

The schematic for going from d-orbitals to $j_{eff} = 1/2$ states is shown in Fig. 3.1. In this example, we consider the IrO_6 octahedra where the ground state is in the $5d^5$ configuration. The octahedral crystal field splits the orbital degeneracy of the d-orbitals into a lower energy t_{2g} triplet and a higher energy e_g doublet, where

the crystal field gap $\Delta = 10Dq \sim 2$ eV [11] and $D = \frac{35ze}{16\pi\epsilon_0 a^5}$ and $q = \frac{2e}{105}\langle r^4 \rangle$. When the full orbital momentum operator $\vec{L}$ is projected onto the t_{2g} manifold, the effective orbital momentum $-\vec{L}_{eff}$ with $l = 1$ [12]: $|l_z = 0\rangle \equiv |d_{xy}\rangle$, $|l_z = \pm 1\rangle \equiv -\frac{1}{2}(i|d_{xz}\rangle \pm |d_{yz}\rangle)$.

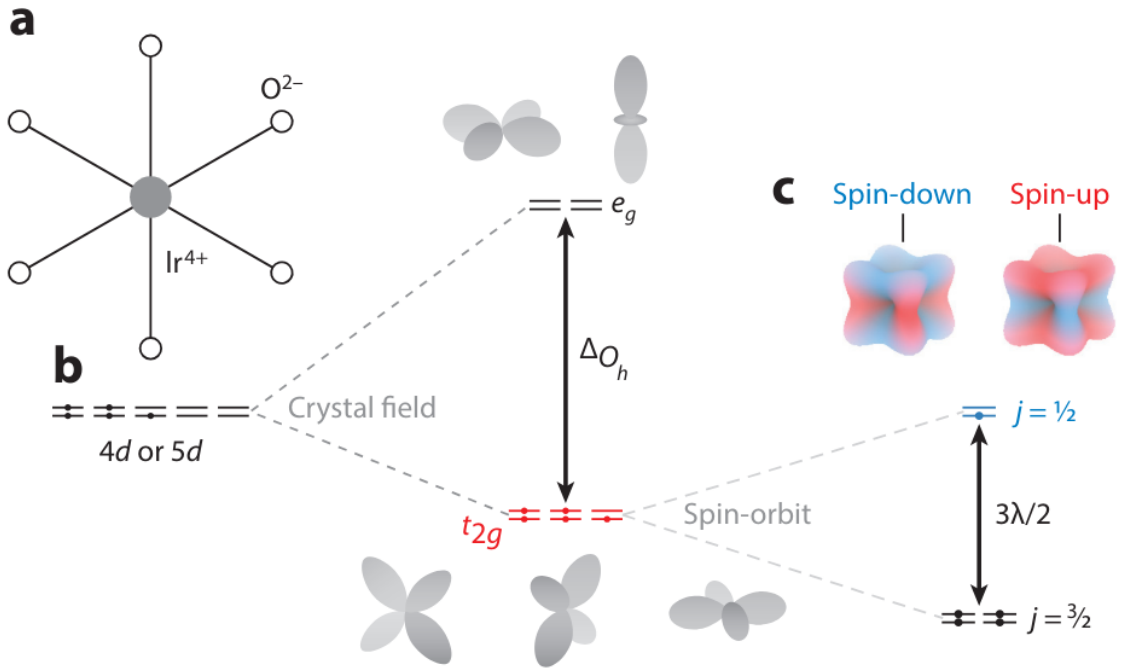

Figure 3.1: Schematic of d-orbitals giving rise to $j_{eff} = 1/2$ states due to crystal field effects and spin-orbit coupling. Adapted from [13].

For a sufficiently large crystal field energy, we can ignore the correlations with the e_g manifold and consider the t_{2g} states independently. The spin-orbit interaction, $H_{SOC} = -\lambda \vec{L} \cdot \vec{S}$, further splits the degeneracy of the t_{2g} multiplet into a higher-energy $j_{eff} = 1/2$ doublet and a lower-energy $j_{eff} = 3/2$ quartet. In the t_{2g} basis,

these states can be written as:

$$
\begin{aligned}
|j_{eff} = \frac{1}{2}, m_{j_{eff}} == \pm\frac{1}{2}\rangle &= \frac{1}{\sqrt{3}}\left(|d_{yz}, \mp\rangle \pm i|d_{xz}, \mp\rangle \pm |d_{xy}, \pm\rangle\right), \\
|j_{eff} = \frac{3}{2}, m_{j_{eff}} == \pm\frac{3}{2}\rangle &= \frac{1}{\sqrt{2}}\left(|d_{yz}, \pm\rangle \pm i|d_{xz}, \pm\rangle\right), \\
|j_{eff} = \frac{3}{2}, m_{j_{eff}} == \pm\frac{1}{2}\rangle &= \frac{1}{\sqrt{6}}\left(|d_{yz}, \mp\rangle \pm i|d_{xz}, \mp\rangle - 2|d_{xy}, \pm\rangle\right),
\end{aligned}
\tag{3.1}
$$

where $|d_{yz}, \mp\rangle$, $|d_{xz}, \mp\rangle$, and $|d_{xy}, \mp\rangle$ are the spin-up and spin-down t_{2g} states. The $j_{eff} = 1/2$ and $j_{eff} = 3/2$ states are separated by a gap of $3\lambda/2$.

We then move on to describe the interactions between the $j_{eff} = 1/2$ electrons. In the case of Ir^{4+}, we have a half-filled $j_{eff} = 1/2$ level. We can describe the full t_{2g} manifold using a multiorbital model [13]:

$$
\begin{aligned}
H = &\sum_{ij}\sum_{\alpha\beta}\sum_{\sigma} t_{ij}^{\alpha\beta}\left(d_{i,\alpha,\sigma}^{\dagger} d_{j,\beta,\sigma} + h.c.\right) \\
&+ \sum_{i}\left[\left(\frac{U - 3J_H}{2}\right)(N_i - 5)^2 - 2J_H\vec{S}_i^2 - \frac{J_H}{2}\vec{L}_i^2 - \lambda\vec{L}_i\cdot\vec{S}_i\right],
\end{aligned}
\tag{3.2}
$$

where in the first sum, $d_{i,\alpha,\sigma}^{\dagger}$ is the creation operator acting on the t_{2g} states in orbital $\alpha = d_{yz}, d_{xz}$, or d_{xy} with spin $\sigma = \uparrow, \downarrow$ at site r_i. $t_{ij}^{\alpha\beta}$ is the tight-binding hopping parameter. U is the on-site Coulomb interaction, J_H is the Hund's coupling, and N_i, $\vec{S}_i$ and $\vec{L}_i$ is the total number operator, the total spin operator, and the total pseudo-angular momentum operator at site $\vec{r}_i$, respectively. The 5 adds a chemical potential to favor the $N = 5$ states found in the d^5 states of Ir^{4+} and Ru^{3+} ions. This model fixes the interorbital repulsion to the free ion value $U - 2J_H$. For Ir^{4+} ions, one typically expects $U \sim 2$ eV, $J_H \sim 0.2$ eV, and $3\lambda/2 \sim 0.4 - 0.5$ eV.

This can be further simplified by assuming the $j_{eff} = 1/2$ and $j_{eff} = 3/2$ bands are well separated, allowing the interband interactions to be neglected. This simplifies Eqn. 3.2 to the Hubbard model [14, 13]:

$$
H = \sum_{ij}\sum_{\sigma=\pm} t_{ij}\left(c_{i\sigma}^{\dagger} c_{j\sigma} + h.c.\right) + U_{eff}\sum_{i} n_{i+}n_{i-},
\tag{3.3}
$$

where $c^{\dagger}_{i\pm}$ creates a $j_z = \pm 1/2$ electron at site $\vec{r}_i$, t_{ij} is the hopping parameter, and $U_{eff} \sim U - \frac{4}{3}J_H$. In the strong Mott limit where $U_{eff} \gg t$ and t is the nearest-neighbor hopping parameter, the low-energy physics is dictated by the super-exchange $J \sim t^2/U_{eff}$ [13, 15]:

$$H = \sum_{ij} J\vec{S}_i \cdot \vec{S}_j = \frac{4t^2}{U_{eff}} \sum_{ij} \vec{S}_i \cdot \vec{S}_j, \tag{3.4}$$

where the sum is over nearest neighbors $\vec{r}_i$ and $\vec{r}_j$ and $\vec{S}_i$ is the pseudo-spin $j_{eff} = 1/2$ at site $\vec{r}_i$. However, the above equation only considers isotropic exchange interactions whereas, given the spin-orbit nature of the $j_{eff} = 1/2$ moments, it is generally expected that interactions are highly anisotropic and can thus be cast into the form [12, 16]:

$$H = \sum_{ij} J\vec{S}_i \cdot \vec{S}_j + \vec{D}_{ij} \cdot (\vec{S}_i \times \vec{S}_j) + \vec{S}_i \cdot \overline{\overline{\Gamma}}_{ij} \cdot \vec{S}_j, \tag{3.5}$$

where J is the isotropic Heisenberg interaction, $\vec{D}_{ij}$ is the Dzyaloshinskii–Moriya (DM) vector, and $\overline{\overline{\Gamma}}_{ij}$ is the symmetric pseudo-dipolar tensor.

Pedagogical interlude

We describe the crystal field effects and spin-orbit coupling in more detail following [17].

In a fully isotropic environment without spin-orbit coupling, as seen in Fig. 3.1(a), the d-orbitals are fully degenerate with orbital momentum $|L| = 2$. An octahedral crystal field can break this degeneracy as, for example, spatial overlap between the neighboring ligands differs for the different d-orbitals. We can consider how this affects the effective orbital momentum of the orbitals by considering the expectation value of L_z in the basis of the d-orbitals. The basis is given by $|\psi_\alpha\rangle = \{|d_{xz}\rangle, |d_{yz}\rangle, |d_{xy}\rangle, |d_{3r^2-z^2}\rangle, |d)x^2 - y^2\rangle\}$. $\langle L_z\rangle$ is then:

$$\langle\psi_\alpha|L_z|\psi_\alpha\rangle = \left(\begin{array}{ccc|cc} 0 & i & 0 & 0 & 0 \\ -i & 0 & 0 & 0 & 0 \\ 0 & 0 & 0 & 0 & 2i \\ \hline 0 & 0 & 0 & 0 & 0 \\ 0 & 0 & 2i & 0 & 0 \end{array}\right).$$

The top left corner corresponds to the t_{2g} subspace, whereas the bottom right corner corresponds to the e_g subspace. Note that the t_{2g} subspace has the same expectation values of L_z as that of p-orbitals up to a minus sign. In fact, the total orbital momentum of the t_{2g} subspace has the same form as p-orbitals, up to a minus sign. That is, $\vec{L}_{t_{2g}} = -\vec{L}_p$. Thus, the effective orbital momentum is $|L_{t_{2g}}| = 1$ and $|L_{e_g}| = 0$. Therefore, the effective total angular momentum for the t_{2g} states are

$$\begin{aligned} \vec{j}_{eff} &= \vec{L}_{t_{2g}} + \vec{S} = -\vec{L}_p + \vec{S} \\ |\vec{j}_{eff}| &= \left\{\frac{1}{2}, \frac{3}{2}\right\}. \end{aligned} \tag{3.6}$$

Here, j_{eff} is a good quantum number and the states $|j_{eff}, m_{j_{eff}}\rangle$ are given in Eqn. 3.1. It is the spin orbit interaction that splits the $j_{eff} = 1/2$ and $j_{eff} = 3/2$ states.

The spin-orbit interaction is due to the interaction between the intrinsic spin of an electron $\vec{S}$ and the orbital motion of the electron relative to the nucleus of the atom. Generally, in a solid where the electrons are non-interacting, this interaction takes the general form of [18]:

$$H_{SO} = \frac{\hbar}{4m_0^2c^2}\vec{\sigma}\cdot[\nabla V(\vec{r}\times\vec{p})], \tag{3.7}$$

where m_0 is the electron mass, $V(\vec{r})$ is the effective Kohn-Sham potential, and $\sigma_{i=x,y,z}$ are the Pauli spin matrices. The mean value of the spin-orbit interaction takes the common form:

$$H_{SO} = \lambda\vec{L}\cdot\vec{S} \tag{3.8}$$

where $\vec{S} = \frac{1}{2}\vec{\sigma}$, $\vec{L} = \vec{r} \times \vec{p}$, and the spin-orbit coupling constant λ is

$$\lambda_{(nl)} = \frac{\hbar}{2m_0^2c^2} \left\langle \frac{1}{r}\frac{dV}{dr} \right\rangle_{(n,l)} . \tag{3.9}$$

where $\langle \ldots \rangle_{(nl)}$ is the mean value of the radial quantity in the state with quantum number (nl). Values for the spin orbit coupling λ are shown for some transition metals are shown in Table 3.1 adapted from [18].

Table 3.1: Spin-orbit coupling of d-valence electrons in various transition metals. Adapted from [18] Table 3.

Atom	Z	λ (eV)
Fe	26	0.050
Co	27	0.061
Cu	29	0.103
Ru	44	0.161
Rh	45	0.191
Ag	47	0.227
Os	76	0.31
Ir	77	0.40
Au	79	0.42

The energy splitting between the $j_{eff} = 1/2$ and $j_{eff} = 3/2$ states can be determined by considering the difference between the eigenvalues of $\vec{L}\cdot\vec{S} = \frac{1}{2}(\vec{J}^2 - \vec{L}^2 - \vec{S}^2)$ [15]:

$$\begin{aligned} \Delta E_{SO} &= \langle 1/2, 1/2|\lambda\vec{L}\cdot\vec{S}|1/2, 1/2\rangle - \langle 3/2, 3/2|\lambda\vec{L}\cdot\vec{S}|3/2, 3/2\rangle \\ &= \lambda - (-\frac{1}{2}\lambda) \\ &= \frac{3}{2}\lambda. \end{aligned} \tag{3.10}$$

3.3 Bond-directional exchange interactions

Here, we describe how bond-directional exchange interactions can arise in these $j_{eff} = 1/2$ systems. These systems can materially be found in transition metal oxide

systems, where the octahedral cage surrounding the $4d$ and $5d$ transition metal ions are composed of oxygen ligands. Khaliullin [19] and later Jackeli and Khaliullin [12] showed that certain idealized TM-O-TM bond geometries can host exchange interactions that depend on the direction of bonding.

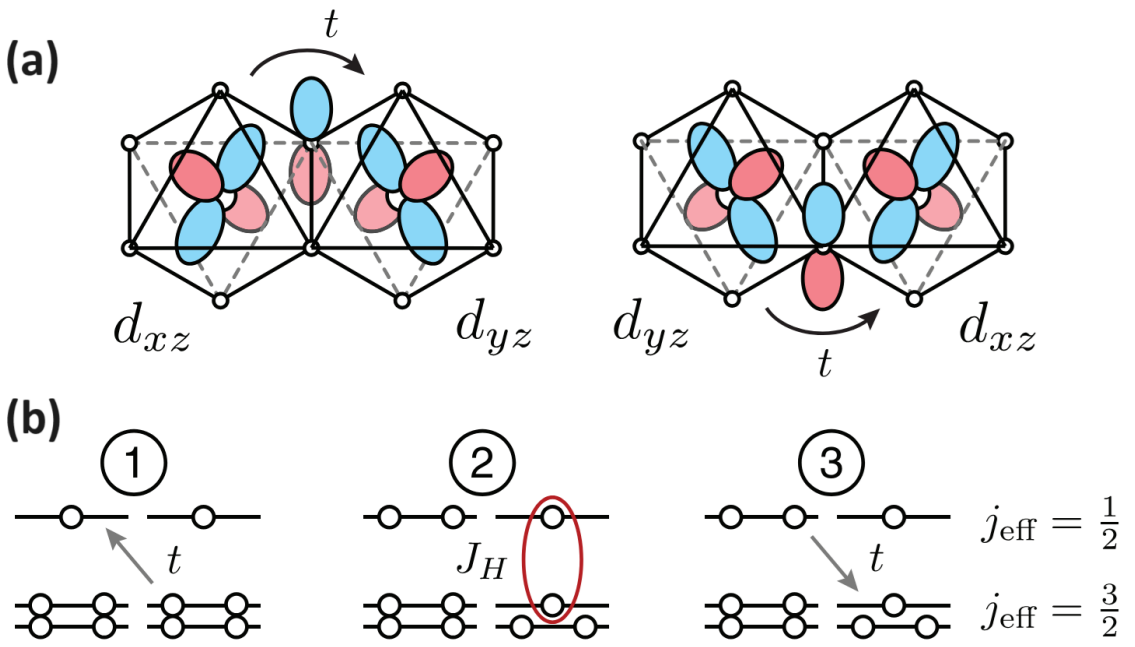

Figure 3.2: Model of bond-directional Kitaev interactions. Adapted from [16]. **(a)** Hopping paths considered in the idealized edge-sharing model by Jackeli and Khaliullin. **(b)** Schematic of virtual processes that lead to bond-directional Kitaev interaction.

Specifically, we consider 90° TM-O-TM bonds of edge-sharing octahedra (depicted in Fig. 3.2) that are found in systems with honeycomb-like structures such as Na_2IrO_3, Li_2IrO_3, and α-$RuCl_3$. If we consider the large Hubbard U limit, we can describe the low-energy spin Hamiltonian to be well-described by Eqn. 3.5. Jackeli and Khaliullin considered the case where exchange between neighboring d-orbitals is mediated by the intervening ligand p-orbitals. In the edge-sharing geometry, the

coupling is then given by the two hopping pathways depicted in Fig. 3.2(a). In this case, the hopping pathways destructively interfere so that, to leading order, the isotropic Heisenberg term $J \sim t^2/U$ exactly vanishes. We are left with a finite anisotropic interaction that arises due to the virtual process depicted in Fig. 3.2(b) and the presence of Hund's coupling [16]. This leads to a ferromagnetic interaction in the ground state $\sim t^2 J_H/U$. Importantly, this exchange interaction depends on the spatial orientation of the given Ir-Ir bond, taking the form:

$$H_{ij}^{\gamma} = -JS_i^{\gamma}S_j^{\gamma}, \tag{3.11}$$

where the principle axis labeled γ is perpendicular to the Ir-O_2-Ir plane of the bond. This is precisely the form of the Kitaev interaction [20]. Furthermore, edge-sharing octahedra form naturally form lattices with three nearest neighbors where the principle axes are orthogonal.

3.4 Material properties of β-Li_2IrO_3

3.4.1 Crystal structure

The results in Chapter 4 measure a high-quality single crystal sample of β-Li_2IrO_3 synthesized using a vapor transport technique. The crystals were synthesized using a vapor transport technique. They have an orthorhombic structure, belong to the *Fddd* (#70) space group, have dimensions of roughly $100 \times 150 \times 300$ μm^3, and have lattice parameters are $a = 5.8896(16)$Å, $b = 8.4314(17)$Å, and $c = 17.777(4)$Å at $T = 273$ K. The growth, crystal structure, and thermodynamic properties are extensively discussed in [21]. An image of a sample similar to the one used in Chapter 4 is shown in Fig. 3.3 [22].

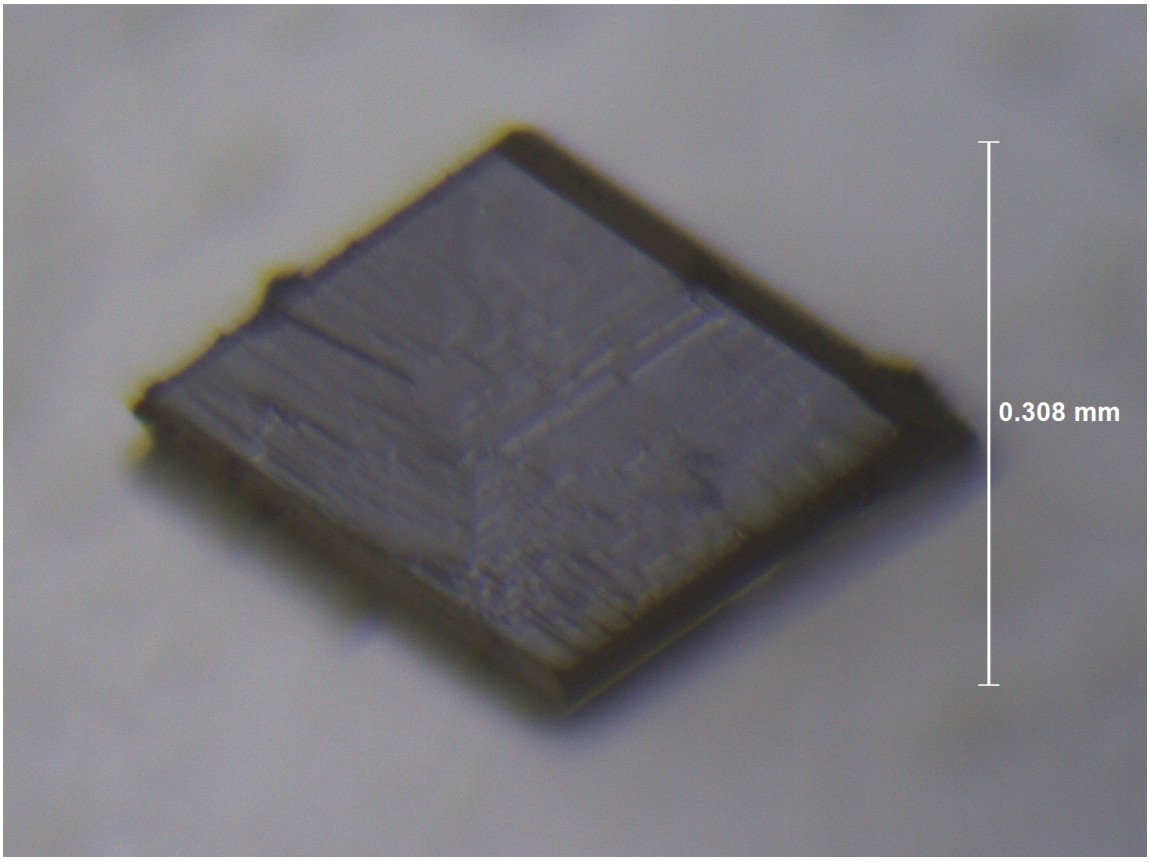

Figure 3.3: Image of β-Li_2IrO_3 single crystal from [22]

β-Li_2IrO_3 is a member of the harmonic honeycomb family of Li_2IrO_3 first described in Ref [23] and depicted in Fig. 3.4. The basic building blocks are IrO_6 octahedra, where each IrO_6 octahedron shares an edge with three neighboring IrO_6 octahedra. There are three orthogonal directions of spin exchange between Ir moments defined by the Ir-O_2-Ir planes highlighted in Fig. 3.4(a). This edge-sharing geometry gives rise to the bond directional interactions as described above.

The edge-sharing bond geometry with three neighbors leads to a honeycomb-like structure, where zigzag chains along the $\hat{a} \pm \hat{b}$ directions are stacked along the c-axis, where $\hat{a}$ and $\hat{b}$ are unit vectors along the a- and b-axes, respectively. Fig. 3.2(b)

shows the two distinct types of c-axis bonds, where one type links two parallel zigzag chains and the other rotates one zigzag chain with respect to the other by $\phi \sim 70°$. These ingredients can be combined to generate the harmonic honeycomb family $\langle N \rangle$-Li_2IrO_3.This thesis focuses on β-Li_2IrO_3, which is the $N = 0$ polytype where each zigzag chain is rotated with respect to its neighbors along the c-axis.

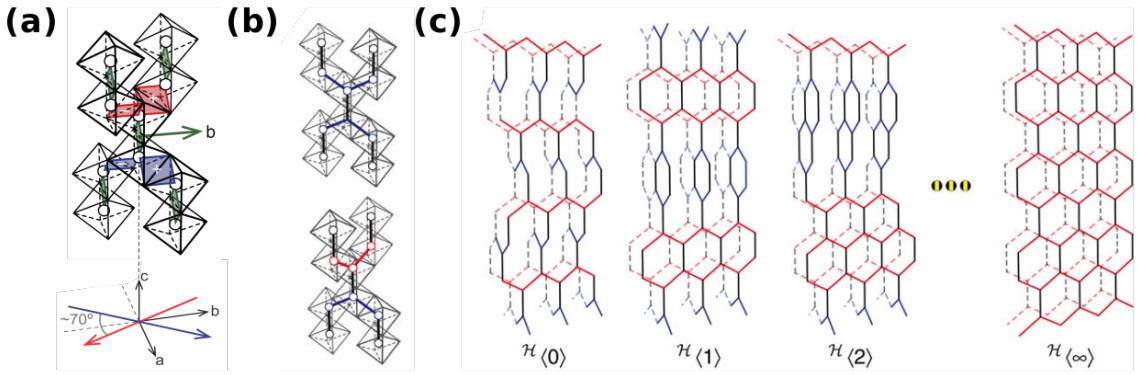

Figure 3.4: Harmonic honeycomb family $\langle N \rangle$-Li_2IrO_3. Adapted from [23]. **(a)** The building blocks of the harmonic honeycomb structure. There are two types of c-axis bonds (black bonds) that can link adjacent zigzag chains, resulting in two distinct honeycomb planes (blue and red) defined by the c-axis and the the $\hat{a}+\hat{b}$ direction or the c-axis and the $\hat{a}-\hat{b}$. $\hat{a}$ and $\hat{b}$ are unit vectors along the a- and b-axes, respectively. The top bond-type links within a single honeycomb plane (blue-to-blue or red-to-red) without rotation. The bottom bond-type rotates from one honeycomb plane to the other (blue-to-red or red-to-blue). **(b)** Series of harmonic honeycomb structures. Each structure is labeled as $\langle N \langle$-Li_2IrO_3, where N counts the number of completed honeycomb rows before a rotation. In literature, structures are usually labeled with a Greek letter described in Table 3.2.

Table 3.2: Harmonic honeycomb series of Li_2IrO_3 defined by [23]. See **??** for description of series.

Harmonic honeycomb number	Material	Lattice name	Dimensionality
$N = 0$	β-Li_2IrO_3	Hyper-honeycomb	3D
$N = 1$	γ-Li_2IrO_3	Stripy-honeycomb	3D
$N = \infty$	α-Li_2IrO_3	Layered honeycomb	2D

3.4.2 Magnetic structure

Low-temperature magnetic structure

The low-temperature magnetic order of β-Li_2IrO_3 at zero-field, shown in Fig. 3.5, was originally deduced by Ref. [24] using magnetic neutron powder diffraction. Below $T_N = 38$ K, the system takes on a spiral order with counter-rotating moments which is incommensurate with the lattice and propagates along the a-axis with a propagation vector of $\vec{q} = (0.571, 0, 0)$. We will refer to this phase as the incommensurate (INC) phase. Notably, γ-Li_2IrO_3 takes on a very similar order around the same temperature as well [25]. Reports using resonant elastic X-ray scattering [22] showed that, upon applying a magnetic field along the b-axis at low temperatures, the INC phase smoothly disappears, going to zero at $H_c \sim 2.8$ T. The system simultaneously develops a zigzag order (referred to as the field-induced zigzag, or FIZZ, order) which coexists with the INC phase. In the case of the FIZZ order, the moments propagate along the $\hat{a} \pm \hat{b}$ directions commensurate with the lattice. Interestingly, the intensities of the Bragg peaks associated with the INC and FIZZ orders can be rescaled to have a constant sum as shown in Fig. 3.6.

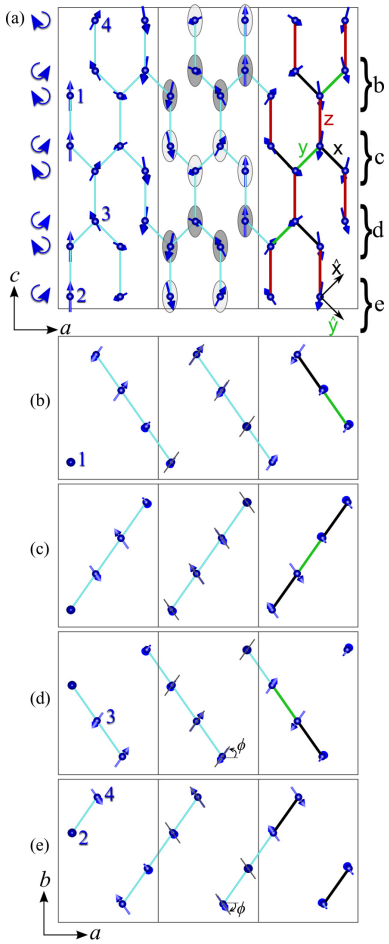

Figure 3.5: Real-space representation of magnetic structure of β-Li_2IrO_3 in INC phase. Adapted from [24]. **(a)** Projection of magnetic structure onto the ac plane. Blue spheres represent Ir atoms with the blue arrow representing its magnetic moment. Numbers 1-4 label sites of the primitive cell. The magnetic moments rotate are counter-rotating with every nearest-neighbor. This implies that along a zigzag chain, for example, every next-nearest-neighbor is rotated by a constant angle forming a spiral with a given handedness, whereas the remaining moments form a spiral with the opposite handedness. Furthermore, the magnetic moments rotate within two distinct planes, where the plane of rotation is the same along a given zigzag chain and alternates along the c-axis. These two planes are defined by tilting the ac plane about the c-axis by $\phi = \pm 55(1)^\circ$ and are depicted in the middle panel as light

Figure 3.5: and dark shaded ellipses. **(b)-(e)** Neighboring zigzag chains projected onto the *ab* plane corresponding to the labels b-e to the right of **(a)**. This illustrates the two planes of rotation.

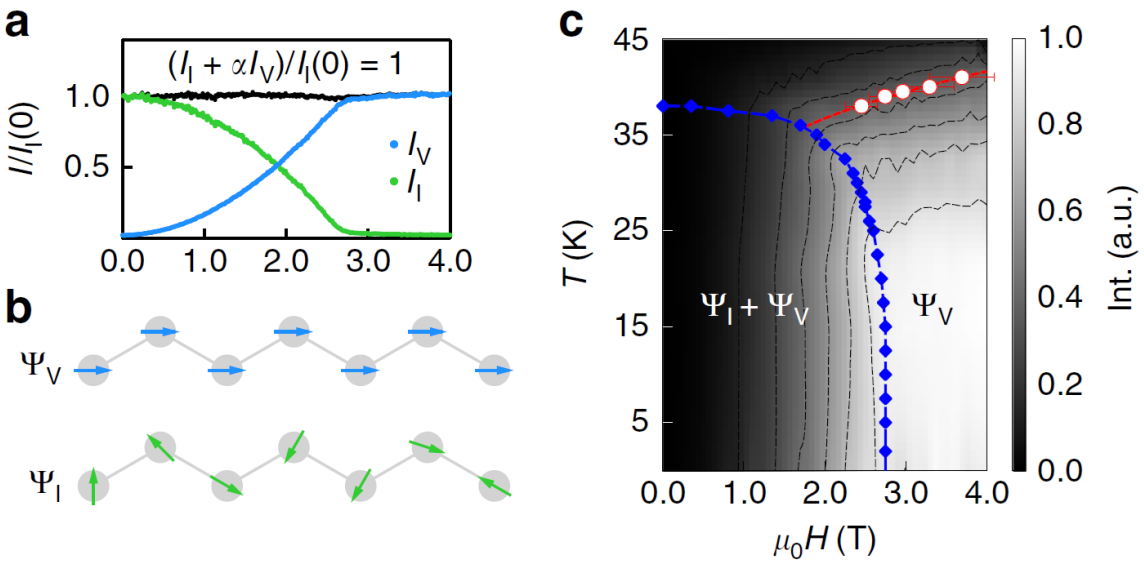

Figure 3.6: Low-temperature magnetic order parameter of β-Li_2IrO_3 with magnetic field applied along b-axis. Adapted from [22]. **(a)** Magnetic-field dependence of Bragg peak intensities of the INC phase (I_I) and the FIZZ phase (I_V) measured by resonant elastic X-ray (REXS). Intensities are rescaled and normalized such that $(I_I+\alpha I_V)/I_I(B=0) = 1$. This demonstrates the order parameter sum rule described in the text. **(b)** Schematic representation of the ordering of magnetic moments along zigzag chains for the INC Ψ_I and FIZZ Ψ_V orders. **(c)** T-H phase diagram superimposed with normalized REXS intensity of a peak commensurate with the lattice. The blue diamonds indicating the INC phase boundary was determined through a combination of magnetization and heat capacity measurements. The red dots indicating the FIZZ crossover boundary was determined through a cusp observed in magnetic field-dependent heat capacity measurements.

3.4.3 Dynamical characterizations

Thermodynamics

The low-temperature thermodynamic properties of β-Li_2IrO_3 are shown in Fig. 3.7, adapted from [21].

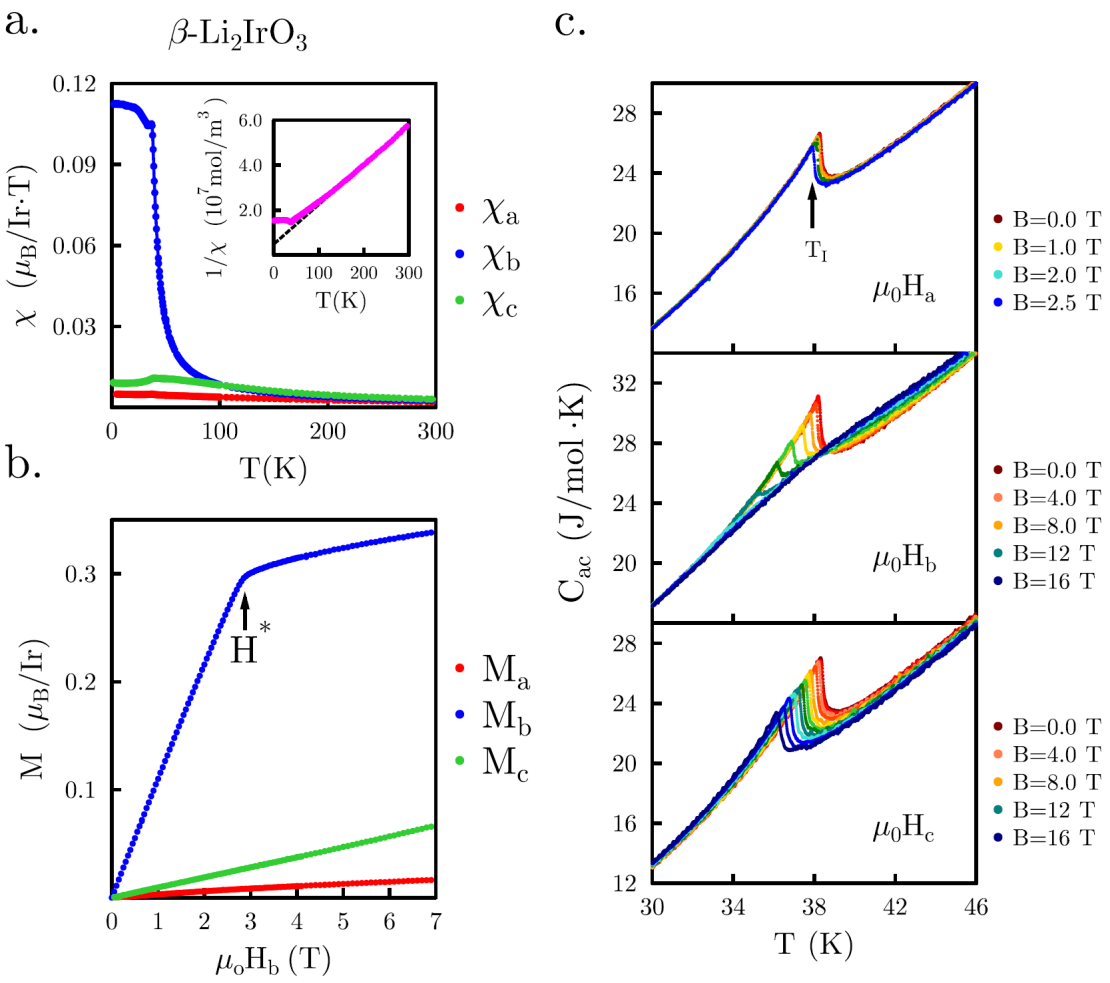

Figure 3.7: Low-temperature thermodynamic characterization of β-Li_2IrO_3. Adapted from [21]. **(a)** Temperature depndent magnetic susceptibility along different crystal axes with an applied magnetic field of 1 T. **(b)** Magnetic-field dependent magnetization along different crystal axes taken at $T = 2$ K. H^* indicates the critical magnetic field along the b-axis required to quench the INC order. **(b)** Temperature-dependent *ac* heat capacity with magnetic fields applied along different crystal axes. T_I indicates the INC phase transition.

Beyond the properties of the magnetic ordering at low-temperature, there are features in the dynamic response of β-Li_2IrO_3 at higher temperatures that depend on the magnetic field despite a lack of observable magnetic ordering. Namely, several results demonstrate a kink-like feature at $T_\eta \sim 100$ K [23, 21, 26]. It has been established that the data is consistent with a reordering of the magnetic principle axes at ~ 100 K for β- and γ-Li_2IrO_3, where the inverse magnetic susceptibility shows Curie-Weiss behavior above T_η and strongly deviates below T_η [23, 21, 26]. This deviation from conventional Curie-Weiss behavior indicates that the intermediate temperature regime $T_N < T < T_\eta$ demonstrates a magnetically disordered phase distinct from a conventional paramagnet.

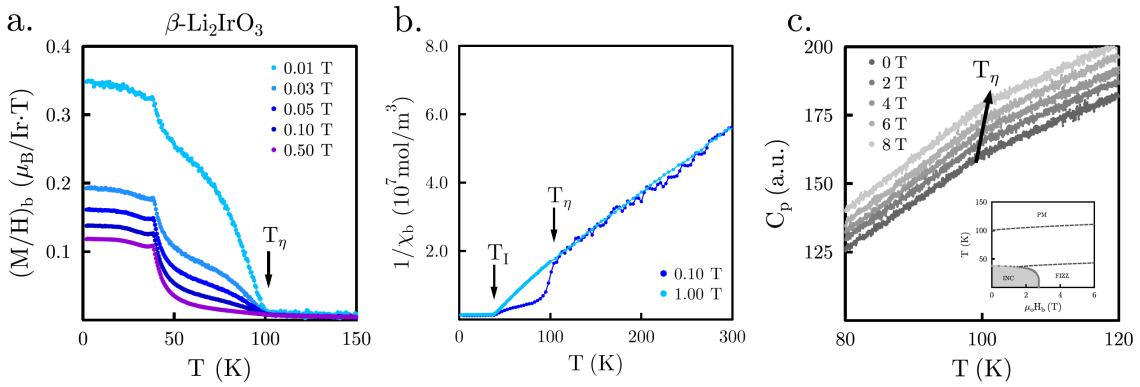

Figure 3.8: High-temperature thermodynamic characterization of β-Li_2IrO_3. Adapted from [21]. **(a)** Magnetic susceptibility of β-Li_2IrO_3 for a magnetic field applied along b-axis. **(b)** Inverse magnetic susceptibility for a magnetic field applied along the b-axis. **(c)** Temperature-dependent *ac* heat capacity near T_η for various applied magnetic fields. Arrow guides the eye highlighting the kink defining T_η. Inset shows T-H phase diagram.

Low-energy magnetic excitations

[27] suggests there are gapless magnetic excitations in the magnetically ordered incommensurate phase and gapped magnon-like excitations in the FIZZ phase. [28] suggests the same results through RIXS, but adds that there is a momentum-independent continuum of excitations at $\sim$ 35 meV. A continuum with a similar energy scale was reported by [29], measured through Raman scattering.

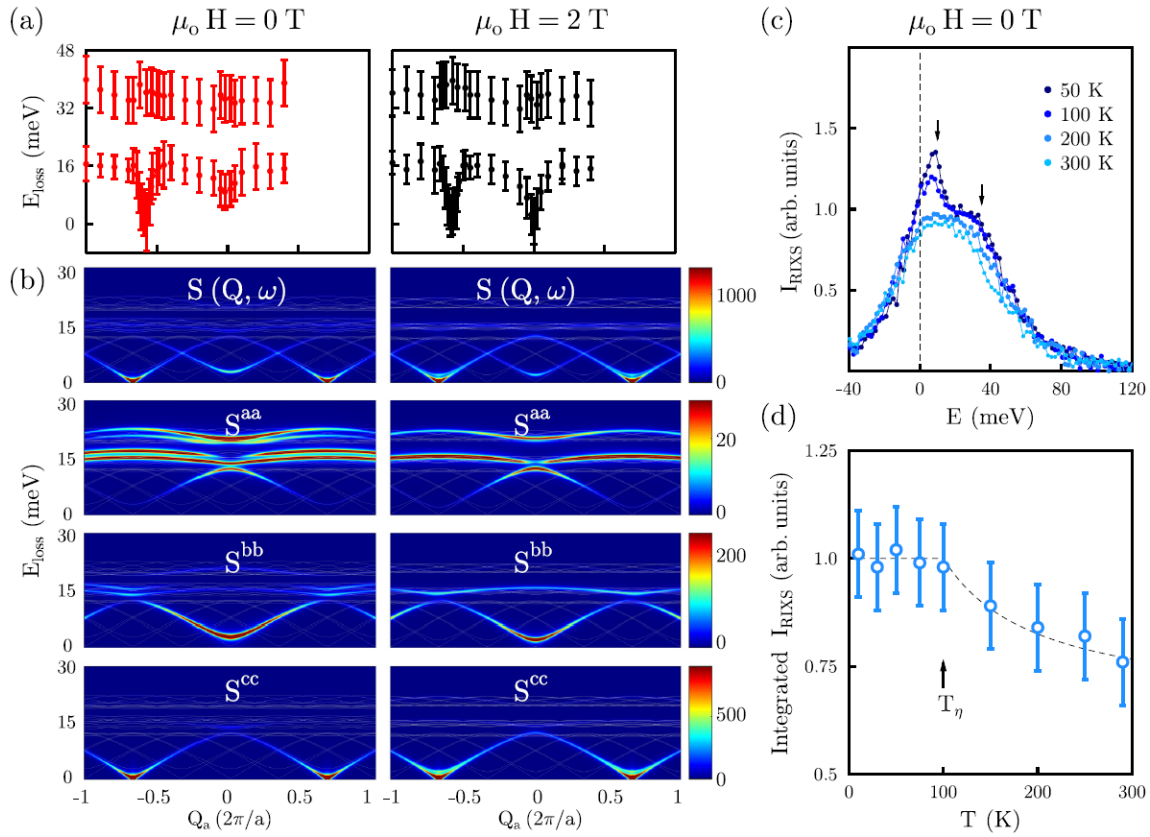

Figure 3.9: Low-energy resonant inelastic X-ray scattering (RIXS) and calculated dynamical spin structure factor of β-Li_2IrO_3. Adapted from [28]. **(a)** Dispersion of excitations from momentum-resolved RIXS. Circles and vertical bars indicate the peak and spread of excitations identified from RIXS spectra taken along (h, 0, 22) at $T = 5$ K. **(b)** Diagonal components of calculated dynamical spin structure factor, $S^{aa}(Q,\omega)$, $S^{bb}(Q,\omega)$, $S^{cc}(Q,\omega)$, and their sum, $S(Q,\omega)$. **(c)** Momentum-integrated RIXS spectra at various temperatures above T_N. **(d)** RIXS intensity integrated along momentum and along energy for $\hbar\omega > 20$ meV. Demonstrates the temperature dependence of continuum centered at ~ 35 meV described in paper.

Optical characterization

Optical conductivity has not been measured on β-Li_2IrO_3, but the primary features of are likely the same, both qualitatively and quantitatively, for α-, $\beta-$ and γ-β-Li_2IrO_3. The optical properties are shown in Fig. 3.10. The pump and probe energies used in Chapter 4 are 1.2 eV and 1.55 eV, respectively. These wavelengths overlap with features that are dominated by intersite $j_{eff} = 3/2$ to $j_{eff} = 1/2$ transitions, with some contributions from intersite $j_{eff} = 1/2$ to $j_{eff} = 1/2$ transitions. A theoretical analysis of the electronic transitions contributing to the optical properties of Na_2IrO_3, α-Li_2IrO_3, and γ-Li_2IrO_3 are explored in [30, 31].

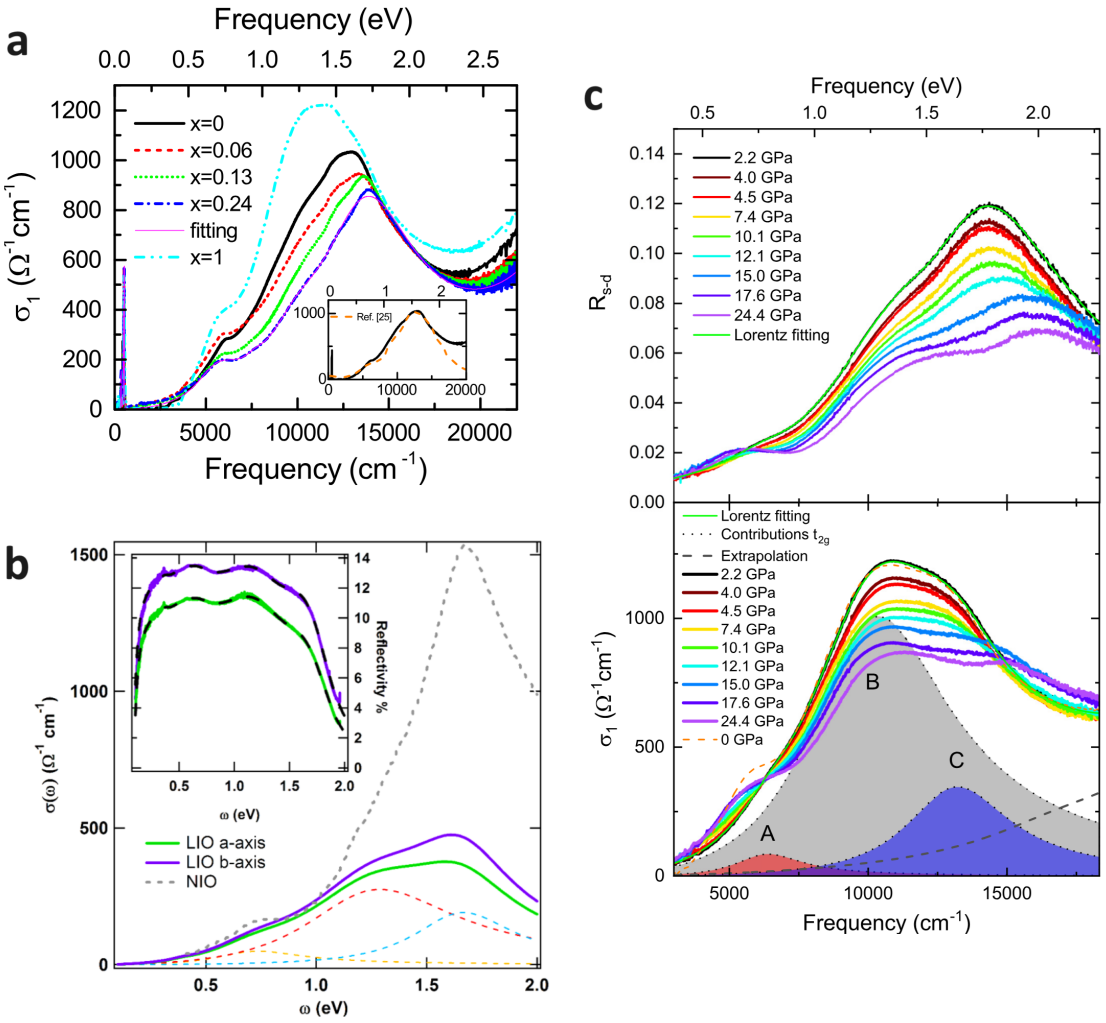

Figure 3.10: Optical conductivity for A_2IrO_3 (A=Na, Ir). **(a)** Adapted from Ref. [32]. Optical conductivity of $(Na_{1-x}Li_x)_2IrO_3$. Note that $x = 1$ corresponds to Li_2IrO_3. **(b)** Adapted from [33]. Optical conductivity and reflectivity of Na_2IrO_3 and α-Li_2IrO_3. Dashed colored lines show fits of reflectivity data in inset to Lorentz oscillators **(c)** Adapted from [32]. Reflectivity spectrum (top) and optical conductivity (bottom) for α-Li_2IrO_3 under the labeled pressures. Shaded regions labeled A, B, and C are fits of the 2.2 GPa reflectivity data to Lorentz oscillators. Descriptions of A, B, and C are given in the reference above.

Chapter 4

Tracking magnetism through photoinduced quasiparticle dynamics of $\beta - Li_2IrO_3$

4.1 Introduction

The quantum spin liquid (QSL) is a phase of matter central to the problem of strongly correlated and quantum many-body systems. The QSL phase is characterized by an absence of long-range magnetic order, a ground state with massive many-body and long-range entanglement, and fractionalized excitations [34]. QSLs have seen an explosion of interest in recent decades following Alexei Kitaev's formulation of an exactly solvable spin liquid ground state in the 2D honeycomb model [20]. This was followed by the formulation of an exact solution to the 3D honeycomb model [35] and the demonstration that the Kitaev honeycomb model can be materially realized in tri-coordinated 4 d and 5 d transition metal compounds with spin-1/2 pseudospins [12]. Experimental work subsequently flourished, with material candidates including $\alpha - \mathrm{RuCl_3}$, $\mathrm{A_2\,IrO_3}$(A = Li or Na), and a growing list of other

compounds [36].

Despite the concerted effort towards understanding QSLs, there are still several prominent roadblocks to a material realization and verification of a quantum spin liquid phase. First, the known candidate materials tend to exhibit magnetic order at low temperatures due to the presence of other parasitic magnetic exchange interactions [37], stabilizing long-range order and obscuring the QSL ground state. Second, proving the existence of a true QSL phase requires the measurement of long-range entanglement and fractionalized excitations - properties that are notoriously difficult to experimentally quantify. Given these issues, it is imperative to employ new techniques to overcome these barriers.

To that end, we study the QSL candidate $\beta - Li_2IrO_3$ using time-resolved spectroscopic techniques to gain new insights on the dynamical magnetic properties of $\beta - Li_2IrO_3$ and characterize possible signatures of spin correlations that may be useful for the tuning and identification of a true QSL phase.

$\beta - Li_2IrO_3$ is an attractive candidate to study spin liquid physics as its microscopic parameters place the material in close proximity to the spin liquid phase and its rich magnetic phases are experimentally accessible [38]. At ambient pressure, the low-energy electronic structure of β - Li_2IrO_3 is best described as a spin-orbit coupled Mott-Hubbard insulator with $j_{\text{eff}} = 1/2$ pseudospins on each tri-coordinated Ir^{4+} site in the ground state [39, 40], shown schematically in Fig. 4.1(b). The dominant magnetic interaction between pseudospins is a bond-directional exchange arising from inter-orbital hopping mediated by the oxygen ions, exactly analogous to the bond-directional interactions of the Kitaev honeycomb model [12].

Though the Kitaev exchange interaction has been shown to be the dominant energy scale at low temperatures [38], the isotropic Heisenberg and off-diagonal exchange interactions cause $\beta - Li_2IrO_3$ to magnetically order at low temperatures. As shown in the phase diagram in Fig. 4.1(c), at zero applied magnetic field, β - Li_2IrO_3 orders into a non-coplanar incommensurate (INC) order with counter-rotating mo-

ments along the magnetic propagation vector $Q = (0.574, 0, 0)$ below $T_N = 38$ K [24, 25, 41]. Upon applying a magnetic field along the b-axis, the INC order is suppressed at relatively modest magnetic fields, where a uniform $Q = 0$ collinear magnetic order develops in its place. This collinear magnetic order, henceforth referred to as field-induced zigzag order (FIZZ), has ferromagnetic alignment along the b-axis, admixed with a zig-zag canting along the a-axis [38, 42, 43, 22, 44]. As seen in the phase diagram in Fig. 4.1(c), the INC order is completely suppressed at a critical field $H^* = 2.8T$ at $T = 2$ K, while the FIZZ order remains stable until much larger fields [22, 28, 45]. In the intermediate region $H < H^*$, the INC and FIZZ magnetic orders coexist such that each broken symmetry state retains its intrinsic periodicity and the two order parameters obey a simple intensity sum rule described in [38, 22].

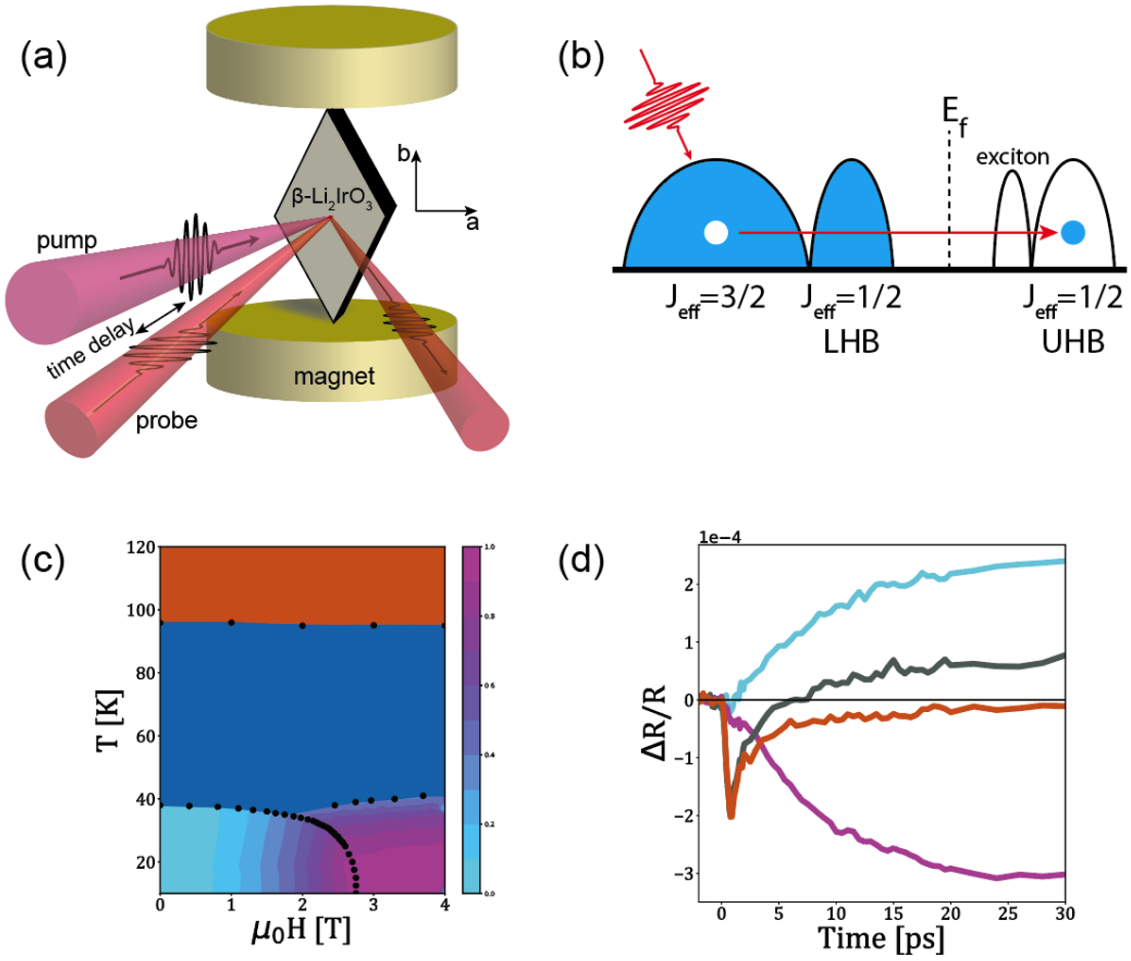

Figure 4.1: Overview of time-resolved reflectivity measurement and data on $\beta - Li_2IrO_3$. (a) Experimental setup. Single crystal $\beta - Li_2IrO_3$ is placed in a magnetic cryostat with the magnetic field oriented along the b-axis and the c-axis normal to the surface. The pump and probe are near normal incidence to the sample, and the polarizations are oriented along the b-axis and a-axis, respectively. (b) Schematic of the initial photoexcitation process and electronic structure. Electron in the $j_{eff} = 3/2$ valence band is photoexcited into the $j_{eff} = 1/2$ Upper Hubbard Band (UHB). (c) Equilibrium B-T phase diagram of $\beta - Li_2IrO_3$. The contour plot shows the normalized scattering intensity of a magnetic peak corresponding to the FIZZ order [22]. The INC and

Figure 4.1: FIZZ phase boundaries were determined using a combination of magnetization and heat capacity measurements [22]. The blue region shows the paramagnetic phase where the Kitaev interaction remains dominant (KPM), and the orange region shows the paramagnetic phase where the Heisenberg interaction becomes dominant (PM), persisting up to room temperature. The boundary is determined using ac-heat capacity measurements as described in [21]. (d) Overview of time-resolved reflectivity data in each magnetic phase. Colors correspond to color scheme from (c).

Furthermore, the temperature evolution of the susceptibility suggests a reordering of the principle magnetic axes at 100 K [23], coinciding with anomalous behavior observed in the magnetization, heat capacity, and muon spin relaxation [45, 21, 45]. The principle axes at high temperatures are determined by the structural anisotropy of the crystal, whereas below 100K, the principle axes seem to follow the Kitaev-like spin-anisotropic exchange. Though the origin is still unclear, the anomaly onsets at the characteristic energy scale of the Kitaev interaction and could be related to the broad continuum of excitations observed in Raman [29, 46] and Resonant Inelastic X-ray Scattering (RIXS) [28, 47, 48] experiments. Amazingly, these rich experimentally observed magnetic properties can be well-explained and quantified by the $J-K-\Gamma$ model, with the parameters placing the material in close proximity to the Kitaev spin liquid phase [38, 49].

Beyond its rich equilibrium magnetic order, β - Li_2IrO_3 exhibits a broad continuum in its low-energy excitation spectra, a feature which would be consistent with the emergence of fractionalized Majorana excitations. A broad continuum of excitations has been observed using several techniques including Raman spectroscopy [29, 46], resonant inelastic X-ray scattering (RIXS) [28, 47, 48], inelastic neutron scattering (INS), and THz spectroscopy [49]. Furthermore, this feature persists at intermediate temperatures $T_N < T < T_\eta$ where the system is magnetically disordered and the Kitaev interaction is the dominant energy scale. Despite these findings, the

microscopic nature of these excitations is yet to be understood. Thus, we turn to ultrafast techniques to directly probe the low-energy magnetic dynamics in the time domain.

Time-resolved reflectivity (TRR) has proven useful in the study of many different types of quantum materials, including superconducting cuprates [50, 51, 52], Fe-based superconductors [53], BCS superconductors [54], charge and spin density wave compounds [55, 56], f-electron compounds with heavy fermions [57], strongly spin-orbit coupled systems such as iridates [58], and ruthenates [59]. The versatility of this technique arises from its ability to detect changes in meV-scale electronic properties in quantum materials by means of photoinduced changes in the optical joint density of states at the probe photon energy with high sensitivity.

In this work, we measure the time-resolved reflectivity while tuning temperature, magnetic field, and photoexcitation density and show that the amplitude of the transient reflectivity is a linear combination of signals proportional to the magnetic order parameters of the low-temperature phases of $\beta - Li_2IrO_3$. We use nearly degenerate pump and probe wavelengths to selectively photoexcite electrons from the $j_{\text{eff}} = 3/2$ valence band to the $j_{\text{eff}} = 1/2$ upper Hubbard band and probe the same transition, as shown in Fig. 4.1(b). The resulting photoexcited quasiparticles interact with the magnetic background, inducing low energy magnetic dynamics.

4.2 Methods

High-quality single crystals of the 3D hyperhoneycomb iridate $\beta - Li_2IrO_3$ were grown using a vapor transport technique. The growth and thermodynamic properties are extensively discussed in [21]. The samples were mounted in a $7T$ optical cryostat (Opticool by Quantum Design) for T and B dependent time-resolved reflectivity (TRR) measurements. The TRR measurements were taken using a commercial Yb-based fiber laser (Spectra-Physics, Spirit) producing 350 fs pulses with wavelengths

centered at $\lambda = 1040$ nm and a 200kHz repetition rate. These pulses are used as a pump for the TRR measurements. A non-colinear optical parametric amplifier (NOPA) was used to generate linearly polarized 25 fs probe pulses with wavelengths centered at $\lambda = 800$ nm. For additional details on the laser system and detection electronics, see [57]. The pump and probe beams were focused to $1/e^2$ spot diameters of 60 μm and 30μm respectively and a dielectric short-pass optical filter was used to block scattered pump photons from hitting the photodetector. The data were collected from an as-grown a - b crystal face, with dimensions of approximately 70μm along the a-axis and 130μm along the b-axis. Unless explicitly stated, the data are reported with the pump polarized along the b-axis and the probe polarized along the a-axis.

Our measurements are performed in the gentle photoexcitation regime, using a pump fluence of $F = 5\mu\text{J/cm}^2$ for all measurements unless otherwise stated. We estimate the optical penetration depth to be 120 nm for the pump beam and 90 nm for the probe beam using published optical data on $\gamma - \text{Li}_2\text{2IrO}_3$ [36]. At $\text{F} = 5\mu\text{J/cm}^2$, we estimate one absorbed pump photon per 10^{-4}Ir sites. Based on published heat capacity data [21], we can roughly estimate an upper bound on the increase in temperature due each pump pulse at $\text{F} = 5\mu\text{J/cm}^2$, described in detail in Supplemental IV.

4.3 Results

We first characterize the photoexcitation and TRR response in the absence of magnetic order by measuring the sample at temperatures well above T_η. The red curve in Fig. 4.1(d) shows the change in reflectivity at $T = 150$ K where the sample is fully paramagnetic and still maintains its $j_{\text{eff}} = 1/2$ Mott-Hubbard electronic structure. The signal consists of a fast negative change in reflectivity from the impulsive photoexcitation, followed by a multi-exponential decay. We observe that the

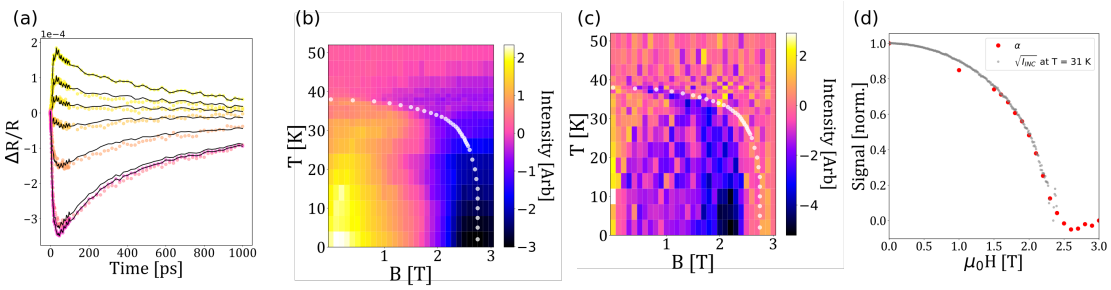

Figure 4.2: Field dependence of time-resolved reflectivity signal. (a) time-resolved reflectivity signal at various B fields taken at 2K. Fits to Eqn. 4.1 (solid line) are superimposed on data (colored circles). (b) Amplitude at peak of $\Delta R/R$ corresponding to a pump-probe delay of 33 ps (see dashed vertical line in (a)) plotted over B and T. White open circles show the incommensurate phase boundary, taken with permission from [22]. (c) Derivative data shown in (b) with respect to b. (d) Extracted parameter α^2 (blue circles) plotted over field and normalized intensity of order parameter from REXS (grey).

amplitude and timescales of these dynamics are only weakly temperature-dependent and independent of magnetic field, as expected from a paramagnetic Mott-Hubbard insulator far from the Mott transition. This is substantiated by seeing that all of the normalized TRR curves collapse onto each other at sufficiently high temperatures (See Supplemental 4.7.2).

Next, we turn to the magnetically ordered phases. As T is reduced below the ordering temperature T_N, we observe a new signal component emerge with a timescale of about 10ps that shows significant and distinct behavior in each of the magnetic phases, as shown in Fig. 4.1(d). Notably, the maximum amplitude of the signal is $\sim 100\times$ larger in the magnetically ordered phases than the signal in the high-temperature paramagnetic phase.

To quantify how this signal depends on the magnetic order, we show in Fig. 4.2(b) the amplitude of the TRR signal across the low-temperature phase diagram at a constant time of $t = 35$ps after photoexcitation, corresponding to the peak of the signal and denoted by the dashed line in Fig. 4.2(a). The derivative with respect to magnetic field of the same data is shown in Fig. 4.2(c). Immediately, the TRR amplitude qualitatively maps onto the equilibrium phase diagram. The open white circles superimposed onto the TRR data in Fig. 4.2(b),(c) show the phase boundary for the INC equilibrium phase determined by magnetization and heat capacity and obtained with permission from Ref [24]. This demonstrates that the TRR amplitude is sensitive to the INC magnetic order. This also indicates that the photoinduced heating is relatively small, as there is no significant temperature increase in the phase boundary for the TRR data. Furthermore, the amplitude of the TRR signal seen in Fig. 4.2(b) mimics the relative amplitudes of the INC and FIZZ order as measured by resonant elastic X-ray scattering, shown in Fig. 4.1(c). We quantify this correspondence by modeling the field dependence of the TRR signal, $\Delta R/R(B,t)$, as a linear weighted sum of the purely INC response, $\Delta R/R(0T,t)$, and the purely FIZZ response, $\Delta R/R(3T,t)$, at each temperature:

$$\frac{\Delta R}{R}(B,t) = \alpha \cdot \frac{\Delta R}{R}(0T,t) + (1-\alpha) \cdot \frac{\Delta R}{R}(3T,t) \tag{4.1}$$

where α, corresponding to the fraction of the signal due to the purely INC response, is the only free parameter. $(1-\alpha)$ corresponds to the fraction of the signal due to the purely FIZZ response. The fits to Eqn. 4.1 at each field are superimposed on the data in Fig. 4.2(a) and are remarkably accurate, demonstrating that the weighted sum faithfully reproduces the time-dependence of the dynamics at all fields. In particular, the fits reproduce the subtle time dependence of the nearly suppressed signal near $B = 1.7T$, which is due to small differences in the characteristic timescales of the dynamics associated with the INC and FIZZ orders. In Fig. 4.2(d), the extracted parameter, α, is plotted against the INC order parameter as measured by REXS at an elevated temperature of $T \approx 31K$. The integrated intensity of the magnetic Bragg peak measured by REXS is proportional to the square square of the magnetic order parameter, $I_{INC} \propto \psi_{INC}^2$. Therefore, the amplitude of the TRR signal is directly proportional to the spin structure factor of the INC ordering. We find that α is directly proportional to the order parameter of the INC phase, $\alpha \propto \psi_{INC}$. This result demonstrates that the reflectivity is directly related to the INC order parameter and thus serves as a quantitative reporter of magnetism in β-Li_2IrO_3. This correspondence of the optical reflectivity to the order parameter and to the REXS data strongly restricts any microscopic theory of the origin of the signal. We can further take advantage of the time-resolved nature of this technique, allowing us to extract the functional form of the dynamics, relevant timescales, and how these depend on external parameters including temperature, magnetic field, and fluence.

We fit the dynamics in full and show several fits to characteristic TRR signals in Supplementary Note 4.7.3. We simplify the parameter extraction by subtracting out the temperature- and field-independent high temperature response at 50 K from each data set. Though there are limitations to this method, this allows us to model the signal components directly related to magnetic dynamics. The subtracted data

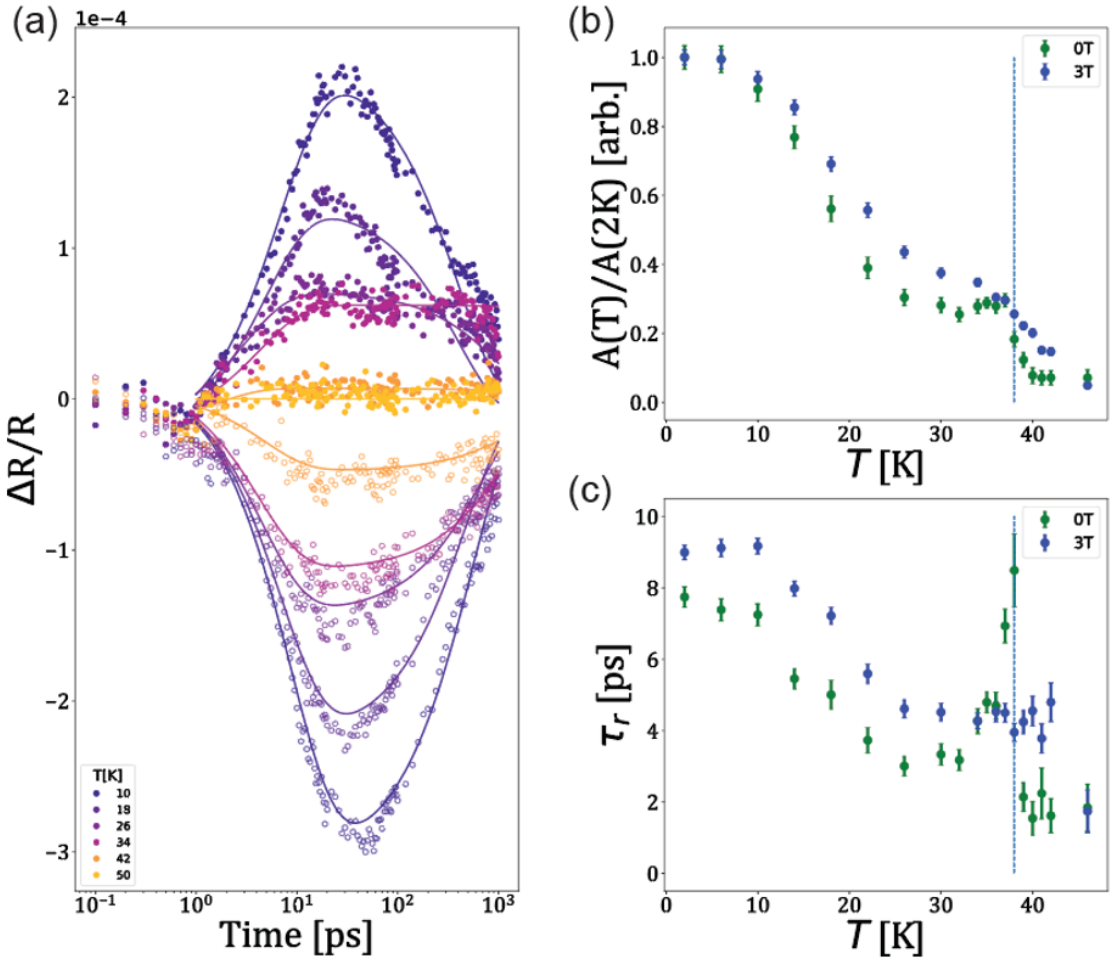

Figure 4.3: Time-domain analysis of low-temperature $\Delta R/R$ signal. (a) Time-resolved reflectivity signal across several temperatures at 0T (filled circles) and 3T (open circles). The fits are shown as solid lines. (b) Extracted fit parameters from Eqn. 4.2 as a function of temperature. The top shows the normalized amplitude $A(t)/A(T = 2K)$, and the bottom shows the rise-time, $\tau_r(t)$. Dashed line in both plots show critical temperature $T_N = 38$K.

can then be accurately fit to the simple functional form:

$$\frac{\Delta R}{R} = A \cdot \left(1 - e^{-t/\tau_r}\right) \cdot e^{-(t/\tau_{recovery})^{\beta}} \tag{4.2}$$

where A, τ_r, τ_1 and τ_2 are the amplitudes, rise time, and two relaxation times of the slow component as a function of temperature and magnetic field of the $\Delta R/R$ signal, respectively. Fits to Eqn. 4.2 are superimposed on the data for $B = 0T$ and $T = 2$ K in Fig. 4.3(a). Notably, a similar functional form and time scales are reported for the photoinduced dynamics of $Na_2\,Ir\,O_2$ [23, 29, 46], $\gamma - Li_2IrO_3$ [23], and α $RuCl_3$ [47], indicating that the photoexcited quasiparticles and their dynamics are governed by similar underlying physics. We fit Eqn. 4.2 to the TRR at $B = 0T$ and $B = 3T$ as a function of temperature to highlight how the signal evolves across the INC phase boundary and the FIZZ crossover, respectively. The resulting fit parameters are plotted in Fig. 4.3 where a kink is observed at $T \approx T_N$ denoted by the dashed line in Fig. 4.3(b),(c). Key similarities and differences can be seen in the temperature dependence of $A(T)$ and $\tau_r(T)$ for the $B = 0T$ (INC) and $B = 3T$ (FIZZ) dynamics. The temperature dependences of the fit parameters are nearly identical for $T \lesssim 30$ K in both the INC phase and the FIZZ phase, but there is a clear deviation as T approaches T_N. Particularly, there is an upturn in τ_r for $B = 0T$ that is not present for $B = 3T$. This upturn in the INC phase is related to critical fluctuations of INC order near the phase boundary as discussed in [18] for $\gamma - Li_2IrO_3$ and seen in thermodynamic measurements of $\beta - Li_2IrO_3$ [22]. The lack of critical behavior at $B = 3T$, on the other hand, is in agreement with the lack of critical behavior of the FIZZ order demonstrated by the broad crossover-like behavior seen in thermodynamic measurements [22]. We next discuss how these dynamics can shed light on a microscopic understanding of the underlying magnetism in $\beta - Li_2IrO_3$.

4.4 Discussion

Above, we pumped β - Li_2IrO_3 across the Mott-Hubbard gap and measured the subsequent dynamics using time-resolved reflectivity throughout the magnetic phase diagram and obtained quantitative relationships between the TRR signal and the magnetic order parameters. To summarize, (i) the amplitude of the $\Delta R/R$ signal reproduces the low-temperature B-T phase diagram, (ii) the $\Delta R/R$ amplitude has one-to-one correspondence with the INC magnetic order parameter measured by REXS in the form of Eqn. 4.1, and (iii) the time-domain dynamics can be fit to a relatively simple functional form (Eqn. 4.2), revealing a photoexcited population of quasiparticles whose dynamics demonstrate critical behavior across the INC phase boundary and crossover-like behavior across the FIZZ.

A natural question that arises is how a magnetic signal can appear in the reflectivity which only depends on the diagonal components of the complex dielectric tensor $\tilde{\epsilon}$. For systems where interband transitions dominate the optical properties, the imaginary part of the dielectric function is directly proportional to the joint density of states, $\epsilon_2(\omega) \propto J(\omega)$ (Eqn. 6.3.4 from [60]), where ϵ_1 is then causally related to ϵ_2 through the Kramers-Kronig relation. This implies that perturbations to the joint density of states cause a change in the dielectric function, $\delta\tilde{\epsilon}(t) = \frac{\partial\tilde{\epsilon}}{\partial J}\delta J(t)$, where such perturbations can be caused by photoexcitations as observed in our experiments. This directly relates the joint density of states to the change in reflectivity observed in our experiments,

$$\delta\tilde{r}(t) = \frac{\partial\tilde{r}}{\partial\tilde{\epsilon}}\frac{\partial\tilde{\epsilon}}{\partial J}\delta J(t)$$

where $\frac{\Delta R}{R}(t) = \left|\frac{\delta\tilde{r}}{\tilde{r}}(t)\right|^2$. We note that our pump and probe photons are resonant with the $j_{eff} = 3/2$ valence band to $j_{eff} = 1/2$ UHB interband transition, where each band is composed of strongly spin-orbit coupled electrons [30]. We posit that the large signal appearing in the INC and FIZZ ordered states originate from the

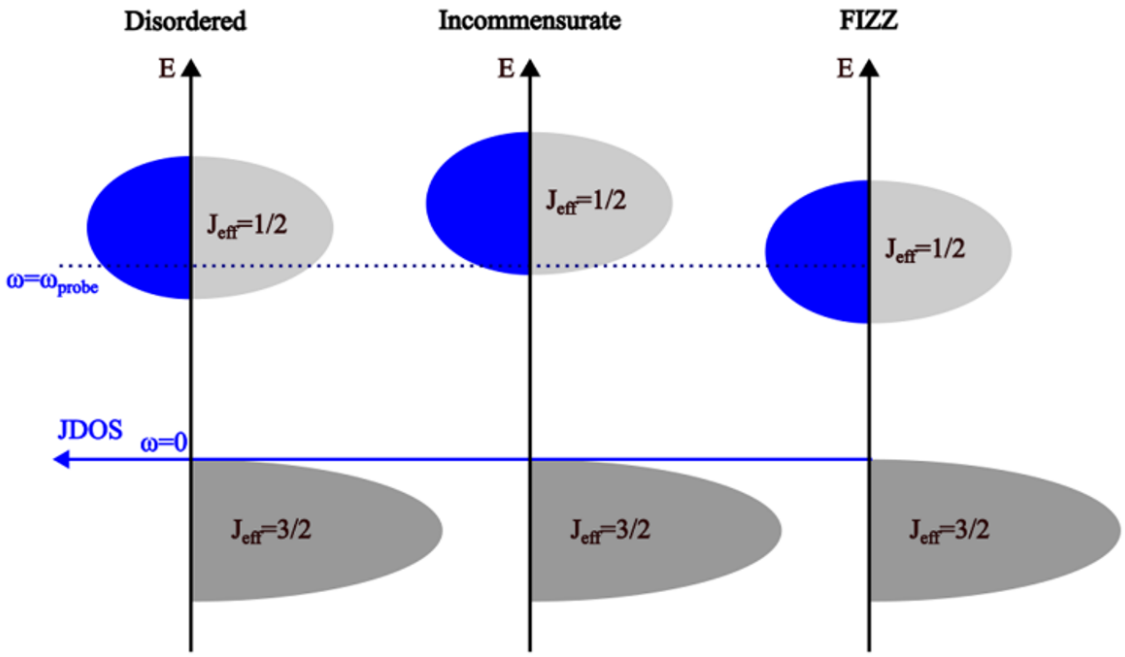

Figure 4.4: Schematic example of magnetic ordering altering the joint density of states. See main text for description. The dark grey shows filled states in the $j_{\text{eff}} = 3/2$ band, while the light grey shows unfilled states. The corresponding joint density of states is in blue. As the magnetic ordering changes the gap between the $j_{eff} = 3/2$ to $j_{eff} = 1/2$ bands, the joint density of states, and therefore the reflectivity, changes at the probe frequency, denoted by the dashed blue like labeled $\omega = \omega_{\text{probe}}$.

coupling of the magnetic degrees of freedom with the band structure.

A possible scenario is schematically shown in Fig. 4.4. In this example, the INC (FIZZ) order shifts the bands such that the joint density of states is lower (greater) at the probe frequency. After photoexcitation, the spin system is disordered, driving the system back towards the high-temperature band structure. This causes a photoinduced increase (decrease) in the joint density of states when starting in the ordered INC (FIZZ) phase, mapping onto an increase (decrease) in the transient reflectivity as observed in our experiment. Calculations modelling the effects of magnetic order on the optical response would help elucidate this matter.

Lastly, we turn to the high-temperature anomaly previously observed in [22, 21, 23, 26]. We observe the onset of a positive signal component that peaks at $T \approx 100$ K of the same form to the dynamics described by Eqn. 4.2. The behavior can clearly be seen by plotting the peak positive amplitude of the $\Delta R/R$ signal vs. temperature as shown in Fig. 4.4(b). The signal quickly grows in over a relatively short temperature window, and then subsequently decreases as temperature is further decreased. The inset shows the full-width at half-maximum (FWHM) of the transition vs. magnetic field, showing a linear broadening of the transition temperature with increasing applied magnetic field. We follow the same procedure described above to fit the signal in the time-domain according to Eqn. 4.2, where we subtract the high-$\Delta R/R(T = 150K, B)$ to isolate the slow rising component. We plot the amplitude and rise time as a function of temperature at various fields in Fig. 4.4(c),(d), showing a clear cusp at $T \approx 100$ K that has a linear field dependence.

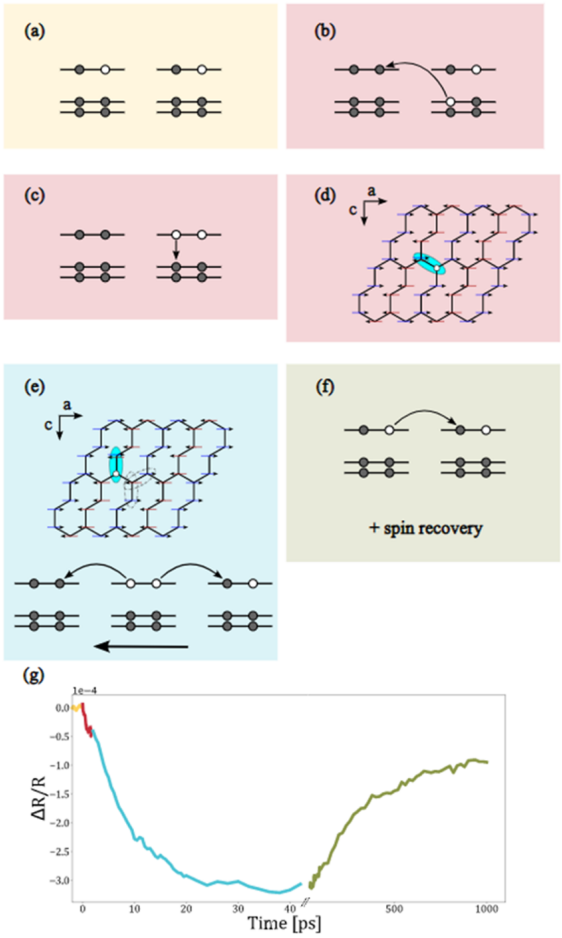

Figure 4.5: Schematic depicting microscopic model of dynamics. (a) Low-energy electronic states of two neighboring Ir^{4+} sites in equilibrium. Filled circles indicate occupied states, while empty circles represent unoccupied states. (b) Intersite single-electron excitation from a $j_{\text{eff}} = 3/2$ state to a $j_{\text{eff}} = 1/2$ state of a neighboring Ir^{4+} atom. This is the dominant photoexcitation pathway for our pump of $\hbar\omega = 1.2$eV [30]. (c) Intrasite transition of excited electrons from $j_{\text{eff}} = 1/2$ to $j_{\text{eff}} = 3/2$. This is a relatively fast relaxation step of the initial photoexcited state, where a doublon and a holon have been formed on the left and right neighboring Ir $^{4+}$ sites, respectively. (d) Real-space picture of the doublon-holon pair superimposed on the

Figure 4.5: β-Li_2IrO_3 lattice in the field-induced zig-zag state (FIZZ) projected onto the $a-c$ plane. The blue and red arrows indicating neighboring spin chains. In the presence of such a magnetic background, the doublon and holon are weakly bound as a Hubbard exciton, indicated by the blue oval. (e) An example of the Hubbard exciton hopping to a neighboring pair of sites. The ovals with dashed outlines indicate pairs of spins that have a different ordering than in the ground state, leading to an energy cost to the hopping process. The schematic below the lattice shows the two-step hopping process in the picture of the low-energy electronic states, depicting the electrons hopping to neighboring Ir^{4+} sites and causing a net motion to the left. (f) Recovery of excitation back to the ground state. (g) Representative $\Delta R/R(t)$ trace taken in the FIZZ state at $T = 2$K, B=3T and fluence F = 5μJ/cm^2. The colors correspond to the steps described in (a)-(f).

Given the similar time scale and functional form of this signal, the cusp about $T \approx 100$ K is likely related to the dynamics described for the low-temperature magnetically ordered phases. β - Li_2IrO_3 is known to have its magnetic principle axes reorder at 100 K[22, 21, 23, 26]. The reordering is attributed to the dominant energy scale changing from the isotropic Heisenberg exchange in the high-temperature regime ($T > 100$ K), to the anisotropic Kitaev-like exchange being dominant below 100 K [45, 21, 23]. This reorientation corresponds to a change in short-range spin correlations which may affect the dynamics probed by TRR. The cusp at $T \approx 100$ K indicates that te dynamics of the photoexcited quasiparticles are sensitive to these short-ranged correlations.

Next, we turn to contextualizing our observations with respect to reported results of time-resolved spectroscopic experiments in related compounds [61, 62, 63, 33, 64, 65, 66, 67]. It is notable that the time domain signals are qualitatively similar to those of Na_2IrO_3 [62, 62, 66, 67], $\gamma - Li_2IrO_3$ [33], and $\alpha - RuCl_3$ [64, 65]. Though these experiments were conducted under slightly different experimental con-

ditions, including laser fluence and wavelengths, the general ansatz of pumping and probing transitions across the Mott-Hubbard gap is common to all these results. The temporal dynamics in all of these compounds show functional forms similar to that of Eqn. 4.2 above, and with similar timescales on the order of 5-10ps as well. These similarities are highly suggestive of a common underlying picture describing the photoinduced dynamics across these candidate Kitaev magnets. However, despite these observations, a coherent story explaining these dynamics is yet to emerge, with various reports attributing the response to Hubbard excitons [62, 62, 64, 65], the delocalization of quasimolecular orbitals in an antiferromagnetic background [66], and fractional quasiparticles of the Kitaev model [67]. We extend these findings to $\beta-Li_2IrO_3$ where the unique magnetic phase diagram with competing INC and FIZZ orders gives new insights into a general understanding of pump-probe dynamics in Kitaev magnets.

A recent 2-photon photoemission spectroscopy result in $\alpha - RuCl_3$ [65] reported the ultrafast formation of Hubbard excitons on the timescale of $\sim 1ps$ after photoexcitation of doublon-holon pairs across the Mott-Hubbard gap, followed by a slow decay of these Hubbard excitons on the timescale of $\sim$ 500ps. Excitonic features have also been reported in $\beta - Li_2IrO_3$ via resonant X-ray scattering measurements [28]. Hubbard excitons are known to interact with the magnetic background where the binding energy of these excitons is proportional to the separation of doublon-holon pairs [61, 62]. The relationship of these Hubbard excitons to spin dynamics were elucidated using time-resolved magnetic linear dichroism [64], directly observed the transient disordering of the magnetic background in $\alpha - RuCl_3$ due to a photoexcited population of Hubbard excitons.

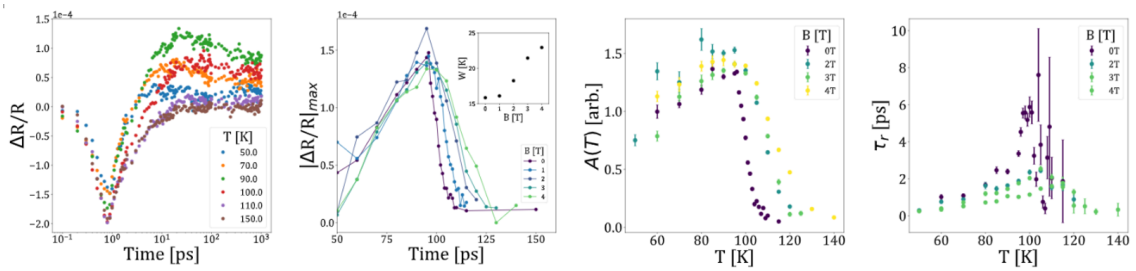

Figure 4.6: Time-domain analysis of high-temperature ΔR /R signal. (a) Time-resolved reflectivity signal across several temperatures at $B = 0$T. (b) Absolute amplitude of ΔR /R. Inset shows full temperature width at half-maximum of the transition as a function of applied magnetic field. (c) Extracted amplitude $A(t, B)$ from Eqn. 4.2 for high-temperature ΔR /R. There is a clear change in signal amplitude across ∼100K, where the onset is shifted by applied magnetic field. (d) Extracted rise time $\tau_r(T, B)$ from Eqn. 4.2 for high-temperature ΔR /R. Peak in rise time observed at 100K as well.

Thus, we can describe we can describe the photoinduced dynamics in β - Li_2IrO_3 observed through $\Delta R/R$ results reported above by the framework schematically shown in Fig. 4.5. (i) The 1.2eV pump excites electrons through the intersite $j_{eff} = 3/2$ valence band to $j_{eff} = 1/2$ UHB transition, creating a nonequilibrium population of electron-hole pairs within the timescale of the pump pulse ($\tau_{e-h} \approx 300$fs). (ii) The holes in the valence band are quickly filled by either photoexcited carries in the UHB or carriers in the LHB, leaving exactly equal numbers of doublons (double occupancy of electrons on a given Ir site) and holons (unoccupied Ir site). This leads to the exponential decay of the initial peak, most easily recognized in the high-temperature TRR signal. (iii) In the presence of magnetic correlations (where FIZZ order is depicted in Fig. 4.5), the doublons and holons interact and form Hubbard excitons. Due to selection rules, the Hubbard excitons are optically dark and are therefore not readily probed by the 800 nm probe beam. However,

as described above for similar spin-orbit coupled Mott-Hubbard insulator [65], the doublons and holons quickly bind to form a stable population of Hubbard excitons on the timescale of $\tau_{HE} < 1ps$. (iv) The population of Hubbard excitons dissipate excess energy through various decay channels, including spin fluctuations. For example, as a Hubbard exciton hops through the lattice, it creates local spin defects along its path. This spin disordering process is associated with the timescale $\tau_r \sim 10$ ps as seen in Eqn. 4.2 and corresponds to the kinetic model described in [33] on the dynamics of $\gamma - Li_2IrO_3$. This understanding is further supported time-resolved magnetic linear dichroism measurements on $\alpha - RuCl_3$ [64], where similar magnetic dynamics are reported. (v) Once the Hubbard excitons are at quasi-thermal equilibrium with the system, the Hubbard excitons recombine via multimagnon emission [63, 64] and other processes on a longer timescale. This timescale is known to be $\sim$ 500ps in $\alpha - RuCl_3$, and likely has a similar timescale in $\beta - Li_2\,IrO_3$[39, 36]. (vi) The magnetic order then recovers on the timescale of $\tau_{\text{spin}} \gtrsim 1$ ns.

4.5 Conclusion

In summary, we investigated the Kitaev spin liquid candidate $\beta - Li_2IrO_3$ across several magnetic phases using time-resolved reflectivity. We demonstrated that the initial $\Delta R/R$ dynamics occur on a characteristic timescale of 10ps that strongly varies with the equilibrium magnetic background. The amplitude of this magnetic signal tracks the order parameter of the low-temperature incommensurate phase, giving a direct handle on observing the photoinduced order parameter dynamics of this $\boldsymbol{q} \neq 0$ magnetically ordered state. We characterize the associated temperature and magnetic field dependences of this signal, revealing critical and crossover-like behavior across T_N at magnetic fields of $0T$ and $3T$, respectively, as observed static measurements. We then describe a possible mechanism for this magnetic signal to appear in reflectivity, as well as describe possible model for understanding the dynamics.

Finally, we demonstrated that the magnetic signal persists at intermediate temperatures $T_N < T < T_\eta$, where the Hubbard excitons may be interacting with a magnetic background with short range correlations. This work develops an understanding of the magnetic properties of other Kitaev spin liquid candidates from a timeresolved dynamical perspective and provides insights into the fundamental understanding of photoexcited Hubbard excitons in spin-orbit coupled iridates.

4.6 Acknowledgements

This chapter, in part, is currently being prepared for submission for publication of the material. Kim, Peter K.; Ruiz, Alejandro; Kissin, Peter; Poore, Maxwell; Vranas, Mayia; Analytis, James; Frañó, Alex; and Averitt, Richard D. The dissertation author was the primary investigator and author of this material.

Research at UCSD supported by the U.S. National Science Foundation DMR-1810310 and NASA 80NSSC19K1210.

4.7 Supplemental information

4.7.1 Supplementary Note 1: Comparing α to REXS intensity

As described in the main text, we fit the pump-probe time-resolved reflectivity (TRR) data to Eqn. 4.1. The resulting fits are shown in Fig. 4.1(a) in the time-domain, and the resulting fit parameters are plotted in Fig. 4.1(b). We compare the extracted parameter $\alpha(H)$ and compare it to the values for α obtained by resonant elastic X-ray scattering (REXS) at various temperatures.

We note that the magnetic field dependence of the extracted α from $\Delta R/R$ at $T = 2$ K follows the magnetic field dependence of the REXS intensity at $T = 31$ K.

This implies that the parameter extracted from the pump-probe TRR measurements is proportional to the REXS intensity at a heightened transient temperature.

4.7.2 Supplementary Note 2: Temperature dependence of fast signal component

In order to isolate the component of the $\Delta R/R$ signal due to the magnetic ordering, we subtracted a representative $\Delta R/R$ scan above the ordering temperature from each low-temperature $\Delta R/R$ scan. We chose $T = 50$ K as this temperature was above the critical temperature for the incommensurate order at $B = 0$ T and above the crossover temperature for the field-induced zigzag order. That is, for each temperature $T < 50$ K, magnetic field B, and time t, the residual signal is given by:

$$\frac{\Delta R}{R}_{residual}(T, B, t) = \frac{\Delta R}{R}(T, B, t) - \frac{\Delta R}{R}(50K, B, t)/10. \tag{4.3}$$

The factor of 10 is used to scale the $\Delta R/R$ scan taken at 50 K because this data was taken with a pump fluence of $F = 50\mu J/cm^2$, whereas the $\Delta R/R$ scans at lower temperatures were taken with a pump fluence of $F = 5\mu J/cm^2$ which is a factor of 10 lower. This was done to increase the signal-to-noise ratio when the signal was small. We justify this linear scaling in Supplementary Note 4.7.5.

The data shown in Fig. 4.3 is given by $\frac{\Delta R}{R}_{residual}(T, B, t)$ described here. This subtraction reduces the number of necessary fit parameters to describe the dynamics, and this method does not rely on a model.

One assumption this method uses is that the time-scales of the non-magnetic response is temperature-independent. We show that the time-scales of the fast response is temperature independent in Fig. 4.7 where we show the normalized response at various temperatures.

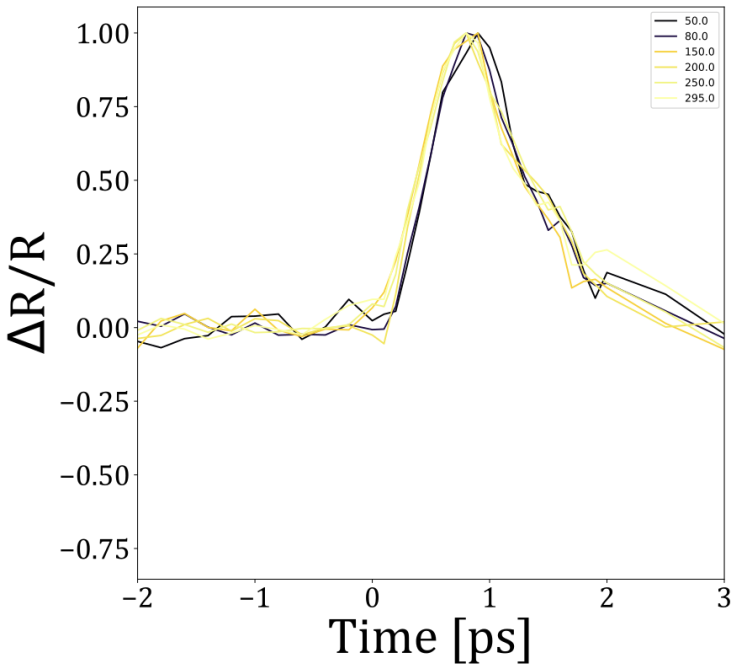

Figure 4.7: Normalized $\Delta R/R$ at high temperatures

4.7.3 Supplementary Note 3: Fitting raw time-domain data

The raw TRR data can be fit accurately according the following function [5]:

$$\frac{\Delta R}{R}(t) = \int_{-\infty}^{+\infty} (f_e(t') + f_m(t')) \cdot g(t - t')dt' \tag{4.4}$$

$$f_e(t) = \begin{cases} 0 & t < 0, \\ A_1 e^{-t/\tau_1} + A_2 e^{-t/\tau_2} + C & t \geq 0. \end{cases} \tag{4.5}$$

$$f_m(t) = \begin{cases} 0 & t < 0, \\ A_3 \cdot \left(1 - e^{-t/\tau_r}\right) \cdot e^{-(t/\tau_{recovery})^\beta} & t \geq 0. \end{cases} \tag{4.6}$$

$$g(t) = \frac{1}{\sigma\sqrt{2\pi}} e^{-\frac{1}{2}\left(\frac{t}{\sigma}\right)^2}. \tag{4.7}$$

In Eqn. 4.4, $f_e(t)$ is the electronic contribution of the pump-induced dynamics, $f_m(t)$ is the magnetic contribution of the pump-induced dynamics, and $g(t)$ is the cross-correlation function of the pump and probe pulses. As shown in Eqn. 4.5, $f_e(t)$ is a bi-exponential decay with a constant off-set C. Eqn. 4.6 shows the model used to describe the material pump-induced dynamics as described in the main text. A_3 is the amplitude, τ_{rise} is the rise time, $\tau_{recovery}$ is the recovery time, and β is the phenomenological stretching exponent. The σ in Eqn. 4.6 is the effective temporal width of the pump and probe pulses.

We fit the above equations to the raw TRR signal in the purely incommensurate (INC) phase at $T = 2$ K, $H = 0$ T, and $F = 5\mu J/cm^2$, shown in black in Supplemental Fig. 4.8. The cyan filled circles are the data points and the colored regions represent the signal components corresponding to the magnetic signal (in yellow) and the electronic signal (in grey). The corresponding fit parameters are shown in the table below.

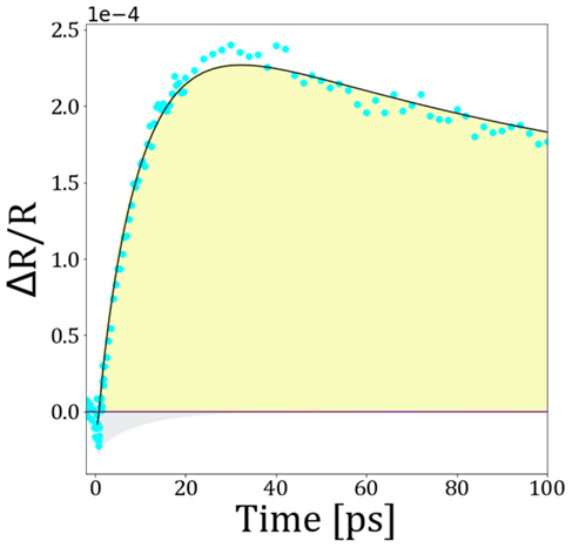

name	value	standard error	relative error	initial value	min	max	vary
t0	0.50000000	0.00000000	(0.00%)	0.5	-inf	inf	False
t1	11.9582902	0.81589297	(6.82%)	10	-inf	inf	True
t2	0.50000000	0.00000000	(0.00%)	0.5	-inf	inf	False
t3	135.028129	67.1586886	(49.74%)	430	-inf	inf	True
A1	-1.0000e-05	0.00000000	(0.00%)	-1e-05	-inf	inf	False
A2	-1.0000e-05	0.00000000	(0.00%)	-1e-05	-inf	inf	False
A3	4.5063e-04	7.3504e-05	(16.31%)	0.00042	-inf	inf	True
A5	0.00000000	0.00000000		0	-inf	inf	False
s	0.30000000	0.00000000	(0.00%)	0.3	-inf	inf	False
b	0.34099814	0.04862415	(14.26%)	0.5	-inf	inf	True

Figure 4.8: Fits and fit parameters of full $\Delta R/R$ dynamics.

4.7.4 Supplementary Note 4: Heating calculations

We estimate the laser-induced heating here. In the simplest case, we assume the absorbed energy density of the pump is given by $E_{absorbed} = \frac{F}{\delta}$, where F is the fluence and δ is the penetration depth. Due to a lack of published optical data on β-Li_2IrO_3, obtain the penetration depth from published data on Na_2IrO_3. We can then numerically integrate published heat capacity data [21] on β-Li_2IrO_3 to obtain the final temperature. Table 4.1 shows the final temperatures for a given initial temperature and pump fluence.

Table 4.1: Calculating laser-induced heating. Each cell shows the final temperature [K] starting from an initial temperature given by the row and a fluence given by the column.

Initial	Fluence $\mu J/cm^2$	
Temperature [K]	5	50
2	20.5	44.4
6	20.8	44.5
10	21.5	44.7
14	22.8	45.0
18	24.6	45.5
22	26.9	46.3
26	29.7	47.3
30	32.9	48.8
34	36.3	50.6
38	39.9	52.8
42	43.6	55.2

4.7.5 Supplementary Note 5: Fluence dependence

Fast signal

The fast peak, which we primarily associate with the impulsive electronic response, has a fluence dependence shown in Figure 4.9 and 4.10. The minimum values of the fast peak are plotted as a function of fluence in Figure Y on a log-log scale. We see that the fluence dependences for this fast peak are relatively linear in the regime from $5\mu J/cm^2$ to $50\mu J/cm^2$ in the high-temperature regimes. This indicates that the purely electronic response encoded in the fast response in the absense of magnetism is linear in fluence. We see that there are small deviations to the linear fluence dependence at lower temperatures, suggesting that there is some dependence of this fast response to properties that don't exist at higher temperatures. This nonlinearity may indicate that even the dynamics in the faster response may be coupled

to magnetic features as we describe in the text. We are unsure of the origin of this non-linearity, and we suggest that this feature merits further study.

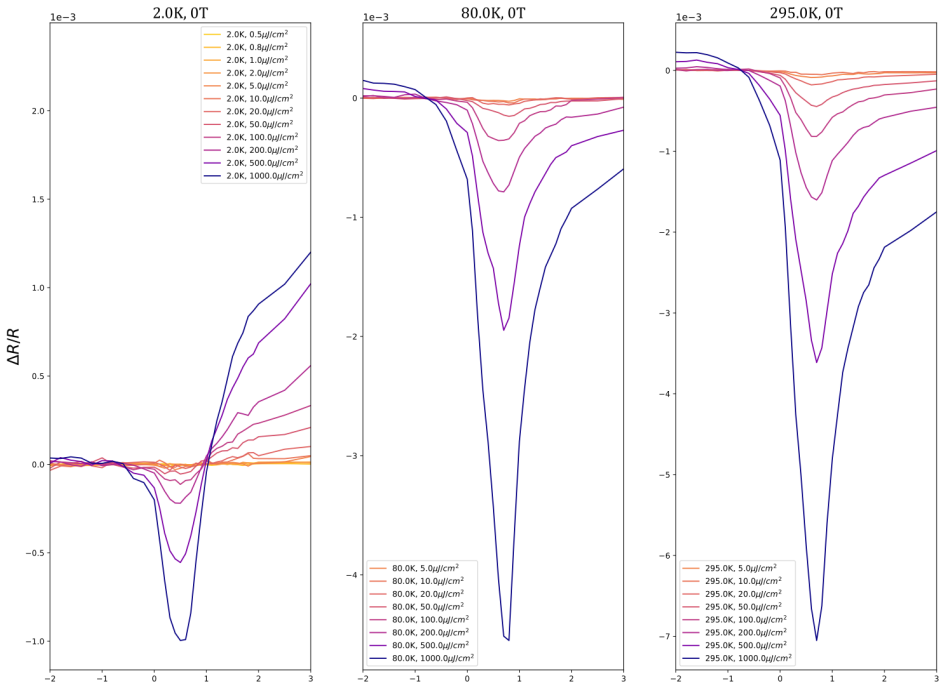

Figure 4.9: Fast component of $\Delta R/R$ signal at various fluences.

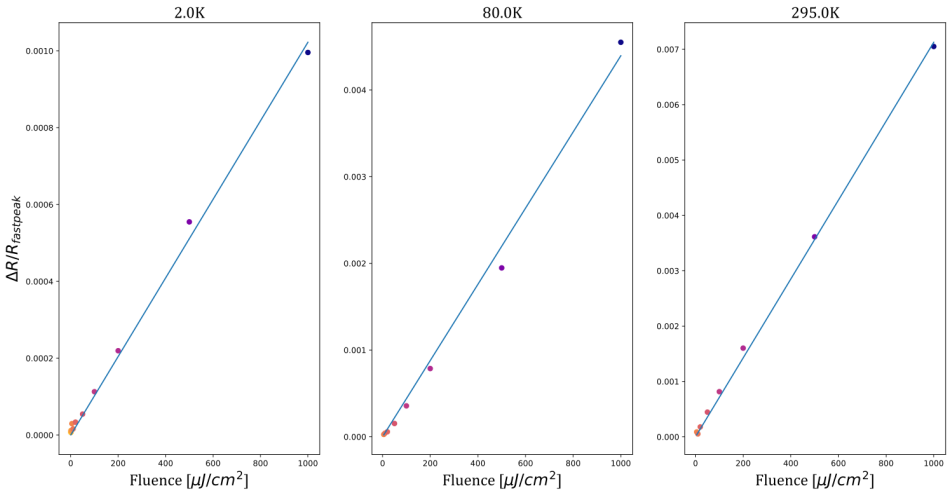

Figure 4.10: Fluence dependence of the amplitude of the fast component of $\Delta R/R$ signal.

Slow signal

We report the fluence dependence of the slow response here. Fig. 4.11 shows the slow response for various fluences at several representative temperatures and magnetic fields. The amplitude of the slow response is shown in Fig. 4.12. Note that the amplitude has a nonlinear dependence on the fluence in the magnetically ordered regimes. We believe that the drastic change in fluence dependence in the $T = 2$ K, $B = 3$ T response is due to a crossover above the field-induced zigzag critical temperature due to laser-induced heating. The non-monotonic behavior of the amplitude in the $T = 80$ K, $B = 0$ T response is particularly peculiar, and may be related to the high-temperature crossover reported in the main text. We note that the fluence dependence merits significant further study.

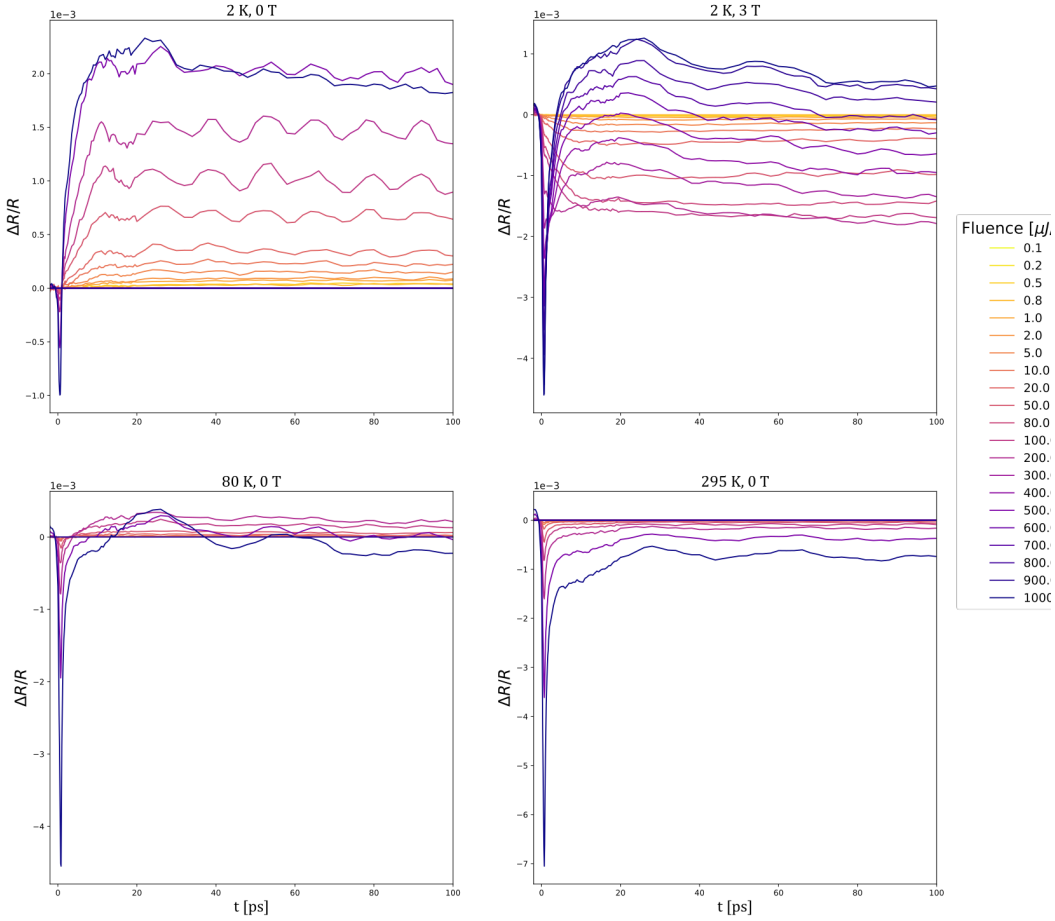

Figure 4.11: Slow component of $\Delta R/R$ signal at various fluences.

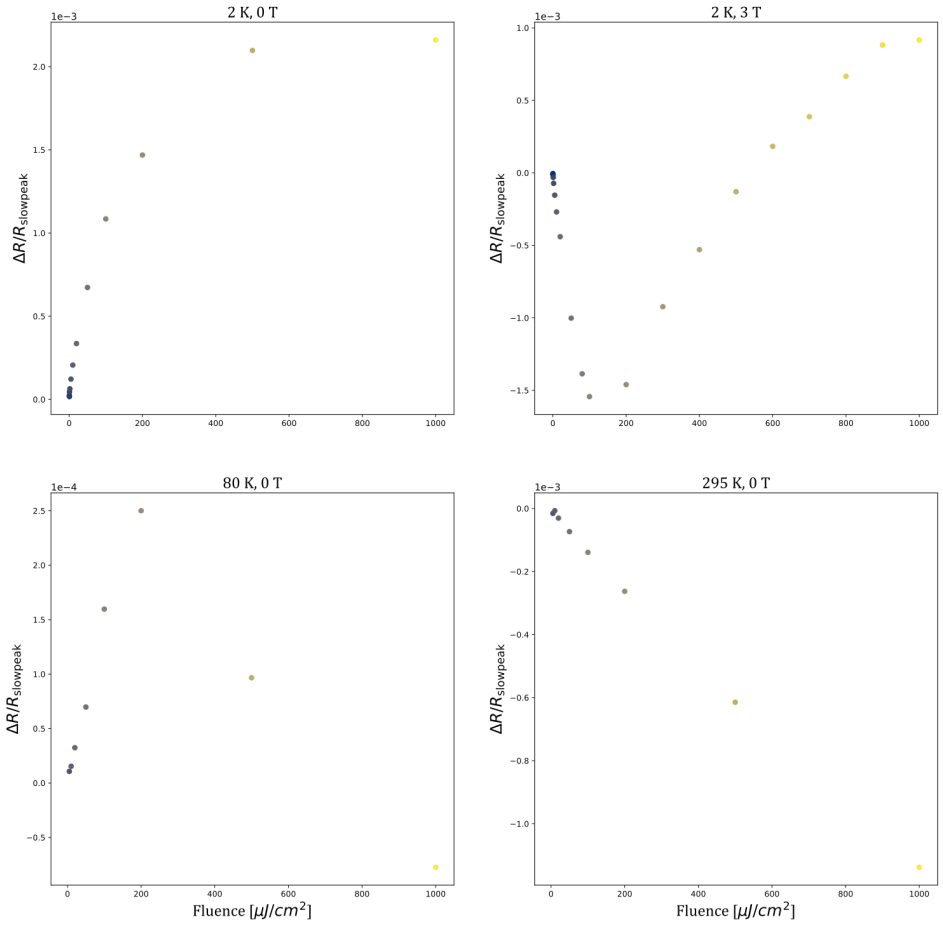

Figure 4.12: Fluence dependence of the amplitude of the slow component of $\Delta R/R$ signal.

Chapter 5

Interlayer magnetophononic coupling in $MnBi_2Te_4$

5.1 Introduction

The realization of magnetic order in functional quantum materials creates a rich platform for the exploration of fundamental spin-based phenomena, as exemplified in strongly correlated materials[68], multiferroics[69], and more recently, magnetic topological materials [70]. As such, these materials hold great promise for application in spintronics, magnetic memory, and quantum information technology. A new paradigm has recently emerged with the discovery of atomically thin magnets, derived from layered, quasi-two-dimensional materials[71]. In such materials, magnetic order is characterized by strongly anisotropic exchange interactions, with interlayer exchange coupling that is an order-of-magnitude weaker than the in-plane exchange coupling. The weak interlayer exchange coupling offers a high degree of tunability in the two-dimensional limit, enabling the realization of phenomena such as magnetic switching via electric fields[72] and electrostatic doping[73]. Such tunability could potentially be made even more potent in combination with additional functionalities

such as those outlined above. For instance, the $Mn(Bi,Sb)_{2n}Te_{3n+1}$ family of layered antiferromagnets is the first experimental realization of intrinsic magnetic order in topological insulators[74, 75, 76]. The interlayer magnetic order is intimately connected to the band topology, with experimental demonstration of switching between quantum anomalous Hall and axion insulator states[77], and realization of a field-driven Weyl semimetal state1[78]. In this context, the discovery of new, efficient coupling pathways between the interlayer exchange and other microscopic degrees of freedom would not only add to the rich spectrum of low-dimensional magnetic phenomena, but also potentially unlock pathways for the dynamic manipulation of magnetism and band topology.

In this work, we observe that interlayer magnetic order in $MnBi_2Te_4$ is strongly coupled to phonons, manifesting in the optical excitation of zone-boundary phonons that are otherwise forbidden due to the conservation of momentum. This magnetophononic response is a consequence of a coherent wave-mixing process between the antiferromagnetic order and A_{1g} optical phonons, as determined from equilibrium and time-domain spectroscopy across temperature- and magnetic field-driven phase transitions. Our microscopic model based on first-principles calculations reveals that this phenomenon can be attributed to phonons modulating the interlayer exchange coupling.

5.2 Methods

5.2.1 Crystal growth and characterization

Single crystals of $MnBi_2Te_4$ were grown using a self-flux method11. Mixtures of 99.95% purity manganese powder, 99.999% bismuth shot, and 99.9999+% tellurium ingot with a molar ratio Mn:Bi:Te = 1:5:16 were loaded into an aluminum crucible and sealed in evacuated quartz tubes. The mixture is heated upto 1173 K for 12

hours and slowly cooled down at the rate of 1.5 K/hour to within 863 K – 903 K. This is followed by centrifugation to remove excess flux. The phase and crystallinity of the single crystals were checked by X-ray diffraction. The antiferromagnetic order with the Néel temperature of 24 K was confirmed using SQUID magnetometry.

5.2.2 Raman spectroscopy measurements

Temperature-dependent Raman spectra were collected using a Horiba LabRam HR Evolution with a freespace Olympus BX51 confocal microscope. A 632.8 nm linearly polarized HeNe laser beam was focused at normal incidence using a LWD 50x objective with a numerical aperture of 0.5, with the confocal hole set to 100 μm. A Si back-illuminated deep depleted array detector and an ultra-low-frequency volume Bragg filter were used to collect the spectra, dispersed by a grating (1800 gr/mm) with an 800 mm focal length spectrometer. The system was interfaced with an Oxford continuous-flow cryostat for low-temperature measurements, using liquid helium as the cryogen.

Field-dependent magneto-Raman spectra were collected using a home-built Raman spectrometer. A 632.8 nm linearly polarized HeNe laser beam was focused at normal incidence using a LWD 50x objective with a numerical aperture of 0.82. A Si back-illuminated deep depleted array detector and a set of ultra-low-frequency volume Bragg filters were used to collect the spectra, dispersed by a grating (1800 gr/mm) with a 300 mm focal length spectrometer. The system was interfaced with an Attocube AttoDRY 2100 closed-cycle cryostat for low-temperature, high magnetic field measurements, using liquid Helium as the cryogen. The field-induced Faraday rotation in the objective was calibrated and corrected using a half-waveplate.

The laser power was maintained below 50 μW in all measurements, to minimize laser heating and maintain the power well below the damage threshold. Laser heating was calibrated by measuring Raman phonon peak shifts as a function of and

using thermal conductivity values from reference[79]. Polarized spectra were obtained using a half-waveplate to rotate the polarization of the incident beam, with a fixed analyzer. After peak assignment using polarization analysis, temperature- and field-dependent spectra were collected without a polarizer, to maximize signal throughput. Spectra were averaged over 60 minutes and 120 minutes in the case of temperature-dependent and field-dependent measurements respectively, with a temperature stability of ± 0.1 K. Any subtle drift in the spectrometer (<0.15 cm^{-1}) over the temperature-dependent studies was corrected using the HeNe line at 632.8 nm.

The $A_{1g}^{(1)}$ peak was fit using an inverse Fano lineshape in combination with a linear background. Its lineshape is given by the expression $I(\omega) = \frac{(q\Gamma-(\omega-\omega_0))^2}{\Gamma^2+(\omega-\omega_0)^2}$, where I is the scattering intensity, ω is the energy, ω_0 and Γ are the resonant energy and linewidth of the excitation respectively, and 1/q is a measure of the peak asymmetry. The $E_g^{(2)}$, and $A_{1g}^{(3)}$ peaks were fit with a standard Gaussian lineshape, and the $E_{1g}^{(3)}$ and $A_{1g}^{(2)}$ peaks were fit with a standard Lorentzian lineshape. A nonlinear least-squares fitting procedure was used. To ensure robustness of the temperature-dependent fits, the same initial fit values and constraints were used for each set of temperature-dependent and field-dependent spectra.

5.2.3 Magnetic field-dependent ultrafast optical spectroscopy

Ultrafast optical pump-probe measurements were carried out using a 1040 nm 200 kHz Spectra-Physics Spirit Yb-based hybrid-fiber laser coupled to a noncollinear optical parametric amplifier. The amplifier produces <50 fs pulses centered at 800 nm (1.55 eV), which is used as the pump beam. The 1040 nm (1.2 eV) output is converted to white light, centered at 1025 nm with a FWHM of 20 nm, by focusing it inside a YAG (Yttrium Aluminum Garnet) crystal. The white light is subsequently compressed to $\sim$50 fs pulses using a prism compressor pair and is used as the probe beam. The pump and the probe beams are aligned to propagate along the [001] axis

of the crystal, at near normal incidence.

The samples were placed in a magneto-optical closed-cycle cryostat (Quantum Design OptiCool). Pump-probe measurements were carried out as a function of magnetic field applied normal to the sample surface (along the [001] direction). The sample temperature was fixed at 2 K. A pump fluence of ∼100 µJ/cm2 was used in order to generate sufficiently large coherent phonon oscillations, while keeping the transient heating to a minimal amount, to ensure we avoid melting of the magnetic order.

5.2.4 Ultrafast electron diffraction measurements

Ultrafast electron diffraction measurements were carried out at the MeV-UED beamline at the SLAC National Accelerator Laboratory. The principle and other technical details of the experimental setup are outlined elsewhere[80]. A 60-fs laser pulse with a photon energy of 1.55 eV and fluence of 7 mJ/cm^2 were used to excite the sample. A higher pump fluence was required than in the optical pump-probe measurements, in order to produce a sufficiently large pump-induced change in diffraction intensities. Fluence-dependent damage studies revealed no signs of laser-induced damage, and the measurements were repeatable over thousands of cycles. Femtosecond electron bunches of ∼100 fs pulsewidth and 3.7 MeV kinetic energy were used to measure pump-induced changes in electron diffraction intensities. Measurements were carried out on flakes with an average thickness of around 100 nm, exfoliated from a single crystal of $MnBi_2Te_4$ and transferred onto an amorphous Si_3N_4 membrane using an ex-situ transfer stage. The flakes were protected with an additional layer of amorphous Si_3N_4 to prevent degradation. The spot sizes of the pump and probe beams were 464×694 μm and ∼70 μm, respectively, and the measurements were carried out at 30 K. The ultrafast electron diffraction intensities were obtained by averaging over several scans, normalizing individual diffraction images to account

for electron beam intensity fluctuation. Individual diffraction peaks were fit to a two-dimensional Gaussian function, and then averaged over symmetry-related peaks based on the R-3m space group of $MnBi_2Te_4$.

5.2.5 Pump-probe data analysis

The time-resolved reflectivity traces were first fitted to a product of an error function and a biexponential decay function. The error function models the excitation of photo-carriers and instrumental temporal resolution, and the exponential decay is an approximation for the sum of various unknown processes occurring over the measured time delay, including electron-electron and electron-phonon thermalization. The functional form is:

$$\left(1+\operatorname{erf}\left(\frac{t}{\tau_r}\right)\right)\times\left(A_1\,\exp\left(-\frac{t}{\tau_1}\right)+A_2\,\exp\left(-\frac{t}{\tau_2}\right)+C\right), \tag{5.1}$$

where t is the time delay, τ_r is the rise time for the excitation of photo-carriers, τ_1 and τ_2 are the time constants of exponential decay, and A_1, A_2, and C are constants. Upon subtracting the biexponential decay, the residual traces were fit to the sum of two decaying sinusoidal functions. The functional form is:

$$A_1\sin\left(2\pi f_1 t+\phi_1\right)\exp\left(-\frac{t}{\tau_{d1}}\right)+A_2\sin\left(2\pi f_2 t+\phi_2\right)\exp\left(-\frac{t}{\tau_{d2}}\right), \tag{5.2}$$

where t is the time delay, f_1 and f_2 are the frequencies of the sinusoidal functionals, corresponding to the $A_{1g}^{(1)}$ and $A_{1g}^{(2)}$ phonons, ϕ_1 and ϕ_2 are the phases, and τ_{d1} and τ_{d2} are the time constants of exponential decay of the oscillations. The initial amplitudes A_1 and A_2 are plotted in Fig. 5.4d. The ultrafast electron diffraction intensities were fit to an exponential decay function of the form:

$$A_1\exp\left(-\frac{t}{\tau_l}\right)+C, \tag{5.3}$$

where t is the time delay, τ_l is the time constant, and A_1 and C are constants.

5.2.6 Electronic structure and phonon calculations

Density functional theory calculations were carried out using the Vienna Ab Initio Simulation Package (VASP)[81, 82, 83, 84, 85] with the PBE exchange correlation functional[86] and van der Waals correction via the DFT-D3[87, 88] method with Becke-Jonson damping. A Hubbard U was also added to the Mn (4 eV) using Dudarev's[89] approach. A non-primitive cell containing two Mn atoms was used to obtain the equilibrium geometry of the system with AFM-A magnetic structure. Γ-point phonons were obtained with the finite displacement method on a $1 \times 1 \times 1$ 'supercell' using the PHONOPY software package[90] and VASP. An energy cutoff of 300 eV was used for all calculations. A $4 \times 4 \times 4$ Γ-centered k-point mesh was used for equilibrium relaxations and phonon calculations. The general energy convergence threshold was 1×10^{-8} eV and the force convergence threshold for relaxation was 1×10^{-5} eV/Å. When including SOC in the magnetic parameter calculations, however, the energy convergence threshold was 1×10^{-6} eV. Gaussian smearing with a 0.02 eV width was also used in all relaxation and single-point energy calculations. Density of states calculations employed the tetrahedron method. The metallic state was modelled by electron doping the unit cells with 0.1 electron/Mn atom. Supercells for magnetic exchange calculations were generated using VESTA[91].

5.2.7 Exchange coupling constants calculations

Magnetic exchange parameters were obtained by considering a model spin Hamiltonian of the form $H = -\sum_{\langle ij \rangle} J_{ij} S_i \cdot S_j$, where J_{ij} includes intra-layer exchange parameters J_1 and J_2 and inter-layer exchange parameter $J^{\perp}$. A $\sqrt{2} \times \sqrt{2} \times 1$ supercell of the conventional cell was used get the intra-layer exchange parameters, while a $1 \times 1 \times 2$ supercell of the primitive cell was used to get the inter-layer exchange parameter. Γ-centered k-point meshes of $4 \times 4 \times 1$ and $4 \times 4 \times 4$ were used in the respective calculations.

For the intra-layer exchange parameters, one FM and two AFM configurations (stripe and up-up-down-down) were used. The spin exchange energy equations in terms of magnetic exchange parameters for structures of $R3\bar{m}$ symmetry are as follows:

$$E_{FM} = 3E_{NM} - 60J_1 S_i \cdot S_j - 60J_2 S_i \cdot S_j, \tag{5.4}$$

$$E_{AFM1} = 3E_{NM} + 12J_1 S_i \cdot S_j + 12J_2 S_i \cdot S_j, \tag{5.5}$$

$$E_{AFM2} = 3E_{NM} + 12J_1 S_i \cdot S_j - 12J_2 S_i \cdot S_j. \tag{5.6}$$

For the inter-layer exchange parameter, one FM and one AFM configuration were used.

$$E_{FM} = E_{NM} - 6J^{\perp} S_i \cdot S_j, \tag{5.7}$$

$$E_{AFM} = E_{NM} + 6J^{\perp} S_i \cdot S_j. \tag{5.8}$$

The calculated values were multiplied by S^2 to obtain the exchange coupling in meV, assuming the spin of the local moment is $S = 5/2$.

5.3 Results

5.3.1 Spectroscopic evidence of magnetophononic coupling

$MnBi_2Te_4$ exhibits magnetic order below a temperature of $T_N = 24$ K, with in-plane ferromagnetic coupling, and out-of-plane antiferromagnetic (AFM) coupling[92], as shown in Fig. 5.1a. With an applied out-of-plane magnetic field, a spin-flop transition occurs at 3.7 T, developing into a fully polarized ferromagnetic-like state (FM) at a critical field of 7.7 T[92]. We first present measurements of the phonon spectra across the magnetic phase transitions in $MnBi_2Te_4$, using magneto-Raman spectroscopy. The full polarized Raman phonon spectra, selection rules, and peak assignments can be found in Supplementary Note 1. Our peak assignment is fully consistent with a previous study[93] that investigated Raman phonons in thin flakes

of $MnBi_2Te_4$ as a function of number of layers. Here we focus on two fully symmetric 'A_{1g}' phonon modes at frequencies of 49 cm^{-1} and 113 cm^{-1}, labeled $A_{1g}^{(1)}$ and $A_{1g}^{(2)}$ respectively. The phonon eigendisplacements, calculated using density functional theory (DFT) simulations, are shown in Fig. 5.1b. Representative spectra at 0 T, in the AFM phase at 15 K and the paramagnetic (PM) phase at 35 K, are shown in Figs. 5.1c and 5.1d, respectively. We observe that the $A_{1g}^{(2)}$ mode clearly exhibits an anomalous increase in scattering intensity in the AFM phase, which has not been reported in previous studies[93]. The temperature-dependence of the $A_{1g}^{(1)}$ mode is discussed in detail in Supplementary Note 2. In the following, we focus on the magnetic field-dependent behavior. At a magnetic field of 9 T, where $MnBi_2Te_4$ is in the fully polarized ferromagnetic (FM) state, the spectral weight of both modes decreases, as shown in the top panels of Figs. 5.1e and 5.1f. This is highlighted by subtracting the spectrum at 9 T from the spectrum at 0 T and plotting the residual in the bottom panels of Figs. 5.1e and 5.1f. In Figs. 5.1g and 5.1h, the residual is plotted as a function of magnetic field H, upon subtracting the 9 T spectrum. A clear correlation is observed between the residual scattering intensity of the A_{1g} modes and the critical magnetic fields for the spin-flop and FM transitions, denoted by dashed white lines.

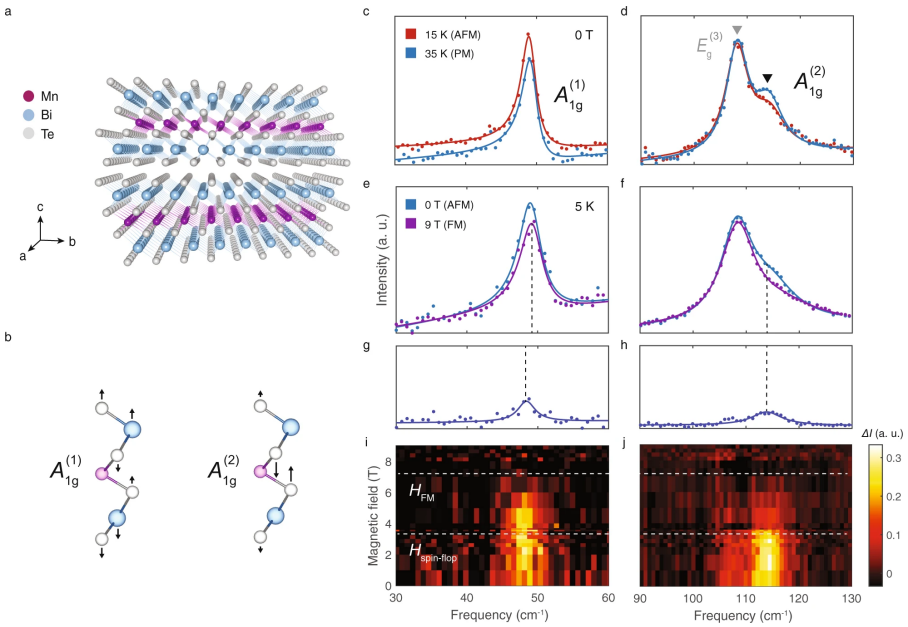

Figure 5.1: **Phonon anomalies across magnetic phase transitions in $MnBi_2Te_4$.** **a** Crystal structure of $MnBi_2Te_4$. **b** Eigendisplacements of the $A_{1g}^{(1)}$ and $A_{1g}^{(2)}$ modes, with arrows denoting displacement of ions. **c, d** Raman spectra of $A_{1g}^{(1)}$ (c) and $A_{1g}^{(2)}$ (d) modes in the paramagnetic (PM) and antiferromagnetic (AFM) phases at 0 T, shown in red and blue respectively. **e, f** Raman spectra of $A_{1g}^{(1)}$ (e) and $A_{1g}^{(2)}$ (f) modes in the AFM and ferromagnetic (FM) phases at 5 K, shown in blue, and purple respectively. **g, h** The difference between spectra in the AFM and FM phases. **i, j** Contour plots of the difference upon subtracting the 9 T spectrum, as a function of magnetic field. The dotted lines denote the FM and spin-flop critical fields.

The fractional change in integrated intensity of the $A_{1g}^{(2)}$ mode is plotted as a function of temperature in Fig. 5.2a (green dots). The integrated intensity folgrlows the AFM order parameter, tracked by the (1 0 5/2) neutron diffraction Bragg peak[79] (purple dots). The grey line is a fit to the power law $I \propto (1 - \frac{T}{T_N})^{2\beta}$, with β = 0.35 as in the reference[79]. Furthermore, a plot of the scattering intensity of the

$A_{1g}^{(1)}$ and $A_{1g}^{(2)}$ modes (Fig. 5.2b) as a function of magnetic field reveals the fractional change in integrated intensities of both modes tracks the AFM order parameter[94] across the spin-flop transition at 3.7 T, and into the fully polarized ferromagnetic state above 7.7 T. The integrated intensities of the $A_{1g}^{(1)}$ and $A_{1g}^{(2)}$ modes increase by fractions of 0.15 and 0.3 respectively, in the AFM phase, as compared to the FM phase at 9 T. Additionally, the fractional increase in the $A_{1g}^{(2)}$ intensity as estimated from the PM to AFM transition and FM to AFM transition in Figs. 5.2a and 5.2b, respectively, are of the same magnitude, pointing to a common origin. Importantly, within the limits of our experimental uncertainty (error bars in plots), we do not observe such large changes in the integrated intensity on any of the other Raman phonons (see Supplementary Note 3 for detailed field-dependent data). Below, we show that the experimentally observed temperature- and field-dependent evolution of scattering intensity is consistent with the excitation of 'forbidden' zone-boundary modes of the $A_{1g}^{(1)}$ and $A_{1g}^{(2)}$ phonon branches.

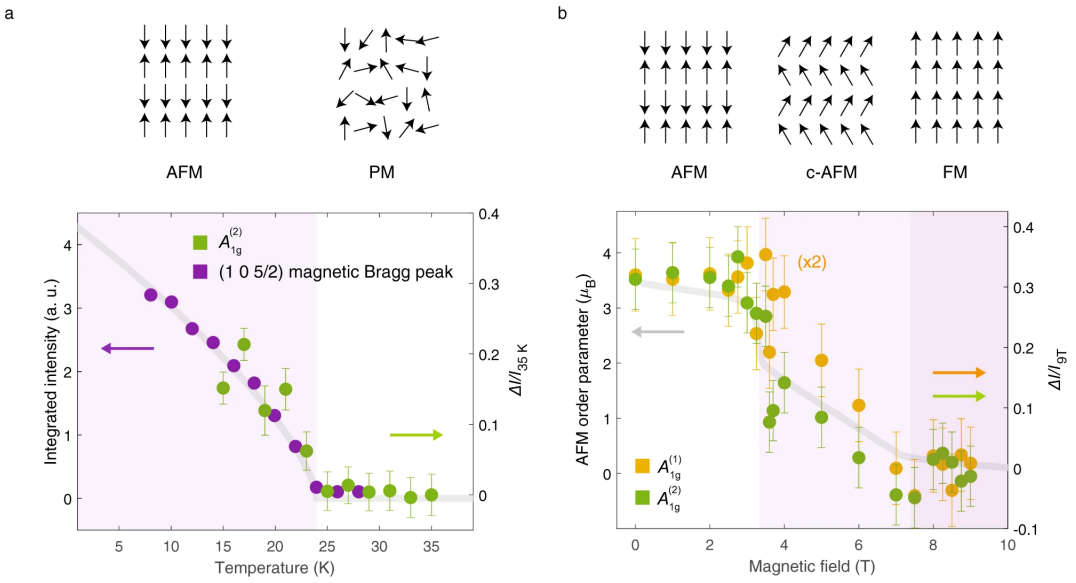

Figure 5.2: **Phonon intensities track the antiferromagnetic order parameter.** **a** Temperature-dependent fractional change in integrated intensity, $\Delta I/I_{35K}$, of the $A_{1g}^{(2)}$ mode, overlayed on integrated intensity of the (1 0 5/2) neutron diffraction peak from reference[79] The gray line is a fit to $A(1-T/T_N)^{2\beta}$, with $\beta = 0.35$, $T_N = 24$ K. **b** The field-dependent fractional change in integrated intensity, $\Delta I/I_{9T}$, of the $A_{1g}^{(2)}$ and $A_{1g}^{(2)}$ modes. The gray line is the AFM order parameter, given by $M - 4.5\mu_B$, where M is the magnetization measured by magnetometry from reference[94]. Error bars are standard deviations in fit values.

The AFM order along the out-of-plane direction (crystallographic c-axis) results in a magnetic unit cell that is double the size of the crystallographic unit cell, as shown in Fig. 5.3a. In contrast, in the high-field FM state (and the paramagnetic state), the magnetic unit cell is identical with the crystallographic unit cell, as in the paramagnetic state. This behavior manifests in the anomalous field-dependent scattering intensity of the A_{1g} modes, which follows the AFM order parameter with the magnetic unit cell doubling resulting in a folding of the phonon Brillouin zone, allowing for the optical detection of zone-boundary phonon modes. DFT simulations

of the phonon dispersion along the out-of-plane direction reveal a flat dispersion for the $A_{1g}^{(2)}$ mode, and a small dispersion for the $A_{1g}^{(1)}$, consistent with the weak interlayer van der Waals interaction, and our experimental results, denoted in Fig. 5.3b using bold circles. This supports our assignment of the anomalous scattering intensity as zone-boundary modes. We also consider and rule out alternative explanations for the observed temperature- and magnetic field-dependent scattering intensity changes, such as resonant Raman effects (see Supplementary Note 5) and possible magnon resonances overlapping with the considered phonons (see Supplementary Note 6).

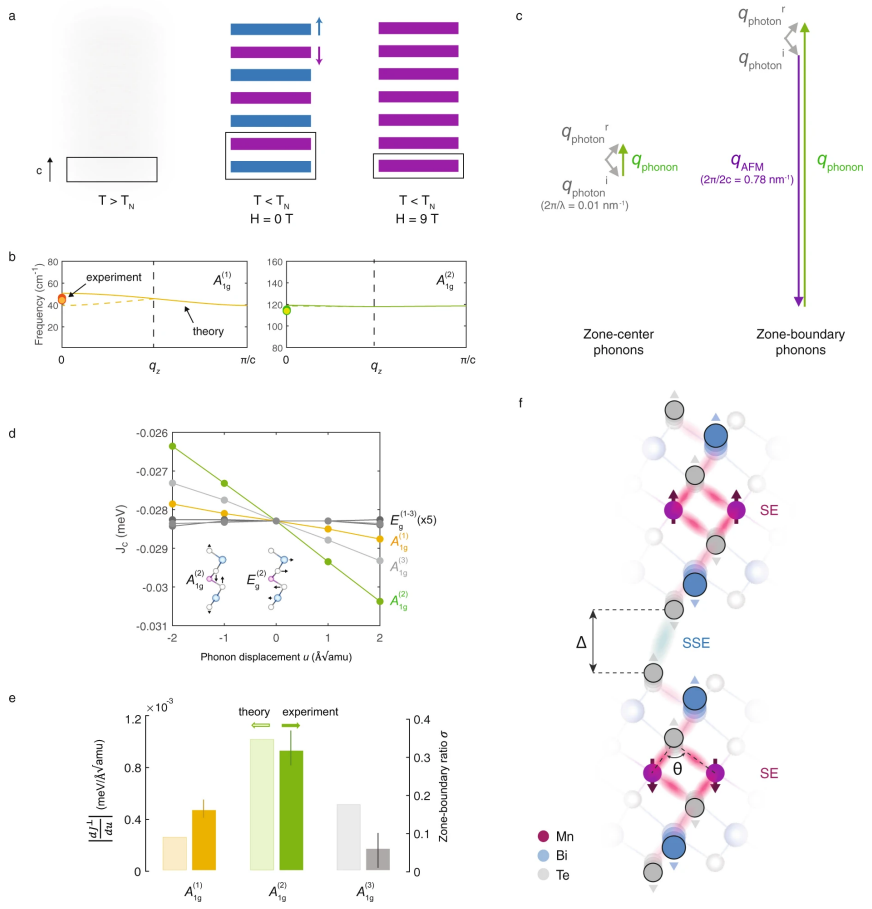

Figure 5.3: **Magnetophononic wave-mixing.** **a** Schematic of layered magnetic ordering in $MnBi_2Te_4$, with blue and purple denoting opposite in-plane spin orientations, and gray denoting disordered spins. The antiferromagnetic (AFM) wavevector is shown schematically, labeled qAFM. **b** The dispersion relations of the $A_{1g}^{(1)}$ and $A_{1g}^{(2)}$ modes along the c-axis, calculated using density functional theory. The experimental zone-center and zone-boundary phonon frequencies are denoted using colored and empty circles respectively. **c** Schematic of wave-mixing for zone-center and zone-boundary modes. The wavevectors of the photon (i=incident, r=reflected), phonon, and AFM spin-wave are shown using gray, green, and purple arrows (not drawn to scale). **d** Modulation of the interlayer exchange coupling by Raman phonons. Inset shows the eigendisplacements of two representative phonons. **e** Comparison between the calculated magnetophononic scattering cross-section $|\frac{dJ^{\perp}}{du}|$ and the experimental

Figure 5.3: zone-boundary ratio σ (see text for definition). Error bars are standard deviations in fit values. **f** Schematic of superexchange (SE) and super-superexchange (SSE), with Δ denoting the interlayer distance, θ denoting the Mn–Te–Mn bond angle, and pink and blue clouds denoting SE and SSE pathways, respectively.

Magnetic unit cell doubling resulting in the activation of zone boundary phonons is unexpected given the absence of a structural phase transition. Refinement based on neutron diffraction at 10 K and 100 K shows no structural unit cell doubling across the AFM transition, and no changes to the unit cell coordinates to within 10^{-3} of the lattice parameters[79]. The negligible change in the spectra of other Raman phonons in $MnBi_2Te_4$ is also consistent with the absence of a structural transition of any kind, and points instead to a mechanism that is mode-dependent.

5.3.2 Microscopic model of magnetophononic wavemixing

In general, zone-boundary modes are optically inactive or 'forbidden' due to the conservation of crystal momentum. Photons in the visible part of the spectrum have negligible momentum in comparison with the crystal Brillouin zone, and thus momentum conservation dictates that only zero momentum (i. e. zone-center) excitations can be generated and detected in first-order scattering processes. This is shown schematically for Raman scattering in Fig. 5.3c. This selection rule can be overcome in the presence of other finite momentum waves in the crystal, as observed for instance in the case of structural distortions that double the crystallographic unit cell[95, 96, 97]. However, as noted above, $MnBi_2Te_4$ does not exhibit any structural transition. Instead, we propose that the crystal momentum is provided by the AFM order, via a magnetophononic wave-mixing process. This is shown schematically in Fig. 5.3c, where the AFM crystal momentum $q_{AFM} = 2\pi/2c$ interacts with the phonon crystal momentum, allowing for the excitation of zone-boundary ($q = \pi/c$)

phonons.

Magnetophononic wave-mixing requires a sufficiently strong scattering cross-section to be observable. This scattering cross-section can typically be written in terms of an interaction term in the free energy. For example, the Raman scattering process is due to a coupling of the incident (E^i) and reflected (E^r) electric fields to a distortion u along a phonon normal mode, via the susceptibility χ_e (i. e. $F = (\frac{d\chi_e}{du}u)E^iE^r$). In the case of a finite-momentum structural distortion, phonons couple to the structural distortion through elastic interactions. Analogously, in our model of magnetophononic wave-mixing, phonons couple to the AFM order by modulating the interlayer exchange interaction $J^\perp$. The corresponding interaction term in the free energy can be obtained by first writing down a Heisenberg-like Hamiltonian for the spin energy, $H = \Sigma_{ij}J_{ij}S_i \cdot S_j$, where J_{ij} is the exchange coupling between spins at sites i and j. Since the coupling is to an out-of-plane antiferromagnetic spin wave, we focus on the interlayer (out-of-plane) exchange coupling $J^\perp$ (only nearest-neighbor interlayer interactions are considered). If a phonon modulates the interlayer exchange interaction, the perturbed exchange coupling $J^{\perp\prime}$ can be written as

$$J^{\perp\prime} = J^\perp + \frac{dJ^\perp}{du}u + \dots \tag{5.9}$$

Equation 5.9 is a special case of what is broadly referred to in the literature as 'spin-phonon coupling' (see Supplementary Note 4 for the interpretation of higher-order terms in terms of phonon frequency renormalization). Based on this, the free energy term that couples the antiferromagnetic spin wave to the phonon is, to first order,

$$F = (\frac{dJ^\perp}{du}u)\sum_i S_iS_{(i+1)}, \tag{5.10}$$

where i and i+1 correspond to nearest-neighbor spin pairs in the out-of-plane direction. It is clear that the magnitude of this coupling directly depends on $\frac{dJ^\perp}{du}$.

In other words, a magnetophononic wave-mixing is possible only when the phonon mode under consideration sufficiently modulates the interlayer exchange coupling.

A microscopic basis for this model can be obtained using DFT simulations. We simulate the modulation of the interlayer exchange coupling $J^{\perp}$ by the six Raman phonons of $MnBi_2Te_4$, which include three A_{1g} modes (pure out-of-plane eigendisplacements), and three E_g modes (pure in-plane eigendisplacements, see Supplementary Fig.5.5b for eigendisplacements). The results, shown in Fig. 5.3d, indicate a striking dichotomy between the out-of-plane A_{1g} modes and in-plane E_g modes. The A_{1g} modes exhibit an order-of-magnitude larger modulation of $J^{\perp}$ than the E_g modes. Furthermore, the $A_{1g}^{(2)}$ mode has by far the largest influence on $J^{\perp}$, consistent with our experimental observation of zone-boundary scattering intensity. A quantitative comparison of this model with our experimental results is possible. This is accomplished by defining an experimental magnetophononic scattering cross-section σ, as the ratio of the integrated intensity of the zone-boundary mode (i. e. the residual spectra in Fig. 5.1d) to that of the zone-center mode (spectra at 9 T in Fig. 5.1d). The scattering cross-section is compared to the calculated interaction term, $|\frac{dJ^{\perp})}{du}|$. The plotted results in Fig. 5.3e show a good agreement between theory and the experiment. In particular, the model reproduces the experimental observation of the $A_{1g}^{(2)}$ mode exhibiting the largest zone-boundary scattering intensity. We note that no signature of a zone-boundary mode was observed in the $A_{1g}^{(3)}$ branch within the experimental uncertainty (see Supplementary Note 3). Finally, also in agreement with the theoretical prediction, no E_g zone-boundary modes were experimentally observed, i. e. σ=0 for all E_g modes, within the experimental uncertainty (see Supplementary Note 3).

The theoretical results outlined above can be rationalized in terms of microscopic interlayer exchange pathways. In general, the exchange coupling across a van der Waals (vdW) gap is understood to be the result of a process named 'super-superexchange' (SSE)[98]. In SSE, given that the interlayer exchange interaction is

usually much weaker than the intralayer exchange interaction, the two can be effectively decoupled. The individual quasi-two-dimensional layers are treated as macroscopic magnetic moments established by the intralayer superexchange (shown in pink in Fig. 5.3f), which couple across the vdW gap via the weaker interlayer exchange (shown in blue in Fig. 5.3f). As in any exchange process, geometrical parameters that influence the relevant hopping integrals play a major role. In superexchange, the angle between magnetic ions and its ligands mediates the superexchange, in this case the Mn-Te-Mn bond angle θ shown in Fig. 5.3f. These structural superexchange interactions are further controlled by orbital hybridization with cationic Bi p states tuned by the nearest-neighbor ions across the vdW gap[99], in this case, determined by the Te-Te distance Δ shown in Fig. 5.3f, to stabilize the FM interlayer coupling in $MnBi_2Te_4$.

We first note that A_{1g} modes in $MnBi_2Te_4$ modulate Δ, whereas E_g modes do not, an observation that accounts for the dichotomy of their respective influence on $J^{\perp}$. Of the A_{1g} modes, examining the eigenvectors in Fig. 5.1b and Supplementary Fig. 5.5b, $A_{1g}^{(2)}$ exhibits the largest modulation of the Mn-Te-Mn bond angle θ. The modulation of θ by the $A_{1g}^{(2)}$ mode is a factor of 2 larger than by $A_{1g}^{(1)}$, which in turn is a factor of 5 larger than by $A_{1g}(3)$. This rationalizes the trend seen in the calculated $\frac{dJ^{\perp})}{du}$ in terms of the SSE pathways.

5.3.3 Time domain signatures of magnetophononic coupling

Finally, we investigate magnetophononic coupling by direct measurement of phonons in the time domain. To do this, we carry out 'pump-probe' experiments to generate and detect coherent optical phonons as a function of magnetic field (see schematic in Fig. 5.4a). Excitation with ultrafast optical pump pulses (1.55 eV, 50 fs) results in the generation of coherent phonon oscillations. A second, time-delayed probe pulse (1.2 eV, 50 fs) measures pump-induced changes in the transient reflectivity

(ΔR/R). The transient reflectivity is sensitive to changes in carrier density and coherent phonons. These measurements are carried out at 2 K, as a function of magnetic field from 0 to 6.4 T, across the spin-flop transition. The transient reflectivity, shown in Fig. 5.4b, exhibits an initial sub-picosecond dip, followed by a slow relaxation. Overlayed on this are multiple distinct coherent oscillation components that (as described below), correspond to the $A_{1g}^{(1)}$ and $A_{1g}^{(2)}$ phonons. We normalize the pump-probe reflectivity traces with respect to their maximum amplitudes, to account for field-dependent variation in the absorbed fluence, and thus photocarrier density, which can influence coherent phonon amplitudes (see Supplementary Note 7 and Supplementary Fig. 5.12 for detailed discussion). Upon subtracting bi-exponential fits (black line fit to 0 T data in Fig. 5.4b shown as a representative example), we observe that the normalized phonon oscillation amplitudes in the residual ΔR/R in Fig. 5.4c visibly decrease with increasing magnetic field, much like the phonon spectral weights measured using Raman spectroscopy.

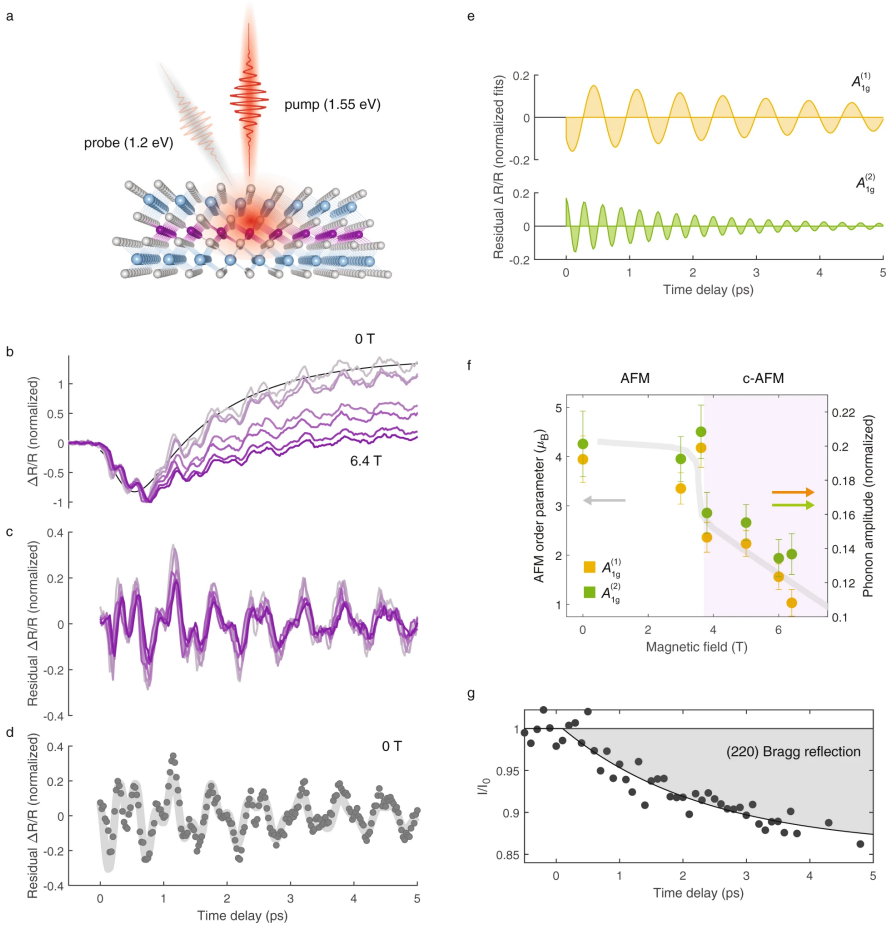

Figure 5.4: **Ultrafast signatures of magnetophononic coupling.** **a** Schematic of pump-probe measurement. **b** Pump-induced changes in the transient reflectivity ($\Delta R/R$) as a function of time delay at various magnetic fields, normalized to the maximum amplitude. The black line is a representative biexponential fit to the 0 T data. **c** The residual $\Delta R/R$ upon subtracting a biexponential fit. **d** Residual $\Delta R/R$ at 0 T, with black dots denoting experimental datapoints and the gray line denoting the fit to the sum of two decaying sinusoidal functions. **e** Individual decaying sinusoidal components obtained from the fit in (**b**), corresponding to the $A_{1g}^{(1)}$ (top) and $A_{1g}^{(2)}$ (bottom) phonons, respectively. **f** Initial amplitude of the coherent $A_{1g}^{(1)}$ and $A_{1g}^{(1)}$ phonons, obtained from fit result in (**d**). The gray line is the antiferromagnetic order parameter from reference[94]. **g** Measured transient electron diffraction intensity of

Figure 5.4: the (2 2 0) Bragg peak, with black dots denoting experimental datapoints, and the black line denoting the fit to an exponential decay function. Error bars are standard deviations in fit values.

The individual oscillatory components are obtained by fitting the residual $\Delta R/R$ to the sum of two exponentially decaying sinusoidal functions (see Methods) as shown for the representative 0 T data in Fig. 5.4d The individual sinusoidal functions, shown in Fig. 5.4e, are readily identified as the $A_{1g}^{(1)}$ and $A_{1g}^{(2)}$ modes at 1.47 THz (49 cm^{-1}) and 3.44 THz (115 cm^{-1}) , respectively. Plotting the amplitudes of the two coherent phonon modes as a function of magnetic field in Fig. 5.4e, it is clear that both modes track the AFM order parameter denoted by the solid grey line, in striking similarity to the field-dependent change in the Raman scattering intensities.

The detection of coherent phonons in pump-probe experiments occurs through a process that is identical to spontaneous Raman scattering[100, 101]. The generation of coherent phonons can also be described within a Raman formalism, with the real and imaginary parts of the Raman tensor responsible for phonon excitation in transparent and absorbing materials, respectively[100]. The similarity of the magnetic-field dependent coherent phonon amplitudes in Fig. 5.4f to the static Raman scattering intensities in Fig. 5.2b thus suggests that these are a consequence of the same mechanism, namely the excitation of zone-boundary phonons via the crystal momentum associated with the antiferromagnetic order.

For resonant excitation of $MnBi_2Te_4$ with 1.55 eV pulses, phonon excitation through the imaginary part of the Raman tensor may be physically thought of in terms of a 'displacive' excitation[102], where the ultrafast excitation of carriers by the pump pulse shifts the quasi-equilibrium coordinates of the lattice in a spatially and temporally coherent manner, generating coherent phonons. Within this picture, magnetophononic zone-folding as described in the previous section would allow for the generation of both zone-center as well as nominally zone-boundary A_{1g} modes.

Additionally, the electronic excitation that shifts the quasi-equilibrium coordinates may itself have a $q_z = \pi/c$ component owing to the contrast in spin-split electronic bands in alternating layers, acting as a direct driving force for the generation of zone-boundary phonons. Unfortunately, the small frequency splitting of the A_{1g} modes precludes the explicit resolution of zone-boundary phonons in the time domain. Nonetheless, it is clear from Fig. 5.4f that the coherent phonons track the AFM order parameter in accord with the magnetophononic wavemixing proposed here.

We note that in general, phonons in time domain measurements are expected to exhibit qualitative deviations from steady-state spectroscopy, owing to the nonequilibrium nature of the former. While the ultrafast carrier excitation in displacive phonon excitation is itself a manifestly nonequilibrium process, additional deviations may emerge from nonequilibrium phonon interactions. We directly measure the timescale of phonon equilibration using ultrafast electron diffraction (see Methods). Here, pump-induced changes in the root-mean-square displacements $\langle u^2 \rangle$ of ions through carrier-lattice and lattice thermalization appear in the transient intensity of Bragg peaks through the Debye-Waller effect (see Supplementary Note 8). These measurements require an order-of-magnitude higher pump excitation fluence than the optical pump-probe measurements in order to produce a discernible signal. Regardless, these high fluence measurements set a lower bound for the phonon thermalization time, as discussed in Supplementary Note 8. As a representative sample, we show in Fig. 5.4g, the transient intensity of the (2 2 0) Bragg peak, with the evolution of the peak intensity fit to an exponential decay (black line). The results indicate that phonon populations indeed remain in a nonequilibrium state through the entire time delay range considered. It is noteworthy that clear signatures of magnetophononic coupling are observed even under such nonequilibrium conditions. Finally, we mention that there may possibly be additional contributions to the coherent phonon amplitudes from magnetodielectric effects which are not explicitly

accounted for here. We discuss the possible contributions to coherent phonon amplitudes due to such an effect Supplementary Note 7.

5.4 Discussion

We have demonstrated that optically 'forbidden' zone-boundary phonons are observed due to magnetophononic wave-mixing in $MnBi_2Te_4$. While it is uncommon for purely magnetic unit cell doubling to give rise to phonon zone-folding effects, such signatures were first observed in transition metal dihalides[103]. These observations were rationalized in terms of phenomenological models of electron-phonon coupling that took into consideration phonon modulation of the spin-orbit coupling and exchange interactions[103, 104]. Our model instead considers the scattering cross-section between the AFM order and phonons, arriving at qualitatively similar conclusions. Importantly, our work provides a description of such a model using first-principles theory. The excellent agreement between the theory and experimental results not only validates the model, but also provides a microscopic basis for the observed phenomena in terms of SSE interlayer exchange pathways. Our work may also help rationalize similar phenomena recently reported[105, 106] in other quasi-two-dimensional magnets such as CrI_3 and $FePS_3$.

Our discovery is especially of significance in light of the critical role played by tunable interlayer exchange interactions in layered magnetic materials. For instance, in $MnBi_2Te_4$, the interlayer magnetic ordering can drive topological phase transitions between quantum anomalous Hall and axion insulator states. Our work unlocks the possibility of controlling the interlayer magnetic ordering in $MnBi_2Te_4$ by exploiting the strong coupling of A_{1g} phonons to $J^{\perp}$. A promising route towards the ultrafast control of magnetism in $MnBi_2Te_4$ is the use of resonant THz excitation to drive large amplitude distortions along A_{1g} modes, as opposed to employing carrier-based mechanisms (such as displacive excitation) that suffer from ultrafast heating effects,

which limit the amplitude of coherent phonons. This may be through anharmonic coupling to Raman active modes[107], or alternatively through sum-frequency ionic Raman scattering[107]. Such mechanisms based on resonant coupling have been used to drive ultrafast light-induced magnetic oscillations and phase transitions, as experimentally demonstrated in other materials[108, 109, 110, 111, 112, 113, 114]. Experimental studies[115] on Bi_2Se_3, a material closely related to $MnBi_2Te_4$, have demonstrated the feasibility of ionic Raman scattering as a way to drive large amplitude oscillations along Raman active modes. Recent theoretical work[116] has outlined an approach based on anharmonic phonon interactions in $MnBi_2Te_4$. In particular, it was shown that resonant excitation of an IR-active A2u phonon (at a frequency of 156 cm^{-1} = 4.7 THz) could drive large amplitude oscillations, which via anharmonic coupling, would drive a unidirectional distortion along Raman-active A_{1g} modes such as the ones identified in the present work. It was predicted that such an approach could be used to drive an AFM to FM transition concurrent with a topological phase transition, using experimentally accessible ultrafast modalities. The magnetophononic wave-mixing in the present work provides an experimental foundation for such approaches and a path towards achieving ultrafast light-induced topological phase transitions.

5.5 Data Availability

Supplementary Information is available for this paper. All the data generated in this study have been deposited in the Figshare database with the
DOI 10.6084/m9.figshare.19102934.

5.6 Supplemental information

5.6.1 Supplemental Note 1: Raman peak assignment and eigenvectors

We start with a systematic analysis of Raman phonon spectra, shown in Supplementary Figure 5.5. The non magnetic unit cell contains seven atoms, and thus there are 21 phonon modes in total, consisting of 18 optical and 3 acoustic modes. Using representation theory, these can be decomposed into irreps of the point group $\bar{3}m$. Of these, only the E_g and A_{1g} modes are Raman active. Polarized Raman spectroscopy measurements are used to readily identify these modes based on their different selection rules. In particular, E_g modes have non-vanishing diagonal Raman tensor components and are thus visible under both parallel8 and cross-polarized configurations, whereas the A_{1g} modes have only diagonal Raman tensor components and are visible only under the parallel-polarized configuration. We did not observe any dependence on the in-plane crystallographic orientation.

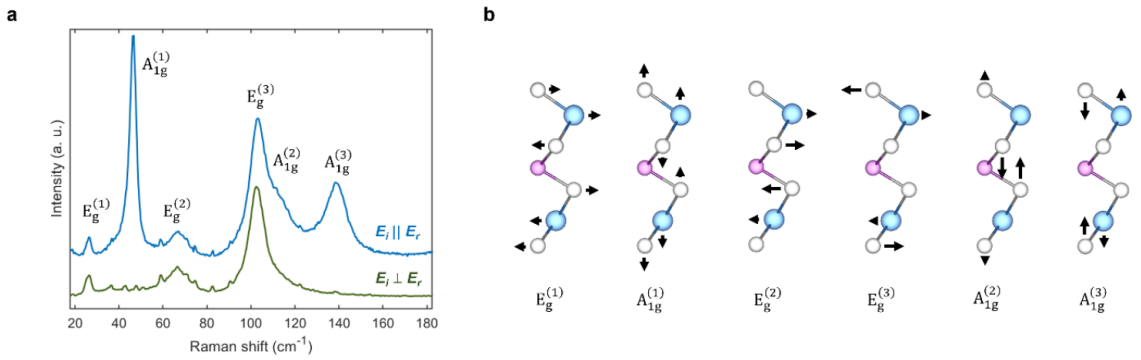

Figure 5.5: **Polarized Raman spectra.** **a**, Raman spectra with the incident and reflected beams parallel- and cross-polarized with respect to each other, at 298 K. **b**, Eigenvectors of Raman phonons, with the arrows denoting ionic motions, calculated using density functional theory simulations. The arrow lengths are proportional to the actual calculated ionic eigendisplacements for all modes.

First-principles calculations are used to enumerate all the Γ-point Raman-active optical phonon modes and their energies in Supplementary Table 5.1. Good agreement is obtained between the calculations and measurements for all the observed Raman phonons, confirming that the first-principles calculations provide a good description of the lattice dynamics.

The phonon eigendisplacements at the Γ point, calculated using density functional theory simulations, show that A_{1g} phonons have purely out-of-plane ionic motions, whereas E_g phonons have purely in-plane ionic motions.

5.6.2 Supplementary Note 2: Anomalous temperature dependence of $A_{1g}^{(1)}$ mode

In Fig. 5.6(a), we plot the Raman spectra measured at 15 K and 300 K, normalized to the height of the $E_g^{(3)}$ peak at ∼113 cm^{-1} , for convenience. We note that the result identified below is independent of the choice of normalization. In

Table 5.1: **Raman phonon mode assignment.** Raman phonon symmetries and frequencies at the Γ point, from density functional theory calculations (theory), and Raman spectroscopy (experiment) at 15 K.

Symmetry	**Frequency cm^{-1} (theory, DFT)**	**Frequency cm^{-1} (experiment, Raman at 15 K)**
E_g	32.9	27.2
A_{1g}	50.7	49.1
E_g	79.8	69.8
E_g	112.9	!08.3
A_{1g}	119.2	113.1
A_{1g}	148.9	146.6

general, phonon peaks in Raman spectra broaden with increasing temperature due to increased phonon-phonon scattering, with resultant lower peak heights. This is visible for instance in the $A_{1g}^{(3)}$ peak at ∼145 cm^{-1}. On the other hand, the scattering intensity of the $A_{1g}^{(1)}$ mode exhibits an anomalous temperature-dependence, with a dramatic decrease in height and integrated intensity, with decreasing temperature (see Fig. 5.6(b)). It is apparent that this decrease in amplitude is independent of the choice of normalization. The amplitude does not show any clear correlation with the magnetic transition at $T_N = 24$ K.

A possible explanation for the dramatic change in scattering intensity with temperature is proximity of the Raman excitation energy (633 nm = 1.96 eV) to electronic transitions correlated with the ionic motion of the $A_{1g}^{(1)}$ mode. Optical conductivity

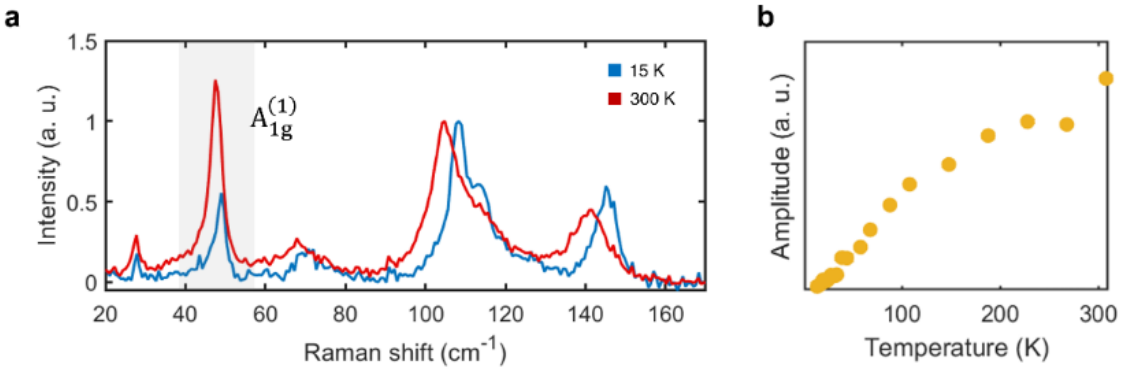

Figure 5.6: **Anomalous temperature-dependence of $A_{1g}^{(1)}$ amplitude. (a)** Unpolarized Raman spectra at 15 K and 300 K, normalized to the height of the $E_g^{(3)}$ peak at ∼115 cm^{-1}. The $A_{1g}^{(1)}$ mode is highlighted in grey. **(b)** The amplitude of the $A_{1g}^{(1)}$ peak, fit to a Fano lineshape, as outlined in the Methods section.

measurements[117] indeed show large changes in the measured temperature range. Such resonant effects may be probed by measuring relative Raman phonon scattering cross-sections as a function of the excitation energy. Resonant effects are discussed in detail in Supplementary Note 5.

The scattering intensity associated with the zone-boundary $A_{1g}^{(1)}$ mode is clearly visible in the field dependent Raman spectra in Fig. 5.1(d) in the main text. In the temperature-dependent Raman spectra in Fig. 5.1(c) however, the anomalous temperature-dependence, described above, appears to swamp the small zone boundary scattering intensity.

5.6.3 Supplementary Note 3: Field-dependence of $E_g^{(2)}$, $E_g^{(3)}$, and $A_{1g}^{(3)}$ spectral weights

The integrated intensities of the $E_g^{(2)}$, $E_g^{(3)}$, and $A_{1g}^{(3)}$ phonons are plotted in Supplementary Figure 5.3a-c, respectively, as a function of magnetic field. The integrated intensities were obtained by fitting individual spectra following the procedure out-

lined in the Methods section, with the error bars denoting the standard deviation in fit values. We note a small dip in the $E_g^{(2)}$ intensity at the spin-flop critical field of 3.7 T. Outside of this, the three modes shown here exhibit no clear field-dependent behavior above the experimental and fitting uncertainty. In particular, there is no signature of coupling to the antiferromagnetic order parameter and the associated zone-boundary phonons.

5.6.4 Supplementary Note 4: Generalized magnetophononic coupling and frequency renormalization

We write down minimal lattice and spin Hamiltonians [118] to describe a generalized magnetophononic coupling. Consider the lattice Hamiltonian described by the harmonic approximation,

$$H_L = H_L^0 + \frac{1}{2!}\frac{\partial^2 H_L^0}{\partial u_\alpha^2}u_\alpha^2 + O(u_\alpha^3) \approx H_L^0 + \frac{1}{2}N\mu_\alpha {\nu_\alpha^0}^2 u_\alpha^2, \tag{5.11}$$

where u_α is the displacement along the phonon normal mode α, μ_α is the reduced mass, ν_α is the frequency, and N is the number of unit cells. The magnetic ground state energy described by a Heisenberg-like Hamiltonian,

$$H_M^0 = -\sum_{ij} J_{ij} S_i \cdot S_j, \tag{5.12}$$

where i and j are spin site indices, and J_{ij} is the isotropic exchange interaction between spins at i and j. When this is perturbed by a zone-center optical phonon α, the perturbed magnetic energy can be derived by considering the derivatives of J_{ij} with respect to the phonon normal mode displacement u_α. Expanding upto second order in u_α , the perturbed exchange interaction is

$$J'_{ij}(u_\alpha) = J_{ij} + \frac{\partial J_{ij}}{\partial u_\alpha}u_\alpha + \frac{1}{2}\frac{\partial^2 J_{ij}}{\partial u_\alpha^2}u_\alpha^2. \tag{5.13}$$

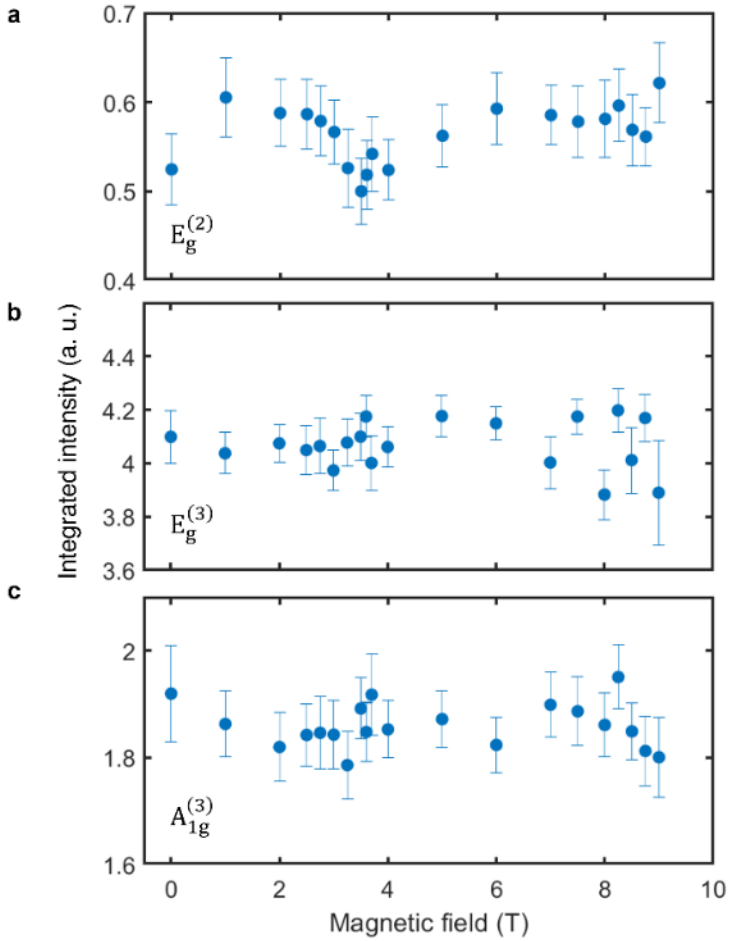

Figure 5.7: **Absence of magnetophononic coupling of other phonons.** The panels show spectral weights of the $E_g^{(2)}$, $E_g^{(3)}$, and $A_{1g}^{(3)}$ modes respectively, as a function of magnetic field. The error bars are standard deviations of the fit values.

Here, the first order term, in the specific case of $J = J^{\perp}$ is responsible for the magnetophononic wave-mixing described in detail in the main text (Eq. 5.9 and Eq. 5.10).

The second order term, proportional to u_α^2, renormalizes the harmonic term in the lattice energy, resulting in spin-induced phonon frequency changes. Separating the in-plane and out-of-plane exchange couplings, denoted by J_μ and $J_\mu^{\perp}$, respectively, where $\mu = 1, 2, \ldots$ are the first- and second-nearest-neighbors and so on, and assuming small spin-induced energy shifts i. e. $\nu_\alpha + \nu_{\alpha 0} \approx 2\nu_{\alpha 0}$, the renormalized phonon frequency is given by

$$\nu_\alpha - \nu_{\alpha 0} = \frac{1}{4N\mu_\alpha \nu_{\alpha 0}} \left[\sum_\mu \frac{\partial^2 J_\mu}{\partial u_\alpha^2} \sum_i S_i \cdot S_{i+\mu} + \sum_\mu \frac{\partial^2 J_\mu^{\perp}}{\partial u_\alpha^2} \sum_i S_i \cdot S_{i+\mu^{\perp}} \right]. \tag{5.14}$$

The above expression shows the renormalization of the phonon frequency due to spin order along different directions, through the respective exchange couplings. Under a mean-field approximation, Eq. 5.14 simplifies to $\nu_\alpha - \nu_{\alpha 0} \propto \langle S^2 \rangle$.

Experimentally, we observe such a spin-induced phonon frequency renormalization in the $A_{1g}^{(1)}$ mode. The phonon frequencies are first extracted as a function of temperature, using the fitting procedure outlined in the Methods section of the main text. We then account for phonon-phonon interactions by fitting the temperature-dependent phonon frequencies to that of a (cubic) anharmonic phonon, given by $\omega(T) = \omega_0 + A\left(1 + \frac{2}{e^{\frac{\hbar\omega_0}{2k_BT}} - 1}\right)$, where ω is the phonon frequency renormalized by anharmonic (phonon-phonon) interactions, T is the temperature, ω_0 is the bare phonon frequency, and A is a mode-specific fitting constant.

Fig. 5.8 shows the temperature-dependent frequency of the $A_{1g}^{(1)}$ mode, with the black line showing a fit to the anharmonic phonon model. The plot shows a small but clear deviation from the fit below $T_N = 24$ K, indicating a spin-induced phonon frequency renormalization. In contrast, the temperature-dependent frequency of the $A_{1g}^{(3)}$ mode in Fig. S3 shows good agreement with the anharmonic phonon model down to the lowest temperatures, indicating that the $A_{1g}^{(3)}$ mode does not exhibit a

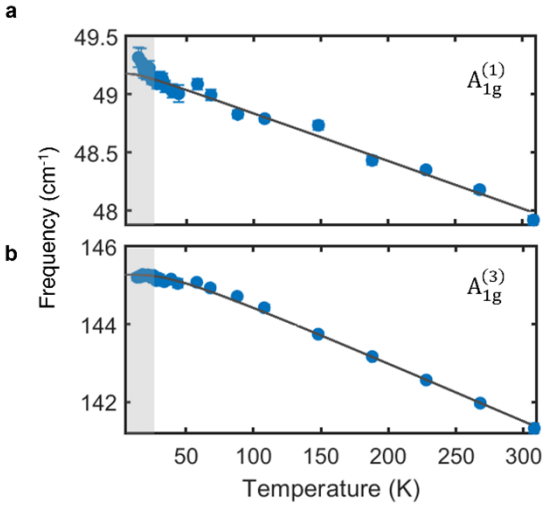

Figure 5.8: **Spin-induced phonon frequency renormalization.** Temperature-dependent frequency of the $A_{1g}^{(1)}$ phonon mode (top) and $A_{1g}^{(3)}$ phonon mode (bottom). The black lines are fits to the anharmonic phonon model described in the text.

significant spin-induced frequency renormalization.

Interestingly, we note that a previous study [119] on atomically thin flakes of $MnBi_2Te_4$ reported a negative spin-induced frequency renormalization of the $A_{1g}^{(1)}$ mode, contrary to the positive frequency renormalization observed in the bulk crystals used in our study. This difference may possibly be due to changes in the electronic and magnetic structure as a function of sample thickness in the 2D limit.

The strong magnetophononic coupling observed in the $A_{1g}^{(2)}$ mode in our magneto-Raman measurements suggests that it too might exhibit a significant spin-induced frequency shift. Unfortunately, the spectral overlap between the $A_{1g}^{(2)}$ and $E_g^{(3)}$ modes (see Fig. 5.5(a)) and strong $A_{1g}^{(2)}$ zone-boundary scattering intensity below T_N hinders a similar temperature-dependent frequency analysis for the $A_{1g}^{(2)}$ mode. None of the other observed Raman phonons exhibit a spin-induced frequency renormalization above the experimental uncertainty.

5.6.5 Supplementary Note 5: Resonant Raman effects

Resonant Raman effects may potentially give rise to temperature- and field-dependent artifacts in phonon peak intensities due to changes in the electronic band structure across phase transitions. In order to rule out such an explanation for the phenomena reported in Figs. 5.1 and 5.2, we investigate resonant Raman effects in $MnBi_2Te_4$ by measuring phonon spectra at different laser excitation energies. In Fig. 5.10, we show the Raman phonon spectra measured with laser excitation energies of 1.58 eV (785 nm), 1.96 eV (633 nm), and 2.71 eV (458 nm), at 297 K and zero magnetic field. Note that the 1.58 eV Raman spectrum is only shown down to 65 cm^{-1} due to the limitation of our low-frequency filters at this excitation wavelength.

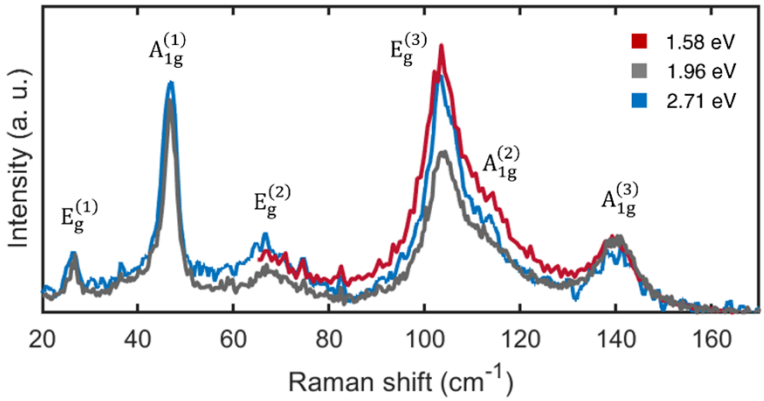

Figure 5.9: **Phonon spectra at different laser excitation energies.** Raman phonon spectra measured using 1.58 eV (785 nm), 1.96 eV (633 nm), and 2.71 eV (458 nm) laser excitation energies at 297 K and zero magnetic field. Spectra are normalized to the $A_{1g}^{(3)}$ peak intensity.

It is observed that phonon peak intensities indeed change as a function of the laser excitation energy, however, these changes occur across all the observed phonon modes, i. e. the three A_{1g} modes as well as the three E_g modes. It is clear that this result is independent of the choice of normalization. In contrast, the temperature- and field-dependent magnetophononic effects observed in our study are only in the

$A_{1g}^{(1)}$ and $A_{1g}^{(2)}$ modes, with negligible changes in the scattering intensities of other modes. Our observations reported in Figs. 5.1 and 5.2 are thus inconsistent with resonant Raman effects.

Furthermore, upon tracking the $A_{1g}^{(2)}$ mode across the PM $\rightarrow$ AFM transition at 24 K using the 1.58 eV (785 nm) laser excitation, it is found that the Raman scattering intensity exhibits quantitatively the same behavior (see Fig. 5.10) as with the 1.96 eV (633 nm) laser excitation (see Fig. 5.1c) – i. e. the $A_{1g}^{(2)}$ scattering intensity is enhanced by around 35% in the AFM phase. This is additional evidence that the observed phenomenon is inconsistent with resonant Raman effects, wherein different excitation energies would give rise to qualitatively different temperature-dependent intensity changes. It is instead consistent with an effect arising from the AFM order, as in our model of magnetophononic wavemixing.

It is useful to consider the exchange energies involved in various magnetic phase transitions in $MnBi_2Te_4$. The dominant in-plane nearest neighbor exchange coupling is 0.12 meV, whereas the interplanar exchange coupling is an order-of-magnitude weaker [120]. The temperature-driven PM $\rightarrow$ AFM transition is accompanied by significant magnetic energy changes due to the in-plane ordering of spins, and the large in-plane exchange coupling. On the other hand, the in-plane ordering remains unchanged in the out-of-plane magnetic field-driven AFM $\rightarrow$ FM transition, with only the interplanar magnetic order being modulated. The accompanying magnetic energy changes are thus an order of magnitude weaker than in the PM $\rightarrow$ AFM transition. Hence it is expected that the associated electronic structure changes as a function of out-of-plane magnetic field would also be correspondingly small, minimizing artifacts due to resonant Raman effects. This assertion is validated in our work, where we find that the scattering intensities of the E_g modes and the $A_{1g}^{(3)}$ mode are unchanged as a function of out-of-plane magnetic field within the experimental uncertainty, as outlined in Section S3, allowing us to identify magnetophononic zone-folding in the $A_{1g}^{(1)}$ and $A_{1g}^{(2)}$ peaks. Importantly, the phenomena observed in Figs.

5.1 and 5.2 are correlated not with magnetic order itself, but specifically with AFM order. The zone-boundary phonon intensity vanishes in the FM phase. In fact, as the results in Fig. 5.2 show, the zone-boundary intensity of the $A_{1g}^{(2)}$ phonon quantitatively tracks the AFM order in both the temperature- and magnetic field-dependent experiments.

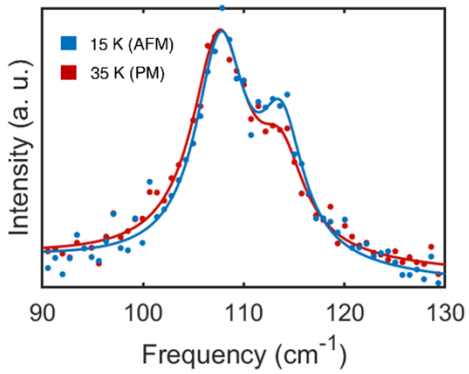

Figure 5.10: **Temperature-dependent intensity of $A_{1g}^{(2)}$ mode with 1.58 eV excitation.** Raman spectra measured at 15 K and 35 K using a 1.58 eV (785 nm) laser excitation. The dots are experimental datapoints, and the solid lines are fits as outlined in the Methods section.

Based on the above arguments, in order to rule out resonant Raman effects and isolate peak intensity changes due to magnetophononic coupling, it is essential to measure phonon scattering intensities as a function of both temperature and magnetic field, as in the present work.

5.6.6 Supplementary Note 6: Symmetry of anomalous scattering intensity

Magnetic ordering can potentially give rise to one-magnon and two-magnon resonances in Raman spectra. In order to eliminate the possibility that the anomalous

scattering intensities observed in our work (plotted in Figs. 5.1 and 5.2) are due to magnons, we carry out a polarization analysis.

Magnons, by virtue of breaking time-reversal symmetry necessarily have off-diagonal terms in the Raman tensor[121]. In $MnBi_2Te_4$, this is associated with E_g modes, as opposed to A_{1g} modes which are fully symmetric and have only diagonal components. The symmetry associated with Raman scattering intensity can be identified as A_{1g} or E_g using polarized Raman measurements, as in Section S1. Here, we focus on the $A_{1g}^{(2)}$ mode. In Fig. 5.11, we show Raman spectra obtained below and above the AFM ordering temperature $T_N = 24$ K, corresponding to parallel-polarization, which is sensitive to both A_{1g} and E_g modes, and cross-polarization, which is sensitive only to E_g modes. Our results clearly show that the anomalous scattering intensity overlapped with the $A_{1g}^{(2)}$ phonon in the AFM phase has an A_{1g} symmetry, since it is absent in the cross-polarized channel. This rules out the possibility that it is due to a magnon. It is instead consistent with our interpretation in terms of scattering intensity due to $A_{1g}^{(2)}$ zone-boundary phonons.

The above inference is also consistent with magnon dispersions measured using inelastic neutron scattering[120]. The dispersion shows that zone-center magnons are at around 1 meV ($\sim$8 cm^{-1}), whereas the highest energy zone-boundary magnons are at 3 meV ($\sim$25 cm^{-1}). The low energy of zone-center magnons rules out the possibility of one-magnon resonance interfering with phonon peaks. A two-magnon resonance may plausibly interfere with the $A_{1g}^{(2)}$ mode at 47 cm^{-1} but would be too low in energy to affect the $A_{1g}^{(2)}$ mode at 115 cm^{-1}, ruling it out as an explanation for the observed phenomena. Two-magnons are also typically associated with a broad continuum of excitations rather than a well-defined peak, a feature that we do not observe in our experiments.

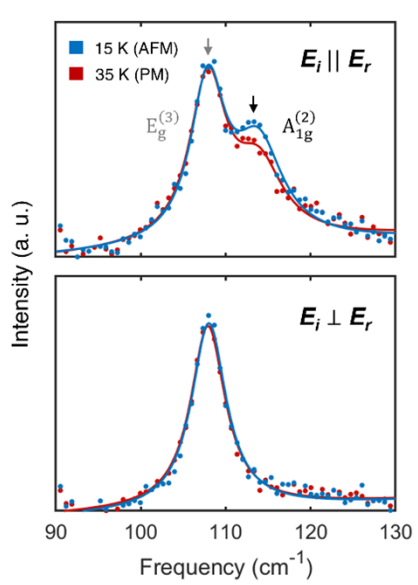

Figure 5.11: **Temperature- and polarization-dependent $A_{1g}^{(2)}$ scattering intensity.** Raman spectra measured at 15 K and 35 K with parallel- (top) and cross-polarization (bottom) of incident and reflected light. The dots are experimental datapoints, and solid lines are fits as outlined in the Methods section.

5.6.7 Supplementary Note 7: Pump-probe measurements – Fluence-dependence

The pump-probe measurements outlined in the main text show phonon excitation via a displacive mechanism, where the ultrafast excitation of carriers by the pump pulse shifts the quasiequilibrium ionic coordinates, generating coherent phonons. Here, the amplitude of coherent phonons is directly proportional to the pump-induced carrier density, i. e. the absorbed fluence. In this context, field-dependent optical conductivity changes may influence coherent phonon amplitudes, in addition to the magnetophononic coupling highlighted in the main text. We account for such magnetic-field dependent changes in absorbed fluence by normalizing the pump-probe measurements with respect to the pump-induced carrier density.

The carrier density can be tracked by the maximum amplitude of the transient reflectivity trace, which occurs at a time delay of ∼0.9 ps. In Fig. 5.4 of the main text, all the pump-probe traces are normalized with respect to this amplitude.

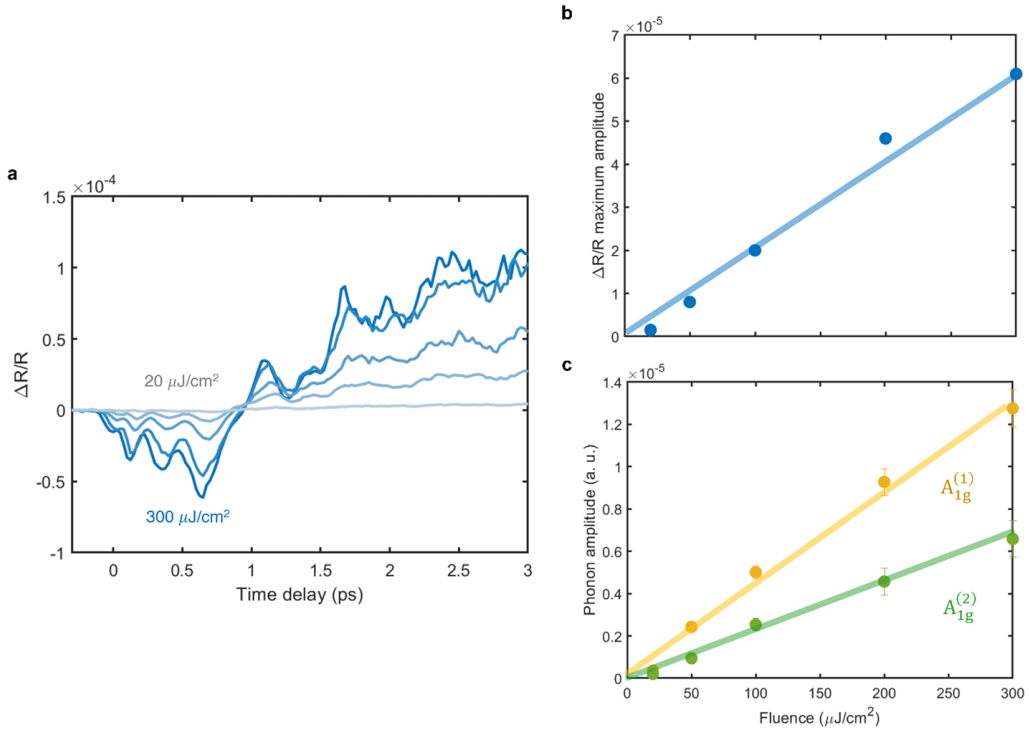

Figure 5.12: **Fluence-dependence of coherent phonons. a**, Transient reflectivity traces as a function of pump fluence from 20 to 300 $\mu J/cm^2$. **b**, Maximum subpicosecond amplitude of transient reflectivity as a function of pump fluence, which is a measure of the photoinduced carrier density. **c**, Amplitude of $A_{1g}^{(2)}$ and $A_{1g}^{(2)}$ coherent phonons as a function of pump fluence, extracted using the method outlined in the main text and Methods. The lines in **b** and **c** are linear fits.

We verify the validity of this approach by separately measuring the transient reflectivity and coherent phonon amplitudes as a function of pump fluence, shown in Fig. 5.12a. The fits in Fig. 5.12b and 5.12c, carried out as outlined in the Methods,

show that both the maximum transient reflectivity (which tracks the absorbed fluence and photoinduced carrier density) as well as the unnormalized coherent phonon amplitudes scale linearly with fluence, confirming that the maximum amplitude of the transient reflectivity trace indeed tracks the carrier density, validating the normalization procedure used in the main text.

Finally, we note that outside of magnetic-field dependent changes in absorbed fluence, there may potentially be additional magnetodielectric effects that change the electron-phonon interactions and thus the Raman susceptibility, which can affect coherent phonon generation. To lowest order, such changes may be phenomenologically described by a magnetodielectric effect of the form $\chi_e = \chi_e^{(0)} + \gamma M^2$, where χ_e is the electrical susceptibility, γ is magnetodielectric coefficient, and M is the net magnetization. Below, we explore possible changes to electron-phonon interaction due to such a magnetodielectric effect. In the interest of conceptual clarity, we consider a simple $M - H$ dependence $M = \chi_m H$, where χ_m is the magnetic susceptibility and H is the external magnetic field, the Raman susceptibility of a phonon (which determines the coherent phonon amplitude via a Raman-like displacive excitation) can then be written as $\frac{d\chi_e}{du} = \frac{d\chi_e^{(0)}}{du} + H^2 \left(2\gamma\chi_m \frac{d\chi_m}{du} + \chi_m^2 \frac{d\gamma}{du}\right)$. The expression in parenthesis determines the change in Raman susceptibility due to the magnetic field, where $\frac{d\chi_m}{du}$ and $\frac{d\gamma}{du}$ are the phonon modulation of the magnetic susceptibility and magnetodielectric coupling coefficient, respectively. Such a field-dependent change in the coherent phonon amplitude would then be a form of indirect magnetophononic coupling. Based on our current pump-probe experimental data, we cannot completely rule out that such indirect magnetophononic effects also have a contribution, in addition to the direct magnetophononic effects highlighted in our manuscript.

5.6.8 Supplementary Note 8: Debye-Waller effect in ultrafast electron diffraction

Optical pump-probe experiments are typically initiated by ultrafast optical (pump) pulses which generate photo-excited carriers (electrons and holes) – which, after thermalizing, decay through the generation of lattice (and spin) excitations. The lattice excitations result in a disordering of the lattice. Ultrafast electron diffraction is a direct probe of this pump-induced lattice disorder, through the transient Debye-Waller effect.

In general, the intensity of a Bragg reflection in an electron diffraction experiment is given by

$$I_0(Q) = \sum_j f_j(Q) \exp\left(-2\pi^2 B_j Q^2\right) \exp\left(-i2\pi Q \cdot r_j\right), \tag{5.15}$$

where the summation is over atoms in the unit cell (indexed by j), Q is the scattering wavevector, f_j is the atomic structure factor for electron diffraction for atom j, B_j is the isotropic Debye-Waller factor for atom j, and r_j is the position of atom j in the unit cell. The Debye-Waller factor is given by $B_j = \langle u_j^2 \rangle$, which is the root-mean-square displacement of atom j about its mean position. A representative static diffraction pattern from a ∼100 nm flake of $MnBi_2Te_4$ oriented along the (0 0 1) crystallographic direction is shown in Fig. 5.13a.

Pump-induced lattice disorder increases B_j, i. e. $B_j \rightarrow B_j + \Delta B_j$, thus generally resulting in a decrease in the transient Bragg reflection intensities. We can define an effective transient Debye-Waller factor ΔB_{eff} as follows –

$$\begin{aligned} I(Q) = &\sum_j f_j(Q) \exp\left(-2\pi^2 (B_j + \Delta B_j) Q^2\right) \exp\left(-i2\pi Q \cdot r_j = \right. \\ &\left. \exp\left(-2\pi^2 \Delta B_{eff} Q^2\right) I_0(Q). \right. \end{aligned} \tag{5.16}$$

The transient Bragg reflection intensity $I(Q)$ is thus a quantitative measure of the pump-induced lattice disorder, $\Delta B_{eff} = \Delta \langle u_{eff}^2 \rangle$. The Debye-Waller effect for a given family of Bragg reflections scales with Q, such that $\log\left(\frac{I}{I_0}\right) \propto -Q^2$.

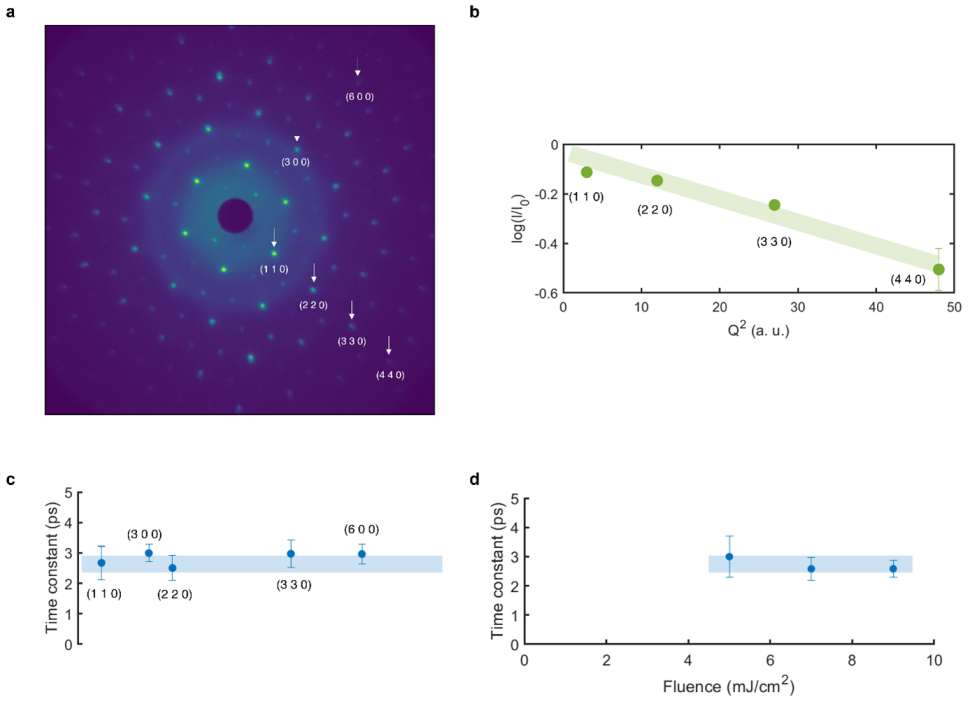

Figure 5.13: **Transient Debye-Waller effect. a,** Static electron diffraction image, with the (n n 0) family of peaks labeled. **b,** Transient Bragg reflection intensity obtained in the $t \to \infty$ limit from the exponential decay fit, plotted as a function of **Q**. The green line is a guide to the eye. **c,** The exponential decay constant of the transient intensity of various Bragg peaks. **d,** The exponential decay constant of the (2 2 0) peak as a function of pump fluence. Error bars are standard deviations of fit values. The blue lines are guides to the eye.

In Fig. 5.13b, we plot the transient intensity $\log\left(\frac{I}{I_0}\right)$ of the (n n 0) family of Bragg reflections at the $t \to \infty$ limit from the exponential decay fit (see Methods), as a function of Q^2. The linear dependence confirms that the observed evolution of transient Bragg intensities is due to a Debye-Waller effect via pump-induced lattice disorder.

The time constants of the transient intensities of various Bragg peaks, obtained from exponential decay fits, are shown in Fig. 5.13c. Within the experimental uncertainty, the time constant is uniform across different peaks.

In the main text, we use the transient Debye-Waller time constant from our UED measurements to establish the timescale of lattice thermalization. However, the optical pump-probe measurements reported in the main text use a much lower fluence, of 0.1 mJ/cm^2, as opposed to 7 mJ/cm^2 used in the UED measurements reported above. In this context, we report the thermalization time constants from our UED measurements as a function of fluence, in Fig. 5.13d. The time constants are largely unchanged from 5 to 9 mJ/cm^2, with a slight increase at lower fluences.

Such a behavior is consistent with increased phonon-phonon scattering at higher fluences[122]. It is expected then that the thermalization time constant at the low fluences used in our optical measurements, with their correspondingly lower phonon populations, would likely be even higher than that extracted from the UED measurements; i. e. the UED time constant sets a lower bound for the phonon thermalization time. This supports our assertion that phonon subsystem remains in a nonequilibrium state through the entire time delay range measured in our study.

5.7 Acknowledgements

This chapter, in full, is a reprint of the material as it appears in Nature Communications. Kim, Peter K.; Padmanabhan, Hari; Poore, Maxwell; Koocher, Nathan Z.; Stoica, Vladimir A.; Puggioni Danilo; Wang, Huaiyu (Hugo); Shen, Xiaozhe; Reid,

Alexander H.; Gu, Mingqiang; Wetherington, Maxwell; Lee, Seng Huat; Schaller, Richard D.; Mao, Zhiqiang; Lindenberg, Aaron M.; Wang, Xijie; Rondinelli, James M.; Averitt, Richard D.; and Gopalan, Venkatraman, Nature Communications, 2022. The dissertation author shared the role of the primary investigator and author of this paper with Hari Padmanabhan and Maxwell Poore.

Appendix A

OptiCool magnet

The experiments in this thesis used Quantum Design OptiCool optical cryostat. The OptiCool can reach magnetic fields of ±7 Tesla and temperatures from 1.7 K to 350 K. The sample and superconducting electromagnet is cooled via condense liquid Helium-4 which is recycled in a closed-cycle loop. For details on the theory of operation and regular maintenance, refer to the OptiCool user manual provided by Quantum Design. We have used the OptiCool for temperature and magnetic field control for pump-probe experiments in reflection in both the Kerr geometry (magnetic field applied parallel to the propagation direction of the light) and in the Voigt geometry (magnetic field applied perpendicular to the propagation direction of the light).

Sample preparation

The samples should have a mirror-like or polished surface for reflection measurements. In the case of the experiments on the single crystal β-Li_2IrO_3 and $MnBi_2Te_4$ samples described in this thesis, the samples surfaces were sufficiently flat without polishing. Though a well-polished surface would be preferrable, we were worried about compromising the integrity of the crystal by polishing as the samples were

small and fragile.

The samples are adhered to custom-machined copper sample mounts using either N grease or silver paint. Silver paint generally provides better thermal contact and transport, so it is best for low-temperature experiments. Silver paint was used for the experiments described in this thesis. It is important to consider the orientation of the sample when placing on the copper mounts. This includes but is not limited to ensuring the surface of the sample is parallel to that of the mount and choosing the correct orientation of the crystal axes with respect to the applied magnetic field, light propagation direction, and light polarization direction. For example, in the Voigt geometry, we used a small copper block to load orient our sample surface normal perpendicular to the magnetic field.

Once the sample is adhered to the copper mount, the mount is screwed onto the top of the top plate of the OptiCool Sample Pod. It is advisable to use apply a thin layer of N grease between the top plate of the OptiCool Sample Pod for maximal thermal contact. Be careful not to drop screws or loose magnetic parts into the magnet as this can be dangerous for the system, user, and samples when a strong magnetic field is turned on.

Aligning into OptiCool

I will assume that the pump and probe beamlines are prepared and ready to meet the samples for this following section. I will note some useful optics that can be helpful for aligning and optimizing a pump-probe signal in the OptiCool as is relevant, as well.

The general heuristic for setting up a pump-probe experiment into the OptiCool is as follows:

1. Roughly align the pump and probe beams into the 3-axis translation stage.

2. Use 3-axis translation stage to aim pump and probe beams onto sample on a

suitably reflective spot.

3. Use a camera at the sample location to check mode quality, beam diameters, and spatial overlap of the beams.

4. Pick off the probe beam after reflection from the sample and direct into the detection setup.

5. Use pump-probe signal to optimize pump-probe overlap.

Note that one may have to iterate between some of these steps as changes made to achieve one step may affect the other steps. The above is the general order of operations.

1. This step is summarized by ensuring that the pump and probe beams are parallel and well collimated as they arrive at the 3-axis translation stage. In the experiments in described in this thesis, the pump and probe beams were $\lesssim 2.5$ cm apart. The beams should be aligned parallel to one of the axes of 3-axis translation stage as there is a lens involved. Additionally, the pump and probe beams be incident on the lens roughly symmetrically to minimize spatial distortions in the beams.

2. The 3-axis translation stage is used to control where the pump and probe beams are incident at the sample location. Two of the three axes, which I will refer to as the x- and y-axes, are used to control within the plane of the sample location. The third axis, the z-axis, controls the position of the focal point along the direction normal to the sample surface. One should use a camera pointed at the sample to direct the beams onto the sample where the focal point is at the sample surface. Note this is only viable for wavelengths which the camera can pick up. Luckily, one is able to pick up slighly above 1040 nm with many commercial cameras. On the first pass, one can just roughly align the beams to the sample surface and then move onto step 3 where the beam is properly shaped. It is possible that the focal point cannot be translated to the sample surface – in this case, carefully translate the lens

in the 3-axis translation stage along the z-axis to bring the focal point to the correct location.

Once the beam has been properly shaped, one must find a reflective spot on the sample. This can be done with the pump beam blocked, but check that pump beam path is sensible once the reflective spot is found. To start, ensure that the z-axis is roughly at the correct location such that the focal point of the probe beam is at the sample surface. This will be fine adjusted later using the pump-probe signal, and the fine adjustment should not change the location the sample. If changing the z-axis significantly changes the position in the plane of the sample, (i) check the alignment into the 3-axis translation stage, or (ii) check that the 3-axis translation stage is properly aligned itself. Once the z-position is correct, place a lens tissue above the sample so that you can observe both the incident beam going to the sample and the reflected beam off of the sample. If the beam is near-normal incidence, the distance between these two spots should be small. In fact, one can roughly calculate the angle of incidence using the distance between these spots and the distance of the lens tissue to the sample. Next, translate in the x- and y-directions to look for a maximally reflective and clean spot. This takes may take some time for unpolished samples, but getting a clean spot is incredibly important for getting a high signal-to-noise ratio as it can minimize pump scatter and other imperfections in the pump-probe signal. One tip is that if the probe beam is indeed focused on the surface of the sample, the sample surface will be imaged onto the lens tissue.

3. This step involves checking the spatial characteristics of the pump and probe beam and ensuring overlap. It is generally difficult to place the camera directly at the sample location in the OptiCool, so instead, pick off the pump and probe beams together between the 3-axis translation stage and the sample and direct the beams onto a CCD camera. Importantly, make sure the pump and probe beams are sufficiently attenuated ($< 50\mu W$ for a beam that is a few tens of microns in diameter) so as to not burn the CCD. Once the beams are on the CCD, ensure that there is

pump-probe overlap near the focal point of the probe beam. If not, it is generally easiest to make a small adjustment the pump beam to achieve overlap. Note that due to the strong magnetic field applied in the experiment, the 3-axis translation stage is somewhat far away from the actual sample, meaning that we must use a long focal length lens. This limits the minimum beam diameter that can be easily achieved. Nominally, we usually work with a minimum beam diameter of $\sim 50\mu$m for the probe beam. One can also use this setup to measure the beam diameter. If this step is done without including the OptiCool windows, note that the overlap and beam diameters will be slightly off compared to actual experimental conditions. Practically speaking, this difference is small as the windows are each 5 mm thick for the top port and 4 mm thick for the side ports.

4. The reflected probe beam should be picked off and directed to the detection scheme. As the detection scheme is dependent on the experiment of interest, this section is left as an exercise for the reader.

5. Once the pump-probe signal is found, one can use it to optimize the overlap under proper experimental conditions. Once the signal is found, bring the setup as close to experimental conditions as possible, including sealing the OptiCool, evacuating the chamber, and cooling down the sample. If it is expected that there are still significant adjustments to be made, this step can initially be done roughly at atmospheric conditions. Once experimental conditions are met, adjust the time-delay to sit at the peak of the pump-probe signal and adjust the z-axis on the 3-axis translation stage to maximize the absolute value of the signal. This will bring the optimized pump-probe overlap found in step 3 to the sample surface. Once this is optimized, as a last final step before experiments begin, very carefully and very slightly adjust the propagation of the pump beam before the 3-axis translation stage and optimize the pump-probe signal. This step accounts for slight changes in the propagation in the presence of a window. Once this is completed, this should not be readjusted throughout the experiment as this can introduce significant random error.

Appendix B

Custom OPA

This section describes the construction and alignment of a homemade collinear optical parametric amplifier. The design was inspired by [123]. This OPA generates light with wavelengths tunable from 850 nm - 950 nm. The major motivation is to use this OPA output to generate carrier envelope phase (CEP) stabilized mid-IR pulses via a subsequent stage of difference frequency generation. This OPA was designed and constructed with equal contributions from Maxwell Poore and with the guidance of Peter Kissin.

Refer to Fig. B.1 for a schematic of the OPA.

Stage 1 OPA

The first stage of optical parametric amplification (Stage 1 OPA) starts from the polarizing beam splitter (PBS_1) to the recombination in the type-II phase-matched BBO crystal BBO_2.

The input 1040 nm beam is expanded by Keplerian telescope, labeled T_1, to a beam diameter of $\sim$ 1.5 mm, and has a linear polarization that is controlled by the $\lambda/2$ wave-plate labeled WP_1. The input 1040 nm beam is a pulse train generated by the Spirit One 1040-8 at a repetition rate of 209,000 Hz and an average total power

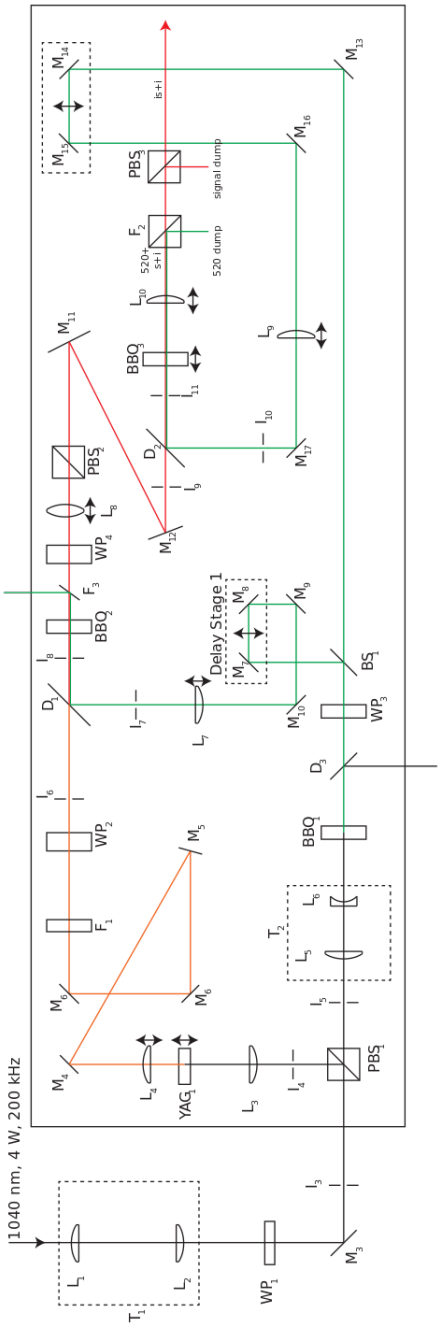

Figure B.1: Custom OPA schematics

of ∼7.6 W. The pulse duration is ∼300 fs and the spectrum of the pulse is centered about 1040 nm with a FWHM of ∼5 nm. Thus, the total energy per pulse is ∼36 μJ.

Using a polarizing beam splitter, the pulse energy of the 1040 nm beam is split into two paths: (i) the white light path serving as the seed pulses for the first stage of optical parametric amplification, and (ii) the 520 nm pump path serving as the pump beam for the first stage (and second stage) of optical parametric amplification. Note pulse the energy in path (ii) is split once again after the pulses are frequency double via second harmonic generation (SHG) so that this energy pumps both the first and second stages of OPA.

Stage 1 OPA: White light generation

From the beam splitter, the white light path (path (i)) receives vertically polarized 1040 nm pulses with pulse energies of ∼1.2 μJ, a peak power of 4MW, and a total average power of 250 mW (209,000 Hz). These pulses are then focused into a 5 mm thick YAG crystal at normal incidence, generating spectrally broadband near-infrared pulses via a nonlinear process that I will refer to as "white light generation". A general overview of white light generation in various nonlinear crystals can be found in [124]. YAG, or $Y_3Al_5O_{12}$, is a cubic garnet that is insulating with a calculated bandgap of ∼5 eV [125]. Though not totally understood by 2007, it was widely assumed that several nonlinear processes lead to white light generation including (i) self-phase modulation, (ii) optical “shockwave” formation due to self-steepening, and (iii) self-focusing [126].

The ultimate goal is to generate a stable pulse train of intense, spectrally broad and spectrally smooth white light pulses. This is achieved by focusing the 1040 nm beam just above the threshold for self-focusing the 1040 nm beam in the YAG. The theoretical details behind white light generation in YAG crystals will not be covered in this text. A more thorough and general treatment of white light generation can

be found in Refs [126, 124, 127].

The main experimental parameters we considered were the numerical aperture (NA) of the 1040 nm pump beam into the YAG, the peak 1040 nm pump intensity incident on the YAG, and the filamentation length in the YAG (tuned by varying the depth of the focal point in the YAG). The values for these parameters corresponding to the numbers listed above are NA ≈ 0.015 and a peak intensity $I_{max} \approx 88$ GW/cm^2 for optimal operating conditions.

The 1040 nm pump beam is focused onto the YAG using a converging AR-coated plano-concave lens with a focal length of 50 mm (L_3). We tested the effects of varying the focal length of lens L3 using lenses of focal lengths f = 25, 75, 100, and 150 mm. We were able to generate stable white light using the 25 mm and 75 mm focal length lenses, but none of the others. For both the 25 mm and 75 mm lenses, the resultant spectra had artifacts of self-phase modulation resulting in frequency-comb-like spectra, and/or were not spectrally broad. The position of the YAG crystal along the axis of beam propagation was varied with respect to the focal point for each set of focusing and pump power conditions; the resultant stabilities and spectra were highly dependent on the YAG's position with respect to the focal point. An experimental consideration to note is that, under certain conditions, the onset of white light generation required a short time for the YAG crystal to thermalize – usually on the order of 30 seconds. Ultimately, these conditions were favorable in generating the most efficient and stable white light pulses. When testing the various focusing and incident power conditions, we generally used the maximum intensity below the damage threshold of the YAG crystal (usually about 300 MW or $\sim$63 GW/cm^2) to optimize the white light spectral profile and stability; once a desirable spectrum and stability was acquired, we subsequently reduced the pump power to the minimum threshold to achieve stable white light. In the context of this OPA, the main spectral region of interest is from 800 nm to 1040 nm as these wavelengths correspond to the signal seed for the OPA within the bandwidth of

the BBO. The spectrum of the white light beam was characterized through a fiber-coupled OceanView spectrometer.

The white light generated in the YAG crystal is output with a high divergence – the beam diameter 25 mm after the posterior face of the YAG was about 20 mm as determined by eye. I assume here that the divergence of the NIR white light photons is approximately the same as the divergence of the visible photons ($\sim$580$\pm$60 nm – appears as a smooth green-yellow-orange spot). The white light from the YAG is then loosely focused by a 25 mm AR-coated plano-concave lens mounted on a translation stage (L_4) to a focal point located at the BBO crystal for optical parametric amplification. The design choice of using a single lens after the YAG to loosely focus the diverging white light was made to minimize the path length through dispersive optics of the white light pulses; an improvement can be made on this system by replacing all transmissive focusing optics in the white light path with curved focusing mirrors (ideally parabolic, though spherical mirrors may be sufficient).

After lens L_4, the white light pulse is steered through a path in free space (air) to match the path length of the 520 nm arm of Stage 1 OPA (mirrors M_4 – M_7). Note that the mirrors used to steer the white light pulses were broadband mirrors (specifically Ag mirrors) to minimize spectral loss or chromatic dispersion. A notch filter F1 centered at 1040 nm and a $\lambda/2$ wave-plate WP_2 was placed in the white light path before the recombination of the white light pulses with the 520 nm pump pulses in the dichroic mirror D_1. Because the white light pulses are collinear with the 1040 nm pump pulses, the filter F_1 was necessary to remove the 1040 nm light from the beam path. Though I am not sure if this is entirely necessary, the 1040 nm photons serve no purpose in the OPA process, and the 1040 nm photons may also undergo SHG in BBO_2 as well. The $\lambda/2$ wave-plate WP2 was used to adjust the angle of linear polarization of the white light seed pulses so that phase matching was achieved in BBO_2. Though the authors of this text are not entirely sure of

mechanisms behind the polarization rotation of spectral components during white light generation, [127] demonstrated that there are spectral components after white light generation orthogonal to the incident pump polarization. The $\lambda/2$ wave-plate is used as a tuning parameter to maximize the efficiency of OPA in BBO_2.

Stage 1 OPA: 520 nm pump path

From the beam splitter PBS1, the 520 nm pump path (path (ii)) receives horizontally polarized 1040 nm pulses with the remainder of the input 1040 nm power.

In retrospect, after review of the properties of the polarizing beam splitter (Thorlabs PBS123), it would be favorable to reflect the majority of the power as the reflectivity is >99.5% whereas the transmissivity is >90%. Furthermore, the extinction coefficient for transmission is much higher than the extinction coefficient for reflection. Recalling that s-polarized light is reflected and p-polarized light is transmitted, the extinction coefficients imply that the fraction of s-polarized photons transmitted is much smaller than the fraction of p-polarized photons reflected – thus it seems favorable to have the higher-intensity branch be reflected. Unfortunately, the current geometry is set up to transmit the higher-intensity branch (the 520 nm pump path), and the remainder of the text will assume this geometry.

After PBS1, the 1040 nm beam is loosely focused with a Galilean telescope T_2 (f=150 mm, f=-100 mm; M=1.5) onto the BBO crystal (BBO_1). This results in frequency doubled 520 nm pulses with a total power of 3.5 W at 520 nm (measured using 1040 nm filter + power meter). This corresponds to a quantum efficiency of about QE=$\frac{2 \cdot n_{out}^{520}}{n_{in}^{1040}} \approx 47\%$, where $n_{in(out)}^{\lambda}$ is the number of photons at wavelength λ going into (out of) the BBO.

Once the 520 nm pulses are generated, the 1040 nm photons are filtered out by dichroic mirror D_3. Directly out of the type-I BBO, the 520 nm pulses have a vertical polarization, orthogonal to the 1040 nm parent pulses. The 520 nm pump pulses must be polarized perpendicular to the axis of rotation (ie. perpendicular to

the ordinary axis) used to achieve the phase-matching angle, and it is practically favorable to have the angle of rotation lie in the vertical direction. Thus, due to these geometric constraints, we rotate the polarization of the 520 nm using the $\lambda/2$ wave-plate WP_3. The 520 nm beam is then split into two equivalent pulse trains with 1.75 W of total power each by a 50:50 beam splitter (BS_1). This corresponds to 8.38 μJ per pulse. Stage 1 OPA utilizes the reflected beam from BS1 to pump the OPA at BBO_2, and Stage 2 OPA utilizes the transmitted beam to pump the OPA at BBO_3. The 520 nm pump beam is then steered through a retroreflective time-delay stage (Delay Stage 1) that is used to tune the temporal overlap of the seed pulses and the pump pulses. Mirrors M_8 – M_11 are dielectric mirrors that are highly reflective at 520 nm.

Stage 1 OPA: Recombination and OPA

After Delay Stage 1, the pump beam is directed through lens L7, set on a translation stage, focusing the beam into BBO_2. The pump pulses are recombined with the seed pulses at the dichroic mirror D_1. The pump-seed overlap is optimized by ensuring that the two beams have the same focal point, identical numerical apertures, and equal spot sizes at the focal point. This maximizes the mode volume for the nonlinear interactions and ensures phase-matching. In practice, total spatial overlap is difficult to achieve. The current setup tunes these parameters by translating the lenses L_4 and L_7 independently. The beams coming out of lenses L_4 and L_7 have different focal lengths, spectral profiles, incident beam diameters, and incident divergences; this results in the two arms having different rates of change in numerical aperture and spot size with respect to the focal point position. Ideally, we need an additional degree of freedom to ensure that all three conditions are met (identical focal point positions, numerical apertures, and spot sizes), but we can get relatively decent OPA efficiency using this current setup.

Note that we are using type-II phase-matched collinear optical parametric am-

plification in uniaxial BBO. We are pumping with 520 nm photons and seeding the amplification process using the signal-like (i.e. higher energy than degeneracy) photons in the white light pulses. In type-II collinear OPA, the seed/signal beam is polarized along the ordinary axis, and the pump beam is polarized perpendicular to the ordinary axis and thus lives on the plane spanned by the two extraordinary axes.

Bibliography

[1] J. Zhang and R.D. Averitt. Dynamics and Control in Complex Transition Metal Oxides. *Annual Review of Materials Research*, 44(Volume 44, 2014):19–43, 2014.

[2] J Ferre and G A Gehring. Linear optical birefringence of magnetic crystals. *Reports on Progress in Physics*, 47(5):513–611, May 1984.

[3] Akhlesh Lakhtakia and Ricardo A. Depine. On Onsager relations and linear electromagnetic materials. *AEU - International Journal of Electronics and Communications*, 59(2):101–104, May 2005.

[4] Katsuaki Sato and Takayuki Ishibashi. Fundamentals of Magneto-Optical Spectroscopy. *Frontiers in Physics*, 10, October 2022.

[5] Rohit P Prasankumar and Antoinette J Taylor. *Optical techniques for solid-state materials characterization*. CRC press, 2016.

[6] Anatoliĭ Zvezdin. *Modern magnetooptics and magnetooptical materials*.

[7] R Clark Jones. A new calculus for the treatment of optical systemsi. description and discussion of the calculus. *Josa*, 31(7):488–493, 1941.

[8] Kristina Wilson. Guide to NOPAs.

[9] Robert W Boyd, Alexander L Gaeta, and Enno Giese. Nonlinear optics. In *Springer Handbook of Atomic, Molecular, and Optical Physics*, pages 1097–1110. Springer, 2008.

[10] Giulio Cerullo and Sandro De Silvestri. Ultrafast optical parametric amplifiers. *Review of scientific instruments*, 74(1):1–18, 2003.

[11] William Witczak-Krempa, Gang Chen, Yong Baek Kim, and Leon Balents. Correlated quantum phenomena in the strong spin-orbit regime. *Annu. Rev. Condens. Matter Phys.*, 5(1):57–82, 2014.

[12] G. Jackeli and G. Khaliullin. Mott Insulators in the Strong Spin-Orbit Coupling Limit: From Heisenberg to a Quantum Compass and Kitaev Models. *Physical Review Letters*, 102(1), January 2009.

[13] Jeffrey G Rau, Eric Kin-Ho Lee, and Hae-Young Kee. Spin-orbit physics giving rise to novel phases in correlated systems: Iridates and related materials. *Annual Review of Condensed Matter Physics*, 7(1):195–221, 2016.

[14] John Hubbard. Electron correlations in narrow energy bands. *Proceedings of the Royal Society of London. Series A. Mathematical and Physical Sciences*, 276(1365):238–257, 1963.

[15] Ramon Alejandro Ruiz-Ramos. *Study of Three-Dimensional Kitaev Honeycomb Materials β, γ—Li2IrO3*. PhD thesis, University of California, Berkeley, 2018.

[16] Stephen M Winter, Alexander A Tsirlin, Maria Daghofer, Jeroen van den Brink, Yogesh Singh, Philipp Gegenwart, and Roser Valentí. Models and materials for generalized Kitaev magnetism. *Journal of Physics: Condensed Matter*, 29(49):493002, 2017.

[17] Alberto De la Torre. *Spectroscopic studies of layered iridium oxides*. PhD thesis, Dec 2015.

[18] Cyril Martins, Markus Aichhorn, and Silke Biermann. Coulomb correlations in 4d and 5d oxides from first principles—or how spin–orbit materials choose their effective orbital degeneracies. *Journal of Physics: Condensed Matter*, 29(26):263001, 2017.

[19] Giniyat Khaliullin. Orbital order and fluctuations in Mott insulators. *Progress of Theoretical Physics Supplement*, 160:155–202, 2005.

[20] Alexei Kitaev. Anyons in an exactly solved model and beyond. *Annals of Physics*, 321(1):2–111, January 2006.

[21] Alejandro Ruiz, Vikram Nagarajan, Mayia Vranas, Gilbert Lopez, Gregory T. McCandless, Itamar Kimchi, Julia Y. Chan, Nicholas P. Breznay, Alex Frañó, Benjamin A. Frandsen, and James G. Analytis. High-temperature magnetic

anomaly in the Kitaev hyperhoneycomb compound β-Li_2IrO_3. *Physical Review B*, 101(7), February 2020.

[22] Alejandro Ruiz, Alex Frano, Nicholas P. Breznay, Itamar Kimchi, Toni Helm, Iain Oswald, Julia Y. Chan, R. J. Birgeneau, Zahirul Islam, and James G. Analytis. Correlated states in β-Li_2IrO_3 driven by applied magnetic fields. *Nature Communications*, 8(1), October 2017.

[23] K. A. Modic, Tess E. Smidt, Itamar Kimchi, Nicholas P. Breznay, Alun Biffin, Sungkyun Choi, Roger D. Johnson, Radu Coldea, Pilanda Watkins-Curry, Gregory T. McCandless, Julia Y. Chan, Felipe Gandara, Z. Islam, Ashvin Vishwanath, Arkady Shekhter, Ross D. McDonald, and James G. Analytis. Realization of a three-dimensional spin–anisotropic harmonic honeycomb iridate. *Nature Communications*, 5(1), June 2014.

[24] A. Biffin, R. D. Johnson, Sungkyun Choi, F. Freund, S. Manni, A. Bombardi, P. Manuel, P. Gegenwart, and R. Coldea. Unconventional magnetic order on the hyperhoneycomb Kitaev lattice in β-Li_2IrO_3: Full solution via magnetic resonant x-ray diffraction. *Physical Review B*, 90(20), November 2014.

[25] A. Biffin, R. D. Johnson, I. Kimchi, R. Morris, A. Bombardi, J. G. Analytis, A. Vishwanath, and R. Coldea. Noncoplanar and Counterrotating Incommensurate Magnetic Order Stabilized by Kitaev Interactions in γ-Li_2IrO_3. *Physical Review Letters*, 113(19), November 2014.

[26] M. Majumder, F. Freund, T. Dey, M. Prinz-Zwick, N. Büttgen, Y. Skourski, A. Jesche, A. A. Tsirlin, and P. Gegenwart. Anisotropic temperature-field phase diagram of single crystalline β-Li_2IrO_3: Magnetization, specific heat, and 7Li NMR study. *Physical Review Materials*, 3(7), July 2019.

[27] M Majumder, M Prinz-Zwick, Stephan Reschke, A Zubtsovskii, T Dey, F Freund, Norbert Büttgen, Anton Jesche, István Kézsmárki, Alexander A Tsirlin, et al. Field evolution of low-energy excitations in the hyperhoneycomb magnet β-Li 2 IrO 3. *Physical Review B*, 101(21):214417, 2020.

[28] Alejandro Ruiz, Nicholas P. Breznay, Mengqun Li, Ioannis Rousochatzakis, Anthony Allen, Isaac Zinda, Vikram Nagarajan, Gilbert Lopez, Zahirul Islam, Mary H. Upton, Jungho Kim, Ayman H. Said, Xian-Rong Huang, Thomas Gog, Diego Casa, Robert J. Birgeneau, Jake D. Koralek, James G. Analytis, Natalia B. Perkins, and Alex Frano. Magnon-spinon dichotomy in the Kitaev hyperhoneycomb β-Li_2IrO_3. *Physical Review B*, 103(18), May 2021.

[29] A. Glamazda, P. Lemmens, S. H. Do, Y. S. Choi, and K. Y. Choi. Raman spectroscopic signature of fractionalized excitations in the harmonic-honeycomb iridates β- and γ-Li_2IrO_3. *Nature Communications*, 7(1), July 2016.

[30] Ying Li, Stephen M. Winter, Harald O. Jeschke, and Roser Valentí. Electronic excitations in γLi_2IrO_3. *Physical Review B*, 95(4), January 2017.

[31] Ying Li, Kateryna Foyevtsova, Harald O Jeschke, and Roser Valentí. Analysis of the optical conductivity for A 2 IrO 3 (A= Na, Li) from first principles. *Physical Review B*, 91(16):161101, 2015.

[32] V Hermann, Jihaan Ebad-Allah, F Freund, Anton Jesche, Alexander A Tsirlin, Philipp Gegenwart, and Christine A Kuntscher. Optical signature of the pressure-induced dimerization in the honeycomb iridate α-Li 2 IrO 3. *Physical Review B*, 99(23):235116, 2019.

[33] J. P. Hinton, S. Patankar, E. Thewalt, A. Ruiz, G. Lopez, N. Breznay, A. Vishwanath, J. Analytis, J. Orenstein, J. D. Koralek, and I. Kimchi. Photoexcited states of the harmonic honeycomb iridate γ-Li_2IrO_3. *Physical Review B*, 92(11), September 2015.

[34] Lucile Savary and Leon Balents. Quantum spin liquids: a review. *Reports on Progress in Physics*, 80(1), 2017.

[35] Saptarshi Mandal and Naveen Surendran. Exactly solvable Kitaev model in three dimensions. *Physical Review B*, 79(2), January 2009.

[36] Simon Trebst and Ciarán Hickey. Kitaev materials. *Physics Reports*, 950:1–37, 2022.

[37] M. Hermanns, I. Kimchi, and J. Knolle. Physics of the Kitaev Model: Fractionalization, Dynamic Correlations, and Material Connections. *Annual Review of Condensed Matter Physics*, 9(1):17–33, March 2018.

[38] Ioannis Rousochatzakis and Natalia B. Perkins. Magnetic field induced evolution of intertwined orders in the Kitaev magnet β-Li_2IrO_3. *Physical Review B*, 97(17), May 2018.

[39] H. Gretarsson, J. P. Clancy, X. Liu, J. P. Hill, Emil Bozin, Yogesh Singh, S. Manni, P. Gegenwart, Jungho Kim, A. H. Said, D. Casa, T. Gog, M. H. Upton, Heung-Sik Kim, J. Yu, Vamshi M. Katukuri, L. Hozoi, Jeroen van den

Brink, and Young-June Kim. Crystal-Field Splitting and Correlation Effect on the Electronic Structure of A_2IrO_3. *Physical Review Letters*, 110(7), February 2013.

[40] Beom Hyun Kim, Tomonori Shirakawa, and Seiji Yunoki. From a Quasimolecular Band Insulator to a Relativistic Mott Insulator in t_{2g}^5 Systems with a Honeycomb Lattice Structure. *Physical Review Letters*, 117(18), October 2016.

[41] T. Takayama, A. Kato, R. Dinnebier, J. Nuss, H. Kono, L. S. I. Veiga, G. Fabbris, D. Haskel, and H. Takagi. Hyperhoneycomb Iridate β-Li_2IrO_3 as a Platform for Kitaev Magnetism. *Physical Review Letters*, 114(7), February 2015.

[42] Samuel Ducatman, Ioannis Rousochatzakis, and Natalia B. Perkins. Magnetic structure and excitation spectrum of the hyperhoneycomb Kitaev magnet β-Li_2IrO_3. *Physical Review B*, 97(12), March 2018.

[43] Mengqun Li, Ioannis Rousochatzakis, and Natalia B. Perkins. Unconventional magnetic field response of the hyperhoneycomb Kitaev magnet β-Li_2IrO_3. *Physical Review Research*, 2(1), January 2020.

[44] Wonjune Choi, Tomonari Mizoguchi, and Yong Baek Kim. Nonsymmorphic-Symmetry-Protected Topological Magnons in Three-Dimensional Kitaev Materials. *Physical Review Letters*, 123(22), November 2019.

[45] K. A. Modic, B. J. Ramshaw, J. B. Betts, Nicholas P. Breznay, James G. Analytis, Ross D. McDonald, and Arkady Shekhter. Robust spin correlations at high magnetic fields in the harmonic honeycomb iridates. *Nature Communications*, 8(1), August 2017.

[46] Yang Yang, Yiping Wang, Ioannis Rousochatzakis, Alejandro Ruiz, James G. Analytis, Kenneth S. Burch, and Natalia B. Perkins. Signatures of non-Loudon-Fleury Raman scattering in the Kitaev magnet β-Li_2IrO_3. *Physical Review B*, 105(24), June 2022.

[47] A. Revelli, M. Moretti Sala, G. Monaco, C. Hickey, P. Becker, F. Freund, A. Jesche, P. Gegenwart, T. Eschmann, F. L. Buessen, S. Trebst, P. H. M. van Loosdrecht, J. van den Brink, and M. Grüninger. Fingerprints of Kitaev physics in the magnetic excitations of honeycomb iridates. *Physical Review Research*, 2(4), October 2020.

[48] Jungho Kim, Jiří Chaloupka, Yogesh Singh, J. W. Kim, B. J. Kim, D. Casa, A. Said, X. Huang, and T. Gog. Dynamic Spin Correlations in the Honeycomb Lattice Na_2IrO_3 Measured by Resonant Inelastic x-Ray Scattering. *Physical Review X*, 10(2), May 2020.

[49] Thomas Halloran, Yishu Wang, Mengqun Li, Ioannis Rousochatzakis, Prashant Chauhan, M. B. Stone, Tomohiro Takayama, Hidenori Takagi, N. P. Armitage, Natalia B. Perkins, and Collin Broholm. Magnetic excitations and interactions in the Kitaev hyperhoneycomb iridate β-Li_2IrO_3. *Physical Review B*, 106(6), August 2022.

[50] J. Demsar, R. Hudej, J. Karpinski, V. V. Kabanov, and D. Mihailovic. Quasiparticle dynamics and gap structure in $HgBa_2Ca_2Cu_3O_{8+\delta}$ investigated with femtosecond spectroscopy. *Physical Review B*, 63(5), January 2001.

[51] title = Single-quasiparticle stability and quasiparticle-pair decay in $YBa_2Cu_3O_{6.5}$ N. Gedik and P. Blake and R. C. Spitzer and J. Orenstein and Ruixing Liang and D. A. Bonn and W. N. Hardy. *Physical Review B*, 70(1), July 2004.

[52] J. P. Hinton, J. D. Koralek, G. Yu, E. M. Motoyama, Y. M. Lu, A. Vishwanath, M. Greven, and J. Orenstein. Time-Resolved Optical Reflectivity of the Electron-Doped $Nd_{2x}Ce_xCuO_{4+\delta}$ Cuprate Superconductor: Evidence for an Interplay between Competing Orders. *Physical Review Letters*, 110(21), May 2013.

[53] Darius H. Torchinsky, G. F. Chen, J. L. Luo, N. L. Wang, and Nuh Gedik. Band-dependent Quasiparticle Dynamics in Single Crystals of the $Ba_{0.6}K_{0.4}Fe_2As_2$ Superconductor Revealed by Pump-Probe Spectroscopy. *Physical Review Letters*, 105(2), July 2010.

[54] J. Demsar, R. D. Averitt, A. J. Taylor, V. V. Kabanov, W. N. Kang, H. J. Kim, E. M. Choi, and S. I. Lee. Pair-Breaking and Superconducting State Recovery Dynamics in MgB_2. *Physical Review Letters*, 91(26), December 2003.

[55] J. Demsar, K. Biljaković, and D. Mihailovic. Single Particle and Collective Excitations in the One-Dimensional Charge Density Wave Solid $K_{0.3}MoO_3$ Probed in Real Time by Femtosecond Spectroscopy. *Physical Review Letters*, 83(4):800–803, July 1999.

[56] Elbert E. M. Chia, Jian-Xin Zhu, H. J. Lee, Namjung Hur, N. O. Moreno, E. D. Bauer, T. Durakiewicz, R. D. Averitt, J. L. Sarrao, and A. J. Taylor. Quasiparticle relaxation across the spin-density-wave gap in the itinerant antiferromagnet $UNiGa_5$. *Physical Review B*, 74(14), October 2006.

[57] Peter Kissin, Sheng Ran, Dylan Lovinger, Verner K. Thorsmølle, Noravee Kanchanavatee, Kevin Huang, M. Brian Maple, and Richard D. Averitt. Quasiparticle relaxation dynamics in $URu_{2-x}Fe_xSi_2$ single crystals. *Physical Review B*, 99(16), April 2019.

[58] H. Chu, L. Zhao, A. de la Torre, T. Hogan, S. D. Wilson, and D. Hsieh. A charge density wave-like instability in a doped spin–orbit-assisted weak Mott insulator. *Nature Materials*, 16(2):200–203, January 2017.

[59] Yakun Yuan, Peter Kissin, Danilo Puggioni, Kevin Cremin, Shiming Lei, Yu Wang, Zhiqiang Mao, James M. Rondinelli, Richard D. Averitt, and Venkatraman Gopalan. Ultrafast quasiparticle dynamics in the correlated semimetal $Ca_3RU_2O_7$. *Physical Review B*, 99(15), April 2019.

[60] Martin Dressel and George Grüner. *Electrodynamics of Solids: Optical Properties of Electrons in Matter*. Cambridge University Press, January 2002.

[61] Zhanybek Alpichshev, Fahad Mahmood, Gang Cao, and Nuh Gedik. Confinement-Deconfinement Transition as an Indication of Spin-Liquid-Type Behavior in Na_2IrO_3. *Physical Review Letters*, 114(1), January 2015.

[62] Zhanybek Alpichshev, Edbert J. Sie, Fahad Mahmood, Gang Cao, and Nuh Gedik. Origin of the exciton mass in the frustrated Mott insulator Na_2IrO_3. *Physical Review B*, 96(23), December 2017.

[63] Zala Lenarčič and Peter Prelovšek. Ultrafast Charge Recombination in a Photoexcited Mott-Hubbard Insulator. *Physical Review Letters*, 111(1), July 2013.

[64] Julian Wagner, Anuja Sahasrabudhe, Rolf Versteeg, Zhe Wang, Vladimir Tsurkan, Alois Loidl, Hamoon Hedayat, and Paul H. M. van Loosdrecht. Nonequilibrium dynamics of -RuClsub3/sub – a time-resolved magneto-optical spectroscopy study. *Faraday Discussions*, 237:237–258, 2022.

[65] Dan Nevola, Alexander Bataller, Ankit Kumar, Samanvitha Sridhar, Jordan Frick, Shaun O'Donnell, Harald Ade, Paul A. Maggard, Alexander F. Kemper, Kenan Gundogdu, and Daniel B. Dougherty. Timescales of excited state

relaxation in α-$RuCl_3$ observed by time-resolved two-photon photoemission spectroscopy. *Physical Review B*, 103(24), June 2021.

[66] N. Nembrini, S. Peli, F. Banfi, G. Ferrini, Yogesh Singh, P. Gegenwart, R. Comin, K. Foyevtsova, A. Damascelli, A. Avella, and C. Giannetti. Tracking local magnetic dynamics via high-energy charge excitations in a relativistic Mott insulator. *Physical Review B*, 94(20), November 2016.

[67] Haochen Zhang, Subin Kim, Young-June Kim, Hae-Young Kee, and Luyi Yang. Ultrafast dynamics of fractional particles in α-$RuCl_3$, 2019.

[68] D.N. Basov, R.D. Averitt, D. Marel, M. Dressel, and K. Haule. Electrodynamics of correlated electron materials. *Rev. Mod. Phys*, 83:471–541, 2011.

[69] S.-W. Cheong and M. Mostovoy. Multiferroics: a magnetic twist for ferroelectricity. *Nat. Mater*, 6:13–20, 2007.

[70] Y. Tokura, K. Yasuda, and A. Tsukazaki. Magnetic topological insulators. *Nat. Rev. Phys*, 1:126–143, 2019.

[71] K.S. Burch, D. Mandrus, and J. Park. Magnetism in two-dimensional van der Waals materials. *Nature*, 563:47–52, 2018.

[72] S. Jiang, J. Shan, and K.F. Mak. Electric-field switching of two-dimensional van der Waals magnets. *Nat. Mater*, 17:406–410, 2018.

[73] S. Jiang, L. Li, Z. Wang, K.F. Mak, and J. Shan. Controlling magnetism in 2D CrI3 by electrostatic doping. *Nat. Nanotechnol*, 13:549–553, 2018.

[74] Mikhail M Otrokov, Ilya I Klimovskikh, Hendrik Bentmann, D Estyunin, Alexander Zeugner, Ziya S Aliev, S Gaß, AUB Wolter, AV Koroleva, Alexander M Shikin, et al. Prediction and observation of an antiferromagnetic topological insulator. *Nature*, 576(7787):416–422, 2019.

[75] Haiming Deng, Zhiyi Chen, Agnieszka Wołoś, Marcin Konczykowski, Kamil Sobczak, Joanna Sitnicka, Irina V Fedorchenko, Jolanta Borysiuk, Tristan Heider, Łukasz Pluciński, et al. High-temperature quantum anomalous Hall regime in a $MnBi_2Te_4/Bi_2Te_3$ superlattice. *Nature Physics*, 17(1):36–42, 2021.

[76] Bo Chen, Fucong Fei, Dongqin Zhang, Bo Zhang, Wanling Liu, Shuai Zhang, Pengdong Wang, Boyuan Wei, Yong Zhang, Zewen Zuo, et al. Intrinsic magnetic topological insulator phases in the Sb doped MnBi2Te4 bulks and thin flakes. *Nature communications*, 10(1):4469, 2019.

[77] Chang Liu, Yongchao Wang, Hao Li, Yang Wu, Yaoxin Li, Jiaheng Li, Ke He, Yong Xu, Jinsong Zhang, and Yayu Wang. Robust axion insulator and Chern insulator phases in a two-dimensional antiferromagnetic topological insulator. *Nature materials*, 19(5):522–527, 2020.

[78] Seng Huat Lee, David Graf, Lujin Min, Yanglin Zhu, Hemian Yi, Samuel Ciocys, Yuanxi Wang, Eun Sang Choi, Rabindra Basnet, Arash Fereidouni, et al. Evidence for a magnetic-field-induced ideal type-II Weyl state in antiferromagnetic topological insulator $Mn(Bi_{1-x}Sb_x)_2$ Te_4. *Physical Review X*, 11(3):031032, 2021.

[79] J-Q Yan, Qiang Zhang, Thomas Heitmann, Zengle Huang, KY Chen, J-G Cheng, Weida Wu, David Vaknin, Brian C Sales, and Robert John McQueeney. Crystal growth and magnetic structure of MnBi 2 Te 4. *Physical Review Materials*, 3(6):064202, 2019.

[80] SP Weathersby, G Brown, Martin Centurion, TF Chase, Ryan Coffee, Jeff Corbett, JP Eichner, JC Frisch, AR Fry, M Gühr, et al. Mega-electron-volt ultrafast electron diffraction at SLAC National Accelerator Laboratory. *Review of Scientific Instruments*, 86(7), 2015.

[81] G. Kresse and J. Hafner. Ab initio molecular dynamics for liquid metals. *Phys. Rev. B*, 47:558–561, 1993.

[82] G. Kresse and J. Hafner. Ab initio molecular-dynamics simulation of the liquid-metalamorphous- semiconductor transition in germanium. *Phys. Rev. B*, 49:14251–14269, 1994.

[83] G. Kresse and J. Furthmüller. Efficiency of ab-initio total energy calculations for metals and semiconductors using a plane-wave basis set. *Comput. Mater. Sci*, 6:15–50, 1996.

[84] G. Kresse and D. Joubert. From ultrasoft pseudopotentials to the projector augmented-wave method. *Phys. Rev. B*, 59:1758–1775, 1999.

[85] G. Kresse and J. Furthmüller. Efficient iterative schemes for ab initio total-energy calculations using a plane-wave basis set. *Phys. Rev. B*, 54:11169–11186, 1996.

[86] J.P. Perdew, K. Burke, and M. Ernzerhof. Generalized gradient approximation made simple. *Phys. Rev. Lett*, 77:3865–3868, 1996.

[87] S. Grimme, J. Antony, S. Ehrlich, and H. Krieg. A consistent and accurate ab initio parametrization of density functional dispersion correction (DFT-D) for the 94 elements H-Pu. *J. Chem. Phys*, 132:154104, 2010.

[88] S. Grimme, S. Ehrlich, and L. Goerigk. Effect of the damping function in dispersion corrected density functional theory. *J. Comput. Chem*, 32:1456–1465, 2011.

[89] S. Dudarev and G. Botton. Electron-energy-loss spectra and the structural stability of nickel oxide: An LSDA+U study. *Phys. Rev. B Condens. Matter Mater. Phys*, 57:1505–1509, 1998.

[90] A. Togo and I. Tanaka. First principles phonon calculations in materials science. *Scr. Mater*, 108:1–5, 2015.

[91] K. Momma and F. Izumi. VESTA 3 for three-dimensional visualization of crystal, volumetric and morphology data. *J. Appl. Crystallogr*, 44:1272–1276, 2011.

[92] Seng Huat Lee, Yanglin Zhu, Yu Wang, Leixin Miao, Timothy Pillsbury, Hemian Yi, Susan Kempinger, Jin Hu, Colin A Heikes, Patrick Quarterman, et al. Spin scattering and noncollinear spin structure-induced intrinsic anomalous Hall effect in antiferromagnetic topological insulator MnBi2Te4. *Physical Review Research*, 1(1):012011, 2019.

[93] Jeongheon Choe, David Lujan, Martin Rodriguez-Vega, Zhipeng Ye, Aritz Leonardo, Jiamin Quan, T Nathan Nunley, Liang-Juan Chang, Shang-Fan Lee, Jiaqiang Yan, et al. Electron–phonon and spin–lattice coupling in atomically thin layers of MnBi2Te4. *Nano letters*, 21(14):6139–6145, 2021.

[94] Yu-Jie Hao, Pengfei Liu, Yue Feng, Xiao-Ming Ma, Eike F Schwier, Masashi Arita, Shiv Kumar, Chaowei Hu, Rui'e Lu, Meng Zeng, et al. Gapless surface Dirac cone in antiferromagnetic topological insulator MnBi 2 Te 4. *Physical Review X*, 9(4):041038, 2019.

[95] J.F. Ryan and J.F. Scott. Raman study of soft zone-boundary phonons and antiferrodistortive phase transition in BaMnF4. *Solid State Commun*, 14:5–9, 1974.

[96] D.A. Tenne and X. Xi. Raman spectroscopy of ferroelectric thin films and superlattices. *J. Am. Ceram. Soc*, 91:1820–1834, 2008.

[97] D. Chapron, F. Cordero, and M.D. Fontana. Characterization of oxygen vacancies in SrTiO 3 by means of anelastic and Raman spectroscopy. *J. Appl. Phys*, 126:154101, 2019.

[98] N. Sivadas, S. Okamoto, X. Xu, C.J. Fennie, and D. Xiao. Stacking-dependent magnetism in bilayer CrI 3. *Nano Lett*, 18:7658–7664, 2018.

[99] Jing Li, JY Ni, XY Li, H-J Koo, M-H Whangbo, JS Feng, and HJ Xiang. Intralayer ferromagnetism between S= 5 2 ions in MnB i 2 T e 4: Role of empty Bi p states. *Physical Review B*, 101(20):201408, 2020.

[100] T.E. Stevens, J. Kuhl, and R. Merlin. Coherent phonon generation and the two stimulated Raman tensors. *Phys. Rev. B*, 65:144304, 2002.

[101] G.A. Garrett, T.F. Albrecht, J.F. Whitaker, and R. Merlin. Coherent THz phonons driven by light pulses and the Sb problem: what is the mechanism? *Phys. Rev. Lett*, 77:3661–3664, 1996.

[102] HJ Zeiger, J Vidal, TK Cheng, EP Ippen, G Dresselhaus, and MS Dresselhaus. Theory for displacive excitation of coherent phonons. *Physical Review B*, 45(2):768, 1992.

[103] G. Guntherodt, W. Bauhofer, and G. Benedek. Zone-boundary-phonon raman scattering in vi2 due to modulation of exchange interaction. *Phys. Rev. Lett*, 43:1427–1430, 1979.

[104] T. Sekine, M. Jouanne, C. Julien, and M. Balkanski. Light-scattering study of dynamical behavior of antiferromagnetic spins in the layered magnetic semiconductor FePS3. *Phys. Rev. B*, 42:8382–8393, 1990.

[105] Amber McCreary, Thuc T Mai, Franz G Utermohlen, Jeffrey R Simpson, Kevin F Garrity, Xiaozhou Feng, Dmitry Shcherbakov, Yanglin Zhu, Jin Hu, Daniel Weber, et al. Distinct magneto-Raman signatures of spin-flip phase transitions in CrI3. *Nature communications*, 11(1):3879, 2020.

[106] Xingzhi Wang, Kezhao Du, Yu Yang Fredrik Liu, Peng Hu, Jun Zhang, Qing Zhang, Man Hon Samuel Owen, Xin Lu, Chee Kwan Gan, Pinaki Sengupta, et al. Raman spectroscopy of atomically thin two-dimensional magnetic iron phosphorus trisulfide (FePS3) crystals. *2D Materials*, 3(3):031009, 2016.

[107] Michael Först, Cristian Manzoni, Stefan Kaiser, Yasuhide Tomioka, Yoshinori Tokura, Roberto Merlin, and Andrea Cavalleri. Nonlinear phononics as an ultrafast route to lattice control. *Nature Physics*, 7(11):854–856, 2011.

[108] A Stupakiewicz, CS Davies, K Szerenos, D Afanasiev, KS Rabinovich, AV Boris, Andrea Caviglia, AV Kimel, and A Kirilyuk. Ultrafast phononic switching of magnetization. *Nature Physics*, 17(4):489–492, 2021.

[109] Dmytro Afanasiev, JR Hortensius, BA Ivanov, Alireza Sasani, Eric Bousquet, YM Blanter, RV Mikhaylovskiy, AV Kimel, and AD Caviglia. Ultrafast control of magnetic interactions via light-driven phonons. *Nature materials*, 20(5):607–611, 2021.

[110] P Padmanabhan, FL Buessen, R Tutchton, KWC Kwock, S Gilinsky, MC Lee, MA McGuire, SR Singamaneni, DA Yarotski, A Paramekanti, et al. Coherent helicity-dependent spin-phonon oscillations in the ferromagnetic van der Waals crystal CrI3, 2022.

[111] Ankit S Disa, Michael Fechner, Tobia F Nova, Biaolong Liu, Michael Först, Dharmalingam Prabhakaran, Paolo G Radaelli, and Andrea Cavalleri. Polarizing an antiferromagnet by optical engineering of the crystal field. *Nature Physics*, 16(9):937–941, 2020.

[112] Flavio Giorgianni, Björn Wehinger, Stephan Allenspach, Nicola Colonna, Carlo Vicario, Pascal Puphal, Ekaterina Pomjakushina, Bruce Normand, and Ch Rüegg. Ultrafast frustration breaking and magnetophononic driving of singlet excitations in a quantum magnet, 2023.

[113] Carina A Belvin, Edoardo Baldini, Ilkem Ozge Ozel, Dan Mao, Hoi Chun Po, Clifford J Allington, Suhan Son, Beom Hyun Kim, Jonghyeon Kim, Inho Hwang, et al. Exciton-driven antiferromagnetic metal in a correlated van der Waals insulator. *Nature communications*, 12(1):4837, 2021.

[114] Dmytro Afanasiev, Jorrit R Hortensius, Mattias Matthiesen, Samuel Mañas-Valero, Makars Šiškins, Martin Lee, Edouard Lesne, Herre SJ van Der Zant, Peter G Steeneken, Boris A Ivanov, et al. Controlling the anisotropy of a van der Waals antiferromagnet with light. *Science advances*, 7(23):eabf3096, 2021.

[115] AA Melnikov, KN Boldyrev, Yu G Selivanov, VP Martovitskii, SV Chekalin, and EA Ryabov. Coherent phonons in a Bi 2 Se 3 film generated by an intense single-cycle THz pulse. *Physical Review B*, 97(21):214304, 2018.

[116] Martin Rodriguez-Vega, Ze-Xun Lin, Aritz Leonardo, Arthur Ernst, Maia G Vergniory, and Gregory A Fiete. Light-driven topological and magnetic phase transitions in thin layer antiferromagnets, 2022.

[117] M. Köpf, J. Ebad-Allah, S. H. Lee, Z. Q. Mao, and C. A. Kuntscher. Influence of magnetic ordering on the optical response of the antiferromagnetic topological insulator $MnBi_2Te_4$. *Phys. Rev. B*, 102:165139, Oct 2020.

[118] W Baltensperger and JS Helman. Influence of magnetic order in insulators on optical phonon frequency. *Helvetica physica acta*, 41(6-7):668–+, 1968.

[119] Jeongheon Choe, David Lujan, Martin Rodriguez-Vega, Zhipeng Ye, Aritz Leonardo, Jiamin Quan, T Nathan Nunley, Liang-Juan Chang, Shang-Fan Lee, Jiaqiang Yan, et al. Electron–phonon and spin–lattice coupling in atomically thin layers of MnBi2Te4. *Nano letters*, 21(14):6139–6145, 2021.

[120] Bing Li, J-Q Yan, Daniel M Pajerowski, Elijah Gordon, A-M Nedić, Y Sizyuk, Liqin Ke, Peter P Orth, David Vaknin, and Robert J McQueeney. Competing magnetic interactions in the antiferromagnetic topological insulator MnBi 2 Te 4. *Physical review letters*, 124(16):167204, 2020.

[121] Rohit P Prasankumar and Antoinette J Taylor. *Optical techniques for solid-state materials characterization*. CRC press, 2016.

[122] Tatiana Konstantinova, Jonathan D Rameau, Alexander H Reid, Omadillo Abdurazakov, Lijun Wu, Renkai Li, Xiaozhe Shen, Genda Gu, Yuan Huang, Laurenz Rettig, et al. Nonequilibrium electron and lattice dynamics of strongly correlated Bi2Sr2CaCu2O8+ δ single crystals. *Science advances*, 4(4):eaap7427, 2018.

[123] Matthias Knorr, Jürgen Raab, Maximilian Tauer, Philipp Merkl, Dominik Peller, Emanuel Wittmann, Eberhard Riedle, Christoph Lange, and Rupert Huber. Phase-locked multi-terahertz electric fields exceeding 13 MV/cm at a 190 kHz repetition rate. *Optics letters*, 42(21):4367–4370, 2017.

[124] Maximilian Bradler, Peter Baum, and Eberhard Riedle. Femtosecond continuum generation in bulk laser host materials with sub-μJ pump pulses. *Applied Physics B*, 97:561–574, 2009.

[125] Yong-Nian Xu and WY Ching. Electronic structure of yttrium aluminum garnet (Y 3 Al 5 O 12). *Physical Review B*, 59(16):10530, 1999.

[126] Ivan Buchvarov, Anton Trifonov, and Torsten Fiebig. Toward an understanding of white-light generation in cubic media—polarization properties across the entire spectral range. *Optics letters*, 32(11):1539–1541, 2007.

[127] Chihiro Nagura, Akira Suda, Hiroyuki Kawano, Minoru Obara, and Katsumi Midorikawa. Generation and characterization of ultrafast white-light continuum in condensed media. *Applied optics*, 41(18):3735–3742, 2002.